

# Second Harmonic and Sum Frequency Spectroscopy of Thin Films and Molecular Monolayers

A dissertation submitted to the  
SWISS FEDERAL INSTITUTE OF TECHNOLOGY  
LAUSANNE

for the degree of  
Docteur ès Sciences

presented by  
Maximilian Epple  
Dipl. Phys. univ.

examining board:  
Prof Dr K. Kern  
Prof Dr M. Chergui  
Prof Dr B. Devaud-Pledran  
Dr A. Tadjeddine

December 10, 1999



## Version abrégée

Dans ce travail nous avons étudié les transitions électroniques de couches minces de fullerènes par spectroscopie de seconde harmonique (SH) et par des techniques de pompe-sonde et de réseau optique. Un deuxième sujet a été l'étude de dépôt de métal sur des électrodes d'or modifiées avec des monocouches auto-organisées (SAMs, self-assembled monolayers). Dans ces cas, nous avons étudié le comportement des SAMs lors du processus de déposition *in-situ* et ex-situ en sondant les modes vibratoires des SAMs à l'aide de la spectroscopie de somme de fréquences (SF).

La spectroscopie SH du  $C_{60}$  montre quatre transitions dans ou près de la bande interdite. Pour le  $C_{70}$  les signaux sont beaucoup plus faibles, mais pour les deux fullerènes les excitons singulets les plus bas sont observés alors que l'intensité due aux excitons triplets n'est pas observée. La suppression du signal SH sur les résonances du  $C_{60}$  induite par le faisceau pompe n'est efficace que pour la résonance à l'énergie fondamentale photonique la plus basse. Cette suppression a été utilisée pour étudier le temps de vie de l'exciton singulet le plus bas en fonction de la distance métal-substrat (1-3 nm). Même à des distances aussi petites que 1 nm, les mécanismes classiques d'amortissement dominant et aucun indice en faveur de canaux additionnels de désexcitation n'a été détecté. Pour les substrats d'or, nous observons une prédominance du transfert d'énergie au volume alors que pour l'argent le transfert à la surface est dominant.

Nous avons aussi déterminé, par des expériences de réseau, les constantes de diffusion des excitons du  $C_{60}$  pour des énergies pompes au-dessus et en-dessous de la bande interdite. Au-dessus de 1.86 eV énergie d'excitation un coefficient de diffusion étonnamment élevé d'environ  $100 \text{ cm}^2/\text{s}$  est mesuré. Nous suggérons que cela résulte de la diffusion de l'exciton singulet en présence d'excitation vibrationnelle et électronique. En-dessous de l'énergie de 1.86 eV la constante de diffusion diminue abruptement d'environ un ordre de grandeur.

La spectroscopie SF IR-visible de monocouches auto-organisées sur l'or a servi à observer *in-situ* le dépôt électrochimique de métal sur ces électrodes d'or fonctionnalisées en mesurant la plage des vibrations d'élongations C – H.

Le dépôt de cuivre sur des électrodes d'or fonctionnalisées par du hexanethiol  $C_6$  cause une forte augmentation de l'angle d'inclinaison  $\vartheta$  du groupe terminal

méthyl ( $-\text{CH}_3$ ). Nous proposons que le changement d'orientation du thiolate est produit par la pénétration du cuivre dans la couche de thiolate. Le dépôt de cuivre n'a aucune influence sur les spectres d'une couche de thiolate  $\text{C}_{18}$ .

Les SAMs dont le groupe terminal a été modifié par des unités amino ont des forts modes vibratoires méthylène ( $\text{CH}_2$ ) lorsqu'elles sont mesurées dans l'air. Des mesures *in-situ* en solution aqueuse montrent que ces résonances disparaissent. Nous suggérons que cette disparition des résonances est due à la dissolution de la monocouche dans l'électrolyte aqueux, ce qui rompt les liaisons hydrogène.

## Abstract

In this work electronic transitions of thin fullerene films have been studied with second harmonic (SH) spectroscopy and with pump-and-probe and optical grating techniques. A second subject was the investigation of metal deposition on gold electrodes modified with self-assembled monolayers (SAMs). Here we studied the deposition process *in-situ* and ex-situ by probing vibrational modes of the SAMs with sum frequency (SF) spectroscopy.

The SH spectroscopy of  $C_{60}$  shows four transitions in or near the band gap. For  $C_{70}$  the signals are much weaker, but for both fullerenes the lowest singlet excitons are observed while intensity due to the triplet excitons is not found. The pump beam induced suppression of the SH signal on  $C_{60}$  resonances is only efficient for the resonance of the lowest fundamental photon energy. This suppression has been used to study the lifetime of the lowest singlet exciton as a function of distance (1-3 nm) to a metal substrate. Even at distances as small as 1 nm, classic damping mechanisms prevail, and no evidence for additional decay channels is detected. For Au substrates a predominance of energy transfer to the bulk is observed whereas for silver the transfer to the surface is dominant.

We also determined diffusion constants of  $C_{60}$  excitations for optical pump energies above and below the band gap by grating experiments. Above 1.86 eV excitation energy a surprisingly high diffusion constant of about  $100 \text{ cm}^2/\text{s}$  is measured. It is proposed to result from singlet diffusion in the presence of vibrational and electronic excitation. Below 1.86 eV energy the diffusion constant drops abruptly by about one order of magnitude.

IR-visible SF spectroscopy of self-assembled monolayers on gold served to monitor *in situ* the electrochemical deposition of metals on the functionalized gold electrodes by probing the C – H stretching vibration range.

The deposition of copper on hexanethiole  $C_6$  functionalized gold electrodes causes a strong increase of the tilt angle  $\vartheta$  of the terminal methyl ( $-\text{CH}_3$ ) end group. We propose that the orientational change of the thiolate is triggered by the penetration of copper species in the thiolate layer. The copper deposition has no influence on the spectra of a  $C_{18}$  thiolate layer.

Endgroup modified aminothioliolate SAMs show strong methylene ( $-\text{CH}_2$ ) vibrational modes when probed in air. *In-situ* measurements in aqueous solu-

tions show that these resonances vanish. We propose that the disappearance of the resonances is due to solvation of the monolayer in the aqueous electrolyte which breaks up the hydrogen bonds.

# Contents

<b>1</b>	<b>Introduction</b>	<b>1</b>
<b>2</b>	<b>Elements of nonlinear optics</b>	<b>3</b>
2.1	Nonlinear polarization and susceptibility . . . . .	4
2.2	Second order effects . . . . .	5
2.3	Symmetry considerations for $\chi^{(2)}$ . . . . .	8
2.3.1	Permutation symmetries . . . . .	8
2.3.2	Spatial symmetries . . . . .	9
2.4	Refraction law . . . . .	10
2.5	Polarization dependence . . . . .	12
2.6	Fresnel factors . . . . .	13
2.7	Anharmonic oscillator model . . . . .	16
<b>3</b>	<b>Experimental setup</b>	<b>19</b>
3.1	Experimental setup for SHG spectroscopy . . . . .	20
3.1.1	Source of the fundamental radiation and frequency tripling	20
3.1.2	The OPG-OPA for the visible and near infrared range . .	21
3.2	Setup for vibrational SF spectroscopy . . . . .	23
3.2.1	Fundamental beam and third harmonic . . . . .	24
3.2.2	The OPG-OPA for the visible and near infrared range . .	26

3.2.3	The OPA for the mid infrared . . . . .	28
3.3	Normalization strategies . . . . .	32
<b>4</b>	<b>Fullerenes</b>	<b>33</b>
4.1	Generalities . . . . .	33
4.2	Second-harmonic spectroscopy of fullerenes . . . . .	37
4.2.1	Introduction . . . . .	37
4.2.2	Experimental . . . . .	38
4.2.3	C <sub>60</sub> SHG spectroscopy . . . . .	40
4.2.4	C <sub>60</sub> SHG suppression . . . . .	45
4.2.5	C <sub>70</sub> SHG spectroscopy . . . . .	47
4.2.6	Conclusion . . . . .	49
4.3	C <sub>60</sub> exciton quenching near metal surfaces . . . . .	50
4.3.1	Introduction . . . . .	50
4.3.2	Experimental . . . . .	51
4.3.3	Results and discussion . . . . .	52
4.4	Fast transport of excitons in C <sub>60</sub> . . . . .	59
4.4.1	Introduction . . . . .	59
4.4.2	Experimental . . . . .	60
4.4.3	Results . . . . .	61
4.4.4	Discussion . . . . .	65
<b>5</b>	<b>Thiolates - vibrational SF spectroscopy</b>	<b>69</b>
5.1	Properties of alkanethiols on gold . . . . .	71
5.2	Alkanethiolate SAMs on gold in air . . . . .	74
5.2.1	Signatures in vibrational spectroscopy . . . . .	74
5.2.2	Experimental . . . . .	75
5.2.3	Results C <sub>18</sub> thiolate in air . . . . .	79



5.3	Orientation analysis . . . . .	84
5.3.1	Basis of the model . . . . .	84
5.3.2	Construction of the tensor elements . . . . .	85
5.3.3	Intensity . . . . .	89
5.3.4	Results . . . . .	89
5.3.5	Analysis of spectra - Test of the model . . . . .	93
5.4	Instability of C <sub>6</sub> thiolate in air . . . . .	94
5.5	Alkanethiolates and copper deposition . . . . .	97
5.5.1	Introduction . . . . .	97
5.5.2	Experimental . . . . .	103
5.5.3	Stability of the SAMs in the electrolyte and their initial structure . . . . .	107
5.5.4	Change of the spectra through Cu deposition . . . . .	110
5.5.5	Discussion . . . . .	113
5.5.6	Conclusion . . . . .	117
5.6	Spectroscopic study of aminothiolate . . . . .	119
5.6.1	Introduction . . . . .	119
5.6.2	Experimental . . . . .	120
5.6.3	Spectral characterization of the AT SAM in air . . . . .	121
5.6.4	Influence of the electrolyte – comparison between <i>ex-situ</i> and <i>in-situ</i> . . . . .	122
5.6.5	Discussion . . . . .	126
<b>6</b>	<b>Conclusion</b>	<b>129</b>
<b>A</b>	<b>Fresnel factors</b>	<b>131</b>
	<b>Curriculum Vitae</b>	<b>145</b>
	<b>Remerciements</b>	<b>147</b>

Parts of this thesis are based on the following articles:

- Chapter 4.2    K. Kuhnke, M. Epple, and K. Kern  
Chem. Phys. Lett. **294**, 241 (1998).
- Chapter 4.3    K. Kuhnke, R. Becker, M. Epple, and K. Kern  
Phys. Rev. Lett. **79**, 3246 (1997).

# Chapter 1

## Introduction

Surfaces and interfaces play a prominent role in many key technologies such as catalysis, microelectronics, magnetic storage and biosensorics. Detailed knowledge of surface processes and the specific manipulation of surface properties are therefore of great current interest.

One possibility to modify the properties of a surface is to coat it with organic thin films. This can be done in a very versatile way with self-assembled monolayers (SAMs). SAMs consist of molecules which are chemically bound to the surface. Well ordered monolayers form as a result of the interaction between the adsorbed molecules. By choosing the functional group of the molecules which will be situated at the air/film interface the properties of this interface can be modified in a controlled way. Here we demonstrate how SAMs can be employed for the fabrication of nanostructures.

We have used alkane thiolate SAMs as spacer layers between thin films of  $C_{60}$  molecules and metal surfaces. The thickness of the spacer layer and thus the distance of the thin  $C_{60}$  film to the metal substrate has been fine tuned by varying the chain length of the alkane thiolate in order to change the coupling to the substrate. Using this method the spacer layer thickness can be varied from 1 to 3 nm with a stepwidth of 0.2 nm. We have also used the SAMs in order to control the electrochemical deposition of metals. For instance, when copper is deposited on bare gold surfaces, it grows rapidly in three dimensional islands. Covering the gold surface with an alkane thiolate SAMs allows to grow the copper layer-by-layer at the interface between gold and the SAM. For this

system it is of interest to investigate not only the morphology of the adsorbate but to study the active role which the SAM plays in the deposition process. In the case of deposition of palladium on gold, functionalizing the SAM with an amino group leads to the deposition of palladium clusters and islands *on top* of the SAM, where they are decoupled from the gold substrate.

Numerous techniques have been developed for the investigation of surfaces in the last decades. The structure can be studied by, e.g., He diffraction or low-energy electron diffraction, the electronic properties are accessible with x-ray and ultraviolet photoelectron spectroscopy, and the vibrational modes for example with electron energy loss spectroscopy. A major drawback of these techniques is that they can only be applied under ultra high vacuum conditions. Even though this provides the possibility to prepare and study clean, well characterized systems, a fundamental interest remains for systems in their “natural” environment like aqueous solutions or ambient pressure. Furthermore well characterized surfaces and films can also be prepared in an electrochemical environment. With the development of tunable laser systems in the mid-eighties, nonlinear spectroscopical methods like second harmonic (SH) and sum frequency (SF) spectroscopy became possible in a wide wavelength range, thereby allowing the investigation of the electronic and vibrational excitations. SH and SF can be used in natural or electrochemical environment and anywhere where light has access. Furthermore, due to their physical nature, SH and SF are, in contrast to linear optics, inherently surface- and interface- sensitive. The method is also sensitive to excitons and as a three photon process sensitive to forbidden transitions. This will be employed to study spectroscopically transitions in fullerenes below and above the band-gap and their dynamics.

We investigated by SH and SF spectroscopy the systems described above. Following the description of the basic concepts of nonlinear optics (Chapter 2) the experimental setup is presented (Chapter 3). Then we focus on the electronic properties of fullerene films (Chapter 4). Here the special selection rules of SH generation are helpful for the investigation of the electronic excitation which are very difficult to observe with linear optics. In this chapter also the dynamics of excitons in  $C_{60}$  are addressed in time-resolved studies. Finally we present the results for the metal deposition on SAM-functionalized gold surfaces (Chapter 5) obtained by monitoring the deposition process *in-situ* with vibrational SF spectroscopy of the SAM molecules.

## Chapter 2

# Elements of nonlinear optics

In the vacuum, light waves obey the superposition principle, which means that two electromagnetic waves can simply be described as the sum of the two waves. They do not influence each other mutually. The reason is, that the Maxwell equations, which describe electromagnetism are a set of *linear* differential equations in the case of the vacuum. In matter however, the electric fields of the light waves exert forces on the charged particles, thus inducing a response from the medium. The influence of the magnetic field is much smaller and can be neglected in most cases. If the electric field is weak enough so that the response is proportional to the electric field, the Maxwell equations remain linear (in the electric field). In this case the light waves, if they are able to penetrate and pass through a medium, are well described by linear optics. But if the electric field of the light waves becomes comparable to interatomic fields which act on the electrons ( $\sim 1\text{V}/\text{\AA} = 10^{10}\text{V/m}$ ), the induced response is no more linear in the electric field and the light waves are interacting. The necessary light intensities can be obtained with lasers.

The aim of this chapter is to introduce the nonlinear optical effects which are important for the understanding of this work and to summarize the essential properties, which are used in the further chapters. Thus we introduce the  $\chi^{(2)}$  tensor which is probed by second harmonic and sum frequency generation. Then, symmetry considerations lead the explanation why second order nonlinear optics is inherently surface and interface sensitive. Moreover it will be explained which experimental geometries have to be adapted and finally why electronic and vibrational resonances can be investigated by probing  $\chi^{(2)}$ .

In most cases the properties are illustrated for the sum frequency generation. The formula for the second harmonic generation can easily be deduced from this more general case.

## 2.1 Nonlinear polarization and susceptibility

All electromagnetic phenomena are governed by Maxwell's equations.

$$\begin{aligned}
 \vec{\nabla} \times \vec{H} &= \vec{j}(\vec{r}, t) + \frac{\partial \vec{D}}{\partial t} \\
 \vec{\nabla} \times \vec{E} &= -\frac{\partial \vec{B}}{\partial t} \\
 \vec{\nabla} \cdot \vec{D} &= \rho \\
 \vec{\nabla} \cdot \vec{B} &= 0
 \end{aligned} \tag{2.1}$$

The response of a medium to the electromagnetic field is described by the constitutive relations.

$$\begin{aligned}
 \vec{D} &= \varepsilon_o \vec{E} + \vec{P} - \vec{\nabla} \cdot \vec{Q} + \dots \\
 \vec{H} &= \frac{1}{\mu_o} \vec{B} - \vec{M} + \dots
 \end{aligned} \tag{2.2}$$

where  $\vec{P}$ ,  $\vec{M}$  and  $\vec{Q}$  are the electric dipole, the magnetic dipole and the electric quadrupole moments per unit volume [1].  $(\vec{\nabla} \cdot \vec{Q})$  signifies that the  $i$ -th component of the vector  $(\vec{\nabla} \cdot \vec{Q})_i$  is  $\nabla_k Q_{ik}$ . Here and in the following the Einstein sum convention (summing over double indices) is adopted.

In the *dipole approximation* only the electric dipole term of the response of the medium is considered whereas the magnetic dipole, the electric quadrupole as well as higher multipole orders are neglected. In the following considerations dipole approximation is always assumed, unless specified otherwise.

For a transparent dielectric medium without free charges or current and with vanishing conductivity, the following wave equation can directly be de-

rived from the Maxwell equations (2.1) and the constitutive relations (2.2).

$$\left[ \vec{\nabla} \times (\vec{\nabla} \times) + \frac{1}{c_o^2} \frac{\partial^2}{\partial t^2} \right] \vec{E}(\vec{r}, t) = -\frac{1}{c_o^2 \epsilon_o} \frac{\partial^2}{\partial t^2} \vec{P}(\vec{r}, t) \quad (2.3)$$

The left hand side of equation 2.3 corresponds to the propagation of an electric wave in the vacuum and it is the source term which is induced through the electric field of the right hand side which also radiates a wave and gives rise to linear and nonlinear effects.

In order to see some of the nonlinear effects, we will pass via Fourier transformation into the frequency space:

$$(\vec{r}, t) \longrightarrow (\vec{k}, \omega)$$

Here the induced polarization  $\vec{P}$  can be expanded into a power series of the electrical field  $\vec{E}$ . For the  $i$ -th component of the polarization we have:

$$\begin{aligned} P_i &= \epsilon_o \left\{ \chi_{ij}^{(1)} E_j + \chi_{ijk}^{(2)} E_j E_k + \chi_{ijkl}^{(3)} E_j E_k E_l + \dots \right\} \\ &= P_i^{(1)} + P_i^{(2)} + P_i^{(3)} + \dots \end{aligned} \quad (2.4)$$

$\chi^{(1)}$  is called linear susceptibility,  $\chi^{(2)}$  second order susceptibility or the first order nonlinear susceptibility and so on. In the electric dipole approximation the susceptibilities are independent of  $\vec{k}$  [2]. The term  $P_i^{(1)}$  describes the linear correlation between the polarization and the field. The nonlinear terms become important when dealing with high electric fields. It is obvious that in the higher orders the electromagnetic waves interact with each other via the nonlinear susceptibilities.

## 2.2 Second order effects

In the following only the second order polarization  $P^{(2)}$  will be considered. When the incident electric field is a monochromatic beam with the frequency  $\omega$ , we can write:

$$E_j = \frac{1}{2} E_j(\omega) e^{i\omega t} + c.c. \quad (2.5)$$

The application of equation 2.5 to equation 2.4 gives two terms for  $P^{(2)}$ . One is a static polarization which is known as optical rectification. The other term oscillates with the frequency  $2\omega$  and gives rise to the radiation of the second harmonic frequency. It has the form:

$$P_i^{(2)}(2\omega) = \varepsilon_o \chi_{ijk}^{(2)} E_j(\omega) E_k(\omega) \quad (2.6)$$

When the incident field is the superposition of two fields with the frequencies  $\omega_1$  and  $\omega_2$  (with  $\omega_1 > \omega_2$ ) we have:

$$E_j = \frac{1}{2}(E_j(\omega_1)e^{(i\omega_1 t)} + E_j(\omega_2)e^{(i\omega_2 t)}) + c.c. \quad (2.7)$$

The polarization  $P_i^{(2)}$  is now a sum, which beside the optical rectification also contains terms that are oscillating with the frequencies  $2\omega_1$ ,  $2\omega_2$ ,  $\omega_1 + \omega_2$  and  $\omega_1 - \omega_2$  which correspond to the generation of the second harmonic frequency of  $\omega_1$  and  $\omega_2$  and to the generation of the sum frequency and the difference frequency, respectively.

The contribution which describes for example the sum frequency can be written as:

$$P_i^{(2)}(\omega_3 = \omega_1 + \omega_2) = \varepsilon_o \chi_{ijk}^{(2)} E_j(\omega_1) E_k(\omega_2) \quad (2.8)$$

In order to write this equation, the intrinsic permutation property of  $\chi^{(2)}$  (see section 2.3.1) had to be used.

In the photon picture all these processes can be understood as the interaction between three photons which is also referred to as three wave mixing. Two incident photons are converted to the third one. Figure 2.1 shows this in a schematic diagram for the second harmonic, the sum frequency and the difference frequency generation.

The process in part c) of figure 2.1 where a photon of the frequency  $\omega_3$  is converted into two photons with the frequencies  $\omega_1$  and  $\omega_2$  ( $\omega_3 > \omega_1 > \omega_2$ ) is also called optical parametrical generation (OPG) or optical parametrical amplification (OPA). The difference between OPG, OPA and DFG are the input conditions. Normally optical parametric processes are considered as initiated by a single pump beam. For OPG the initial numbers of photons of the frequency  $\omega_1$  or  $\omega_2$  is zero and parametric scattering of the pump beam



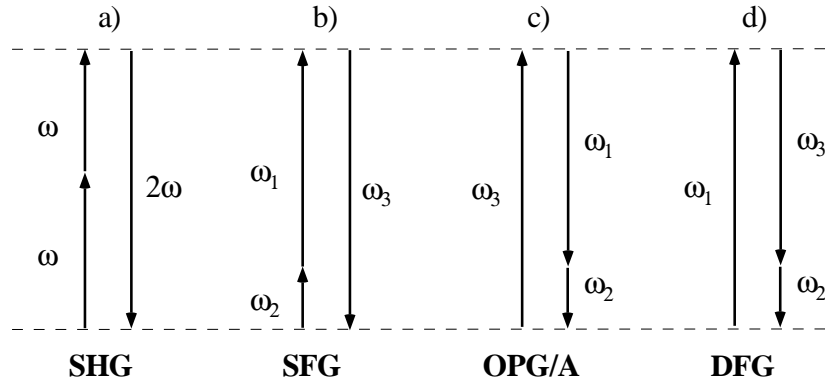


Figure 2.1: Schematic diagram of three wave mixing processes in the photon picture (see text). Energy conservation requires that  $\omega_1 + \omega_2 = \omega_3$  or  $\omega_1 - \omega_2 = \omega_3$  for SFG/OPG/OPA or DFG, respectively.

$\omega_3$  provides single photons of the frequencies  $\omega_1$  and  $\omega_2$  ( $\omega_3 = \omega_1 + \omega_2$ ). The amplification of these noise photons in a nonlinear crystal is known as OPA or as parametric superfluorescence (also see chapter 3). Of the two generated photons, the one with the higher frequency is called *signal* and the other one *idler*. In contrast DFG is considered as initiated by two pump beams of more or less comparable intensity. The difference between OPA and DFG disappears after a significant fraction of the pump energy has been transferred to the lower frequency fields [2].

If the incident field is the superposition of more than two monochromatic waves,  $P_i^{(2)}$  contains still only three-photon processes, like the generation of all second harmonic frequencies or all possible combinations of the sum or difference of two photons. In order to obtain higher order processes as for example the sum of three photons, polarizations of higher order than  $P_i^{(2)}$  are needed. Therefore, when dealing with  $P_i^{(2)}$ , without loss of generality only incident waves with maximal two different frequencies are considered.

## 2.3 Symmetry considerations for the second order susceptibility $\chi^{(2)}$

The second order susceptibility  $\chi^{(2)}$  for each second order process is a third rank tensor and has thus at most 27 independent elements. Indeed these 27 elements are not all independent. The physical nature of  $\chi^{(2)}$ , however, gives rise to permutation symmetries. These and the spatial symmetry of the medium can significantly reduce the number of independent tensor elements.

### 2.3.1 Permutation symmetries

The most important permutation symmetry is called the *intrinsic permutation* symmetry. In order to illustrate it we will first look at the case of sum frequency generation in a field which has the monochromatic frequency contributions  $\omega_1$  and  $\omega_2$ . The second order susceptibility usually is written as  $\chi_{ijk}^{(2)}(\omega_3; \omega_1, \omega_2)$  where  $\omega_3 = \omega_1 + \omega_2$ . Intrinsic permutation symmetry means that  $\chi^{(2)}$  remains invariant under the permutation of the pairs  $(j, \omega_1)$  and  $(k, \omega_2)$ . The physical meaning of this is that it does not matter which one of the frequency components we label  $\omega_1$  and which  $\omega_2$ . In the case of SHG  $\omega_1$  is equal to  $\omega_2$ . This is why the second order susceptibility is invariant to the permutation of the indices  $j$  and  $k$  which reduces the independent tensor elements for SHG from 27 to 18.

Other important permutation symmetries are the *overall permutation* symmetry and the *Kleinmann* symmetry.

The prerequisite for the *overall permutation* symmetry is that absorbance at all involved frequencies can be neglected. From the microscopic expressions of  $\chi^{(2)}$  [2, 3] it can be seen that  $\chi^{(2)}$  stays invariant under the permutation of the pairs  $(j, \omega_1)$ ,  $(k, \omega_2)$  and  $(i, \omega_3)$ . From this the famous Manley-Rowe equations can be derived which describe the energy flux between the involved monochromatic fields [3]. For example in the case of the optical parametrical amplification they show, that the power loss of the pump field is equal to the gain of power of the two fields of lower energy. This is already suggested by the description in the photon picture (figure 2.1).

The prerequisite for the *Kleinmann* symmetry is that the absorption *and*

the dispersion of the medium for all involved optical frequencies is negligible. This is true when all involved frequencies are far from resonances of the medium. In this case all the cartesian indices  $i, j, k$  of  $\chi_{ijk}^{(2)}$  can be freely permuted and therefore the 27 elements are reduced to 10 independent elements.

### 2.3.2 Spatial symmetries

Let us now consider media with spatial symmetry. Spatial symmetry operations are coordinate transformations which leave the system unchanged. When the system is unchanged, the physical properties stay the same. In other words the physical properties have to be invariant under the symmetry transformations. This is also known as the Neumann principle. A third rank tensor transforms as follows:

$$\chi_{ijk}^{(2)'} = T_{il}T_{jm}T_{kn}\chi_{lmn}^{(2)} \quad (2.9)$$

where  $T_{ij}$  is the matrix representing the symmetry transformation. The Neumann principle states that all the tensor elements  $\chi_{ijk}^{(2)'}$  and  $\chi_{ijk}^{(2)}$  must be equal.

#### Centrosymmetric medium

For a *centrosymmetric* medium the symmetry transformation is the inversion.  $T_{ij} = -\delta_{ij}$  where  $\delta_{ij}$  is the Kronecker symbol ( $\delta_{ij} = 1$  for  $i = j$  and  $\delta_{ij} = 0$  for  $i \neq j$ ). Applying Neumann's principle to the inversion, it immediately follows with equation 2.9 that  $\chi_{ijk}^{(2)'} = -\chi_{ijk}^{(2)}$  for all  $i, j, k$ , which can only be true if  $\chi_{ijk}^{(2)} \equiv 0$  for all  $i, j, k$ . This means that the second order susceptibility  $\chi^{(2)}$  vanishes identically in centrosymmetric media and thus second order processes are not allowed as can directly be seen from equation 2.4. However, at the interface between two centrosymmetric media the inversion symmetry is broken and second order processes become allowed. This is the reason for the inherent surface and interface sensitivity of second order nonlinear optics.

#### Isotropic interface

In the case of an isotropic interface we find the following symmetry operations. A rotation by any angle  $\varphi$  about the surface normal ( $z$ -axis) leaves the system

unchanged as well as the reflection at the  $xz$ - and the  $yz$ - planes ( $x$ - and  $y$ -axis lie in the surface plane). A homogeneously distributed chiral adsorbate for example is compatible with the rotational symmetry operation but it breaks the reflection symmetries.

Applying Neumann's principle together with the reflections shows that all tensor elements of  $\chi^{(2)}$  vanish with exception of:

$$\chi_{xxz}^{(2)}, \chi_{xzx}^{(2)}, \chi_{yyz}^{(2)}, \chi_{yzy}^{(2)}, \chi_{zxx}^{(2)}, \chi_{zyy}^{(2)}, \chi_{zzz}^{(2)} \quad (2.10)$$

The application of the rotations furthermore results in:

$$\begin{aligned} \chi_{xxz}^{(2)} &= \chi_{yyz}^{(2)} \\ \chi_{xzx}^{(2)} &= \chi_{yzy}^{(2)} \\ \chi_{zxx}^{(2)} &= \chi_{zyy}^{(2)} \end{aligned} \quad (2.11)$$

This is why finally only four independent elements of  $\chi^{(2)}$  remain:

$$\chi_{xxz}^{(2)}, \chi_{xzx}^{(2)}, \chi_{zxx}^{(2)}, \chi_{zzz}^{(2)} \quad (2.12)$$

## 2.4 Refraction law

We will now consider two beams with frequency  $\omega_1$  and  $\omega_2$  which are incident in the same plane on an interface where SFG or DFG are generated. We are interested in the reflected beams and we can choose the coordinate system such that the incident beams have no  $y$ -component (see figure 2.2).

Energy conservation requires that the generated frequency  $\omega_3$  is  $\omega_1 + \omega_2$  for SFG and  $\omega_3 = \omega_1 - \omega_2$  for DFG ( $\omega_1 > \omega_2$ ). The boundary conditions imply that the parallel components of the electric and magnetic field are continuous across the interface. This is why the parallel components of the involved  $\vec{k}$  vectors are conserved.

$$k_{1,x}^i = k_{1,x}^r \quad (2.13)$$

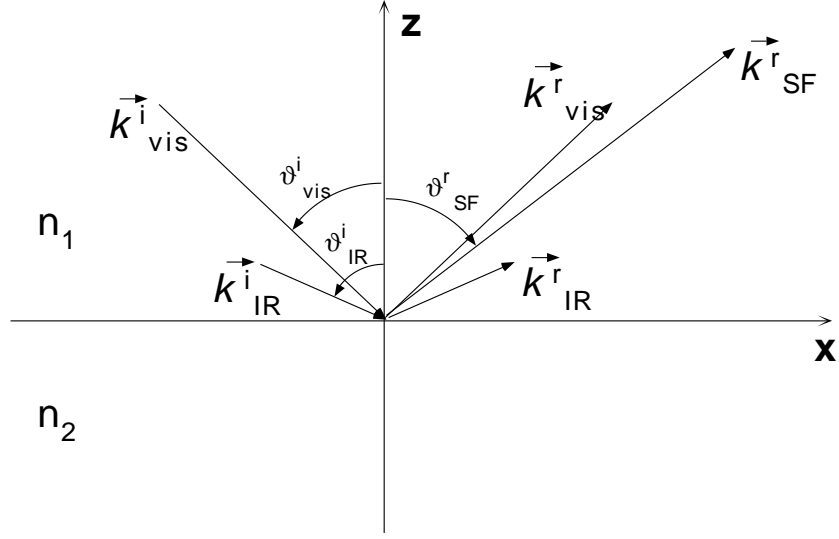


Figure 2.2: Sketch of sum frequency generation in reflection from an interface.  $\vec{k}^i$  and  $\vec{k}^r$  are the wave vectors for the incident and the reflected light, respectively. IR, vis, and SF is for infrared, visible and sum frequency, respectively. The transmitted beams are omitted for the sake of simplicity.  $n_1$  and  $n_2$  are the refraction indices of the two centrosymmetric media which are separated by the  $x - y$ -plane. The non-linear polarization is generated at the interface.

$$k_{2,x}^i = k_{2,x}^r \quad (2.14)$$

$$\text{for SFG} \quad k_{3,x}^r = k_{1,x}^r + k_{2,x}^r \quad (2.15)$$

$$\text{and for DFG} \quad k_{3,x}^r = k_{1,x}^r - k_{2,x}^r \quad (2.16)$$

Expressing the projections on the interface results in:

$$k_3^r \sin \vartheta_3 = k_1^i \sin \vartheta_1 \pm k_2^i \sin \vartheta_2 \quad (2.17)$$

$$\text{with} \quad k_\alpha^{i,r} = |\vec{k}_\alpha^{i,r}| = \frac{\omega_\alpha}{c_0} n(\omega_\alpha) \quad (\alpha = 1, 2, 3) \quad (2.18)$$

Where the plus sign is for SFG and the minus sign for DFG. When dispersion can be neglected we have:

$$\sin \vartheta_3^r = \frac{1}{\omega_3} (\omega_1 \sin \vartheta_1^i \pm \omega_2 \sin \vartheta_2^i) \quad (2.19)$$

The reflected SFG beam lies in between the reflected fundamental beams. In the case of SHG ( $\omega_1 = \omega_2$  and  $\vartheta_1^i = \vartheta_2^i$ ) the reflected SHG beam is collinear with the reflected fundamental beam. For DFG the right hand side of equation 2.19 can be greater than 1. In this case the generation of the difference frequency is forbidden. The physical reason is that the required  $k_{3,x}^r$  (eq. 2.16) leads to a lower limit for the absolute value of the  $\vec{k}_3$ -vector which is too large to fulfill the dispersion relation (eq. 2.18) for  $\omega_3 = \omega_1 - \omega_2$ . A graph describing the allowed angles of incidence in dependence of the wavelength can be found in [4].

## 2.5 Polarization dependence

We will now look at waves incident in the  $xz$ -plane for the case of SFG (see figure 2.2) and we will label here  $\omega_1$ ,  $\omega_2$  and  $\omega_3$  as  $\omega_{vis}$ ,  $\omega_{IR}$  and  $\omega_{SF}$  respectively. Waves which are  $s$ -polarized (perpendicular to the plane of incidence) have an  $\vec{E}$ -field component only in the  $y$ -direction, whereas waves which are  $p$ -polarized (parallel to the plane of incidence) have only components in the  $x$ - and in the  $z$ -direction. The polarization combinations are designated by three letters of which the first, second and third letters refer to the polarizations of the SF, of the visible and of the infrared beam respectively. Using only the nonvanishing tensor components from equation 2.10, equation 2.8 yields together with equation 2.11 the second order polarization components for the different polarization combinations:

$$\text{ssp:} \quad P_y^{(2)}(\omega_{SF}) = \chi_{xxz}^{(2)} E_y(\omega_{vis}) E_z(\omega_{IR}) \quad (2.20)$$

$$\text{sps:} \quad P_y^{(2)}(\omega_{SF}) = \chi_{xzx}^{(2)} E_z(\omega_{vis}) E_y(\omega_{IR}) \quad (2.21)$$

$$\text{pss:} \quad P_z^{(2)}(\omega_{SF}) = \chi_{zxx}^{(2)} E_y(\omega_{vis}) E_y(\omega_{IR}) \quad (2.22)$$

and for ppp:

$$\begin{aligned}
P_x^{(2)}(\omega_{SF}) &= \chi_{xxx}^{(2)} E_x(\omega_{vis})E_z(\omega_{IR}) + \chi_{xzx}^{(2)} E_z(\omega_{vis})E_x(\omega_{IR}) \\
P_z^{(2)}(\omega_{SF}) &= \chi_{zzz}^{(2)} E_z(\omega_{vis})E_z(\omega_{IR}) + \chi_{zxx}^{(2)} E_x(\omega_{vis})E_x(\omega_{IR})
\end{aligned} \tag{2.23}$$

The combinations *sss*, *spp*, *psp* and *pps* give no contribution. We can immediately conclude that if the fundamental beams are both *s*-polarized or both *p*-polarized, the SF output is only *p*-polarized. If one of the fundamental beams is *s*- and the other one is *p*-polarized, the SF output is only *s*-polarized. We can also conclude that for SHG, where, due to the intrinsic permutation symmetry,  $\chi_{xxz}^{(2)} = \chi_{xzx}^{(2)}$ , a preferable polarization combination is the one where the fundamental beam is linearly polarized with both *s* and *p* components (i.e. is rotated away from the plane of incidence by  $\pm 45^\circ$ ) and the SH output is *s* polarized (here a polarizer is needed for the SH beam in order to suppress the generated *p*-output).

When using *ssp*-, *sps*- or *pss*-polarization, only one tensor element is probed at a time, whereas in *ppp*-polarization a combination of all independent elements enters in the output, which complicates the interpretation of the detected signal.

One has to keep in mind that the fields in the equations 2.20 - 2.23 are the effective fields at the interface. The relation between these effective fields and the incident fields is treated in the next section.

## 2.6 Fresnel factors

We are now going to discuss how the incoming and the outgoing fields are related to the physical quantities at the interface for the case of SFG. The results will depend on the model which is used to describe the studied system. We will be considering a simple model where the nonlinear polarization is created in a thin polarization sheet with thickness  $d$ . This sheet separates two linear media which are called medium 1 and medium 2 having the refraction indices  $n_1$  and  $n_2$ , respectively (like in Fig.2.2). Since the wavelength of the involved beams is at least two orders of magnitude larger than the thickness of the sheet, the transition  $d \rightarrow 0$  can be performed. The polarization sheet is situated at  $z = 0^+$  and has the same refraction index as medium 1. The

fundamental beams are incident from medium 1 to the interface and the SF beam is emitted into medium 1 (see also Fig.2.2).

We are defining, following the notation by Hirose [5], a Fresnel coefficient  $L$  which relates the polarization generated in the sheet to the radiated SF field in medium 1. With  $E_p^{SF,out}$  and  $E_s^{SF,out}$  being the amplitude of the  $p$ - and  $s$ -polarized field respectively we have:

$$\begin{aligned} E_p^{SF,out} &= L_x P_x + L_z P_z \\ E_s^{SF,out} &= L_y P_y \end{aligned} \quad (2.24)$$

The Fresnel coefficients which relate the incident fundamental fields to the effective fields in the polarization sheet are called  $K$  and are defined as,

$$\begin{aligned} E_x &= K_x E_p^{in} \\ E_y &= K_y E_s^{in} \\ E_z &= K_z E_p^{in} \end{aligned} \quad (2.25)$$

where  $E_p^{in}$  and  $E_s^{in}$  signify the amplitudes of the incident  $p$ - and  $s$ -polarized fundamental field respectively.

A derivation for the  $L$ -coefficients can be found in [5]. The  $K$ -coefficients in the polarization sheet can be determined from the usual Fresnel coefficients (see for example [6]). In the described model the  $L$ - and  $K$ -coefficients for the polarization sheet are:

$$\begin{aligned} L_x &= -Q \frac{\cos \vartheta_2}{2n_1 \cos \vartheta_1} t_{12}^p; & K_x &= \cos \vartheta_2 t_{12}^p \\ L_y &= Q \frac{1}{2n_1 \cos \vartheta_1} t_{12}^s; & K_y &= t_{12}^s \\ L_z &= Q \left(\frac{n_2}{n_1}\right)^2 \frac{\sin \vartheta_2}{2n_1 \cos \vartheta_1} t_{12}^p; & K_z &= \left(\frac{n_2}{n_1}\right)^2 \sin \vartheta_2 t_{12}^p \end{aligned} \quad (2.26)$$

with

$$Q = \frac{4\pi i \omega_{SF}}{c}; \quad t_{12}^p = \frac{2n_1 \cos \vartheta_1}{n_2 \cos \vartheta_1 + n_1 \cos \vartheta_2}; \quad t_{12}^s = \frac{2n_1 \cos \vartheta_1}{n_1 \cos \vartheta_1 + n_2 \cos \vartheta_2} \quad (2.27)$$

The angles  $\vartheta_2$  have to be inferred from Snell's law ( $n_1 \sin \vartheta_1 = n_2 \sin \vartheta_2$ ). One has to keep in mind that for the  $L$  coefficients the refraction indices at



$\omega_{SF}$  have to be taken and for the  $K$  coefficients the refraction indices at  $\omega_{vis}$  and  $\omega_{IR}$ . As a reminder they are called  $K^{vis}$  and  $K^{IR}$ , respectively. In order to simplify the notation the product  $L_i K_j^{vis} K_k^{IR}$  is abbreviated as  $F_{ijk}$  and called nonlinear Fresnel factor. The indices of  $F_{ijk}$  correspond to the indices of the involved fields and not to the indices of  $\chi^{(2)}$ . Using the equations 2.20-2.23, 2.24, 2.25 and the definition of the nonlinear Fresnel factors, the SF field radiated from an isotrope interface can now conveniently be written as follows:

$$\text{ssp:} \quad E_s^{out}(\omega_{SF}) = \chi_{xxz}^{(2)} F_{yyz} E_s^{in}(\omega_{vis}) E_p^{in}(\omega_{IR}) \quad (2.28)$$

$$\text{sps:} \quad E_s^{out}(\omega_{SF}) = \chi_{xzx}^{(2)} F_{yzy} E_p^{in}(\omega_{vis}) E_s^{in}(\omega_{IR}) \quad (2.29)$$

$$\text{pss:} \quad E_p^{out}(\omega_{SF}) = \chi_{zxx}^{(2)} F_{zyy} E_s^{in}(\omega_{vis}) E_s^{in}(\omega_{IR}) \quad (2.30)$$

and for ppp:

$$\begin{aligned} E_p^{out}(\omega_{SF}) &= E_p^{in}(\omega_{vis}) E_p^{in}(\omega_{IR}) \\ &\times \left\{ \chi_{xxz}^{(2)} F_{xxz} + \chi_{xzx}^{(2)} F_{xzx} + \chi_{zzz}^{(2)} F_{zzz} + \chi_{zxx}^{(2)} F_{zxx} \right\} \end{aligned} \quad (2.31)$$

This is also true for the case of SHG, however the Fresnel coefficients can have other expressions than in equations 2.26 since they depend on the experimental situation. Other geometries for example are discussed in [7]. The angle dependence of the seven nonlinear Fresnel coefficients which appear in equations 2.28-2.31 are plotted in figure 2.3.

We take for medium 1 water and for medium 2 gold. The wavelength for the SF field is 450 nm, for the visible field 532 nm and for the IR field 2900 nm. The corresponding refraction indices can be found in the appendix A. The incident angle of the visible beam is  $4^\circ$  larger than the incident angle of the infrared beam. As can be seen from figure 2.3 the factors  $F_{xxz}$ ,  $F_{yyz}$  and  $F_{zzz}$  are important compared to  $F_{xzx}$ ,  $F_{yzy}$ ,  $F_{zxx}$  and  $F_{zyy}$ . It follows immediately (with equations 2.28-2.31) that the only possible polarization combinations are *ssp* or *ppp* whereby the *ppp*-polarization yields more intensity. The physical reason for this is that due to the dielectric function of gold the parallel component of the IR beam at the interface is strongly reduced. In addition the angular dependence of the  $F_{ijk}$  factors suggests a beam geometry where the angle of incidence of the fundamental beams is around  $70^\circ$ .

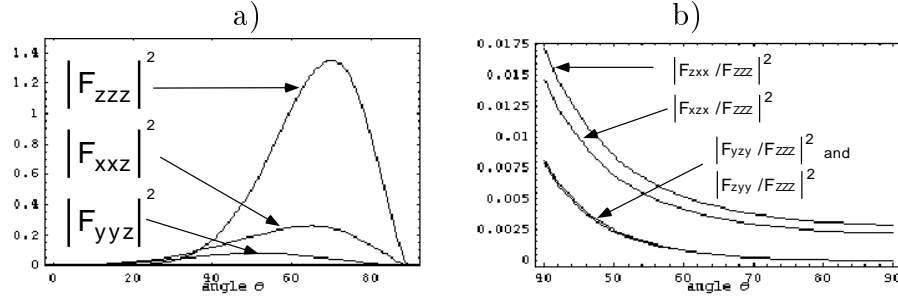


Figure 2.3: a) The dominant nonlinear Fresnel coefficients on gold. The angle of incidence of the IR beam is  $\vartheta_{IR} = \vartheta_{vis} - 4^\circ$  b) The nondominant Fresnel coefficients normalized to  $F_{zzz}$ . See also text.

## 2.7 Anharmonic oscillator model

In the previous section the expression for the radiated field has been given. The frequency dependence of this expression is often dominated by the frequency dependence of  $\chi^{(2)}$ , that we will study in more detail now in a simple model.

In this model a medium is composed of a set of  $N$  classical anharmonic oscillators per unit volume. Its equation of motion in the presence of a driving force  $F$  is:

$$\frac{d^2 x}{dt^2} + \Gamma \frac{dx}{dt} + \Omega^2 x + ax^2 = F \quad (2.32)$$

where the symbols have the usual signification. The driving force is caused by an electric field with two frequency components  $\omega_1$  and  $\omega_2$ .

$$F = \frac{q}{m} \left\{ E_1 (e^{i\omega_1 t} + e^{-i\omega_1 t}) + E_2 (e^{i\omega_2 t} + e^{-i\omega_2 t}) \right\} \quad (2.33)$$

When the anharmonic term  $ax^2$  is small it can be treated in perturbation theory. The displacement  $x$  can then be written as [2]

$$x = x^{(1)} + x^{(2)} + x^{(3)} + \dots + c.c. \quad (2.34)$$

The induced electric polarization is:

$$P = Nqx = Nqx^{(1)} + Nqx^{(2)} + Nqx^{(3)} + \dots + c.c. = P^{(1)} + P^{(2)} + P^{(3)} + \dots + c.c. \quad (2.35)$$

With the relation  $P^{(2)} = \chi^{(2)} E_1 E_2$  we find in the second order [2] for the term corresponding to the sum or difference frequency

$$\chi^{(2)}(\omega_1 \pm \omega_2) = \frac{-2aNg^3}{m^2} \frac{1}{(\Omega^2 - \omega_1^2 - i\omega_1\Gamma)(\Omega^2 - \omega_2^2 \mp i\omega_2\Gamma)} \times \frac{1}{\Omega^2 - (\omega_1 \pm \omega_2)^2 - i(\omega_1 \pm \omega_2)\Gamma} \quad (2.36)$$

From equation 2.36 it can be seen that  $\chi^{(2)}$  is resonantly enhanced when one of the fundamental frequencies  $\omega_1$ ,  $\omega_2$  or the sum respectively difference frequency coincides with the eigen frequency  $\Omega$  of the system. The same is valid for SHG where  $\chi^{(2)}$  is resonantly enhanced when the fundamental or the second harmonic frequency coincides with  $\Omega$ . The resonant enhancement is the reason why SFG, DFG, and SHG are often used for spectroscopic studies of molecules.



# Chapter 3

## Experimental setup

The aim of this thesis was twofold. The first goal was to study electronic transitions, especially in or near the band gap of fullerenes. Such transitions are situated in the region from one up to several eV which corresponds to the photon energies in the near infrared and in the visible. The other goal was the investigation of organic monolayers via vibrational sum frequency spectroscopy, which requires a tunable beam in the mid infrared. This is why a versatile experimental setup had to be developed.

The concept that was chosen is the generation of the required radiation in a two stage optical parametrical device, which in the first stage - starting from the third harmonic of a Nd:YAG laser - creates a tunable near infrared and visible beam using an optical parametrical generation (OPG) and amplification (OPA) process. This beam serves either for the fullerene experiments or for seeding the second optical parametrical stage (OPA) used for the creation of the mid-infrared beam. Such a system has been extensively described by Krause and Daum [8,9]. The advantage is that the wavelength can easily be tuned over the entire range (0.41 – 12.9  $\mu\text{m}$ ) [9], basically by angle tuning optical elements. The setup mounted in this work is inspired by this system and a similar system which has been mounted and also meticulously described by Himmelhaus [10]. Therefore most of the theoretical considerations, which are important when building up such a system for the first time are skipped here and I will rather focus on the particularities and parameters of our system.

## 3.1 Experimental setup for SH spectroscopy of electronic states

### 3.1.1 Source of the fundamental radiation and frequency tripling

The source of the radiation is an active-passive mode-locked Nd:YAG laser (Continuum, PY-61C-20) with a repetition rate of 20 Hz. As saturable absorber the Q-switch I (Exciton) is used. Via cavity dumping a single pulse is extracted from the pulse train in the oscillator. The wavelength is 1.064  $\mu\text{m}$  ( $9398\text{ cm}^{-1}$ ) and the pulse duration is about 35 ps [10]. By operating the oscillator with an output energy of between 2.6 and 3.0 mJ per pulse, and with the tension of the flashlights 20 V above the lasing threshold, the best pulse to pulse stability (3-4% rms) of the fundamental beam could be obtained. After it passed the single pass amplifier (flashlight tension 1.2 kV) the pulse energy can reach up to 45 mJ. The beam diameter is 9.5 mm.

For the operation of an optical parametrical generator and amplifier which generates output in the visible (up to 410 nm) and the near infrared, an intensive pump beam in the near UV is necessary. For this, the fundamental radiation is frequency doubled and then tripled with type II KD\*P (deuterated potassium dihydrogenphosphate,  $\text{KD}_2\text{PO}_4$ ) crystals [11]. The energy obtained for the third harmonic was maximally 12 mJ. Typical operating energies were however between 5 and 7 mJ for the third harmonic.

The energy output is not controlled by adjusting the high tension of the amplifier flashlamps but by detuning the delay between the amplifier and the oscillator lamps in order to avoid a change of the beam divergence. This variation in the divergence is due to a change of the optical properties in the Nd:YAG rod caused by a modification of the temperature distribution in the rod. In fact the temperature gradients in the YAG crystal do not only focus the beam but also lead to spatial inhomogenities in the beam which diminish the quality of the second and third harmonic beam. The KD\*P crystals are fixed right after the amplifier in the laser housing. Once again temperature drifts in the laser housing are the reason for a variation in the phase matching angles of the KD\*P crystals. Therefore they constantly have to be optimized until stationary conditions are reached after several hours. In this context

I put an additional air conditioning system into service which maintains the room temperature constant in the range of  $(22 \pm 1)^\circ\text{C}$ .<sup>1</sup>

### 3.1.2 The OPG-OPA for the visible and near infrared range

For the efficient generation of parametric light, beams with  $\text{TEM}_{00}$  mode should be used. This becomes evident when we look at a multimode laser beam which can be roughly considered as a beam with hot spots. The small dimension of these hot spots increases the so called walk-off effect and decreases the interaction length resulting in a drastic lowering of the conversion efficiency [2]. Additionally the energy density in hot spots is difficult to control and the high intensities can damage the optical elements. It is obvious from what was said in the previous section that an improvement of the spatial quality of the third harmonic beam (355 nm,  $28193\text{ cm}^{-1}$ ) is necessary. At first I did this by spatial filtering. The spatial filter consists of a two lens telescope with a sapphire pinhole with a diameter of  $100\ \mu\text{m}$  placed in the focus. This telescope equally serves to regulate the energy density of the pump beam.

Lithium borate ( $\text{LiB}_3\text{O}_5$ , or short LBO) crystals, cut for type I phase matching are used for the generation of the tunable light. They are heated to  $(50 \pm 1)^\circ\text{C}$  in order to prevent the absorption of water and thus the degrading of the crystals. Wavelength variation is performed by angle tuning of the crystals. For this they are mounted to step motors which allow control of the angle with a precision of 0.001 degree. The pump beam enters the first LBO crystal (OPG) where it creates parametric superfluorescence in a broad divergent beam, which is amplified in the second LBO crystal (OPA). Depending on the wavelength, the spectral width of the signal and idler components in the generated beam after the OPA is in the order of several ten wavenumbers in the whole tunable range from 4200 to  $24000\text{ cm}^{-1}$ . The only exception is a small range near the degeneration at  $14096\text{ cm}^{-1}$  where the width can reach hundreds of wavenumbers [9]. The spectral width of the tunable beam is small enough for the spectroscopy of the electronic transitions described in chapter

---

<sup>1</sup>Before installing this measure, there were temperature changes of more than six degrees during one day.

4.2 but it is too large for both the diffusion experiments (chapter 4.4) as well as for the vibrational sum frequency spectroscopy (chapter 5).

A remedy for this problem is to narrow the spectral width of the light generated in the OPG and then to amplify the spectrally narrowed beam in the OPA. This is why the pump beam is separated from the generated light by a standard dielectrical 355 nm mirror. Before being merged again with the pump beam in the OPA, the generated light can now be narrowed in its separate beam path (see Fig.3.1). For the parametrical amplification process in the OPA only one component (signal or idler) is necessary and the spectral width of the beam after the OPA is determined by the width of the seeding components [9]. Since the simultaneous narrowing of signal and idler component is not feasible, the idler component is blocked by a filter.

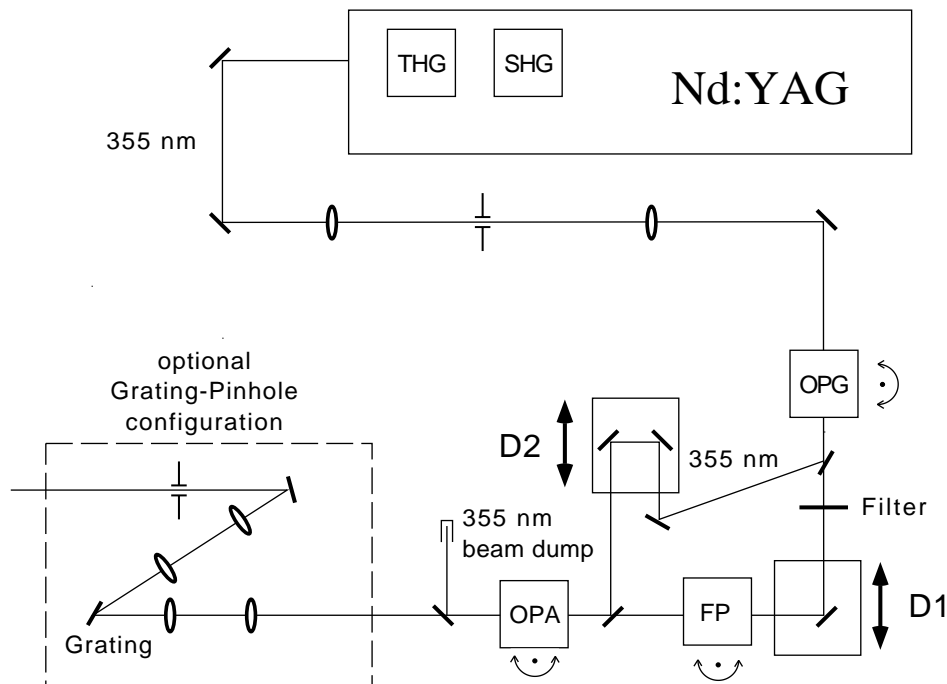


Figure 3.1: Setup for the OPG-OPA. D1, delay stage for adjustment of the spatial overlap of the beams (changes also temporal overlap). D2, new delay stage for independent adjustment of the temporal overlap (see text). FP, Fabry-Perot interferometer.



For spectral narrowing the signal component, a home-built Fabry-Perot interferometer is used. It narrows the band width of this component to about  $15 \text{ cm}^{-1}$ . The idler component is blocked with a filter.

With a separation between the transmission maxima of  $200 \text{ cm}^{-1}$ , the Fabry-Perot is well suited for the whole wavelength range, except for a small region near the degeneration at  $14096 \text{ cm}^{-1}$ . Here the bandwidth is larger than the distance between the transmission maxima. When working in this range, one of the maxima is selected by a subsequent grating-pinhole configuration. In order to prevent damage of the grating, the beam is expanded before the grating and contracted after it with two lens telescopes.

One important change to the former setup [12] is the decoupling of the adjustment for the temporal and the spatial overlap by introducing a variable delay line for the pump beam. This explains the rather unusual path of the pump beam (Fig.3.1). By introducing this modification, the output energy could be improved by a factor two on the one hand and on the other hand, switching between the configurations with and without Fabry-Perot interferometer was easy.

## 3.2 Experimental setup for vibrational SF spectroscopy

During the fullerene experiments (chapter 4) it became clear that the SF spectroscopy setup cannot be realized simply as an extension of the SH spectroscopy setup. This is why I built completely new the optical part of the setup. The reasons for this decision were the following:

Spectroscopy of vibrational states has much higher demands concerning wavelength control and bandwidth of the probing radiation as spectroscopy of electronic transitions due to the much smaller bandwidth of vibrational transitions. During the exciton diffusion experiments (chapter 4.4) we noticed wavelength drifts in the transmission spectrum of the Fabry-Perot interferometer due to its high sensitivity to temperature fluctuations. Thus, a different concept had to be applied for the control of bandwidth and wavelength (see chapter 3.2.2). Further points of which an amelioration was necessary were on the one hand the continuously changing quality of the fundamental beam

which also has considerable contributions of higher modes, since this results in a third harmonic beam of which the quality can not be sufficiently improved by the spatial filtering described in chapter 3.1.2. And on the other hand it was the continuous change of the phase matching angle of the KD\*P crystals due to temperature fluctuations in the laserhousing.

### 3.2.1 Fundamental beam and third harmonic

The most delicate point is the beam quality of the fundamental beam. It has its origin in the laser cavity and already the quality of the pulse which is ejected from the cavity is not satisfying. Replacing of the suspect elements in the cavity (backmirror and wedge which are integral parts of the dye cell, and the acousto-optic modelocker) brought a remarkable improvement of the pulse to pulse stability, but the beam profile leaves much to be desired. Even with the help of the Continuum engineers it could not be further improved. An additional problem of the laser is that the saturable absorber often deposits on the back mirror and on the window wedge. Thus the dye cell periodically had to be dismantled and cleaned. After the replacement of the pumping unit this problem has not reappeared yet. The next starting point for improvement is thus the manipulation of the already created beam.

Krause et al. compress the beam and let it travel twelve meters in order to let the higher modes propagate outside the beam where they do not disturb the conversion processes [8]. In order to get rid of the higher modes Himmelhaus [10] uses a kind of spatial filtering with a travel distance of eight meters involving a four meter telescope which reproduces the beam image from the exit window of the amplifier onto the entrance front of the frequency doubler. Both constructions could not be applied here due to geometrical restrictions. In order to improve the beam quality, we cut off the the outer part of the beam with a pinhole letting pass only the center which has a better quality. In the far field the center of the beam is additionally smoothed due to diffraction and from the effect that the higher modes propagate outside the beam.

This is why the KD\*P crystals are removed from the laserhousing. Now the beam is passed through a pinhole with adjustable diameter after which it is compressed by a factor two. Then it has to travel eight meters before its energy density and its divergence is adjusted for the KD\*P crystals by a three

lens telescope (see Fig.3.2).

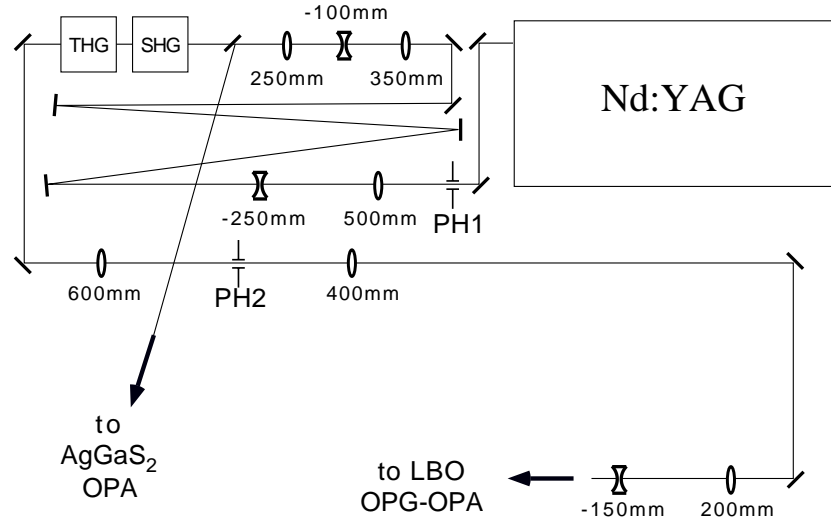


Figure 3.2: Scheme of the setup improving the profile of the fundamental and the third harmonic beam. PH1, adjustable pinhole with diameter  $\approx 4$  mm. PH2, sapphire pinhole with  $150 \mu\text{m}$  diameter.

In order to find the right diameter of the pinhole, the diameter is slowly diminished while observing the form of the beam right before the three lens telescope. The best compromise between energy throughput and form of the beam is when the beam which has originally a rectangular image in the far field, becomes round. This is at a pinhole diameter of about four millimeters.

Placing the KD\*P crystals outside the laserhousing also solved the problem of the continuously changing phase matching angle since the additional air conditioner maintains the temperature constant. Now the crystals are normally adjusted only once a day. The energy density in the first LBO crystal is adjusted by a two lens telescope which is placed right after the frequency tripling unit. Once again a spatial filter is realized by placing a sapphire pinhole with a diameter of  $150 \mu\text{m}$  in the focus. A second telescope which is right before the OPG-OPA unit regulates the divergence of the pump beam and thus the energy density in the second LBO crystal (Fig.3.2).

### 3.2.2 The OPG-OPA for the visible and near infrared range

The concept of narrowing of the spectral width with the Fabry-Perot interferometer has been given up, despite the tempting simplicity of the adjustment, since the required temperature control, would have been too costly in terms of time. Instead I opted for a reliable grating slit configuration (see also [10]). In fact once adjusted it never caused problems and is completely maintenance-free. In this configuration the signal and idler components which are generated in the OPG are expanded by a telescope with two achromate lenses (Spindler & Hoyer) in order to illuminate a large portion of the diffraction grating (1200 lines/mm). A second achromate telescope with a variable slit in the focus accomplishes the monochromatisation by selecting a small spectral width of the signal component (Fig.3.3).

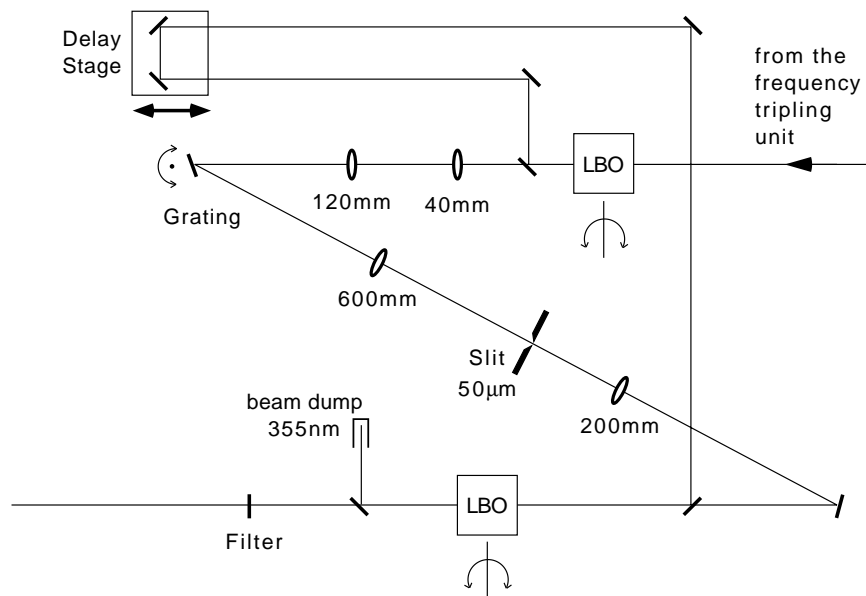


Figure 3.3: The LBO-OPG-OPA with conventional monochromator. The 355 nm pump beam is split off after the first LBO crystal and passes the delay line before being merged with the narrowed signal component in the second LBO crystal. The monochromator consists of four achromate lenses, a grating, and a slit. The output is tunable from 4200 to 24000  $\text{cm}^{-1}$ .

It is important that the second telescope inverses the action of the first one with a high precision in order not to alter the spatial overlap with the pump beam in the OPA during the angle tuning. This would result in a drastically lowered energy output. Figure 3.4 shows the energy output of the LBO-OPG-OPA in the range from 14000 to 24000  $\text{cm}^{-1}$ .

### LBO-OPG-OPA Output

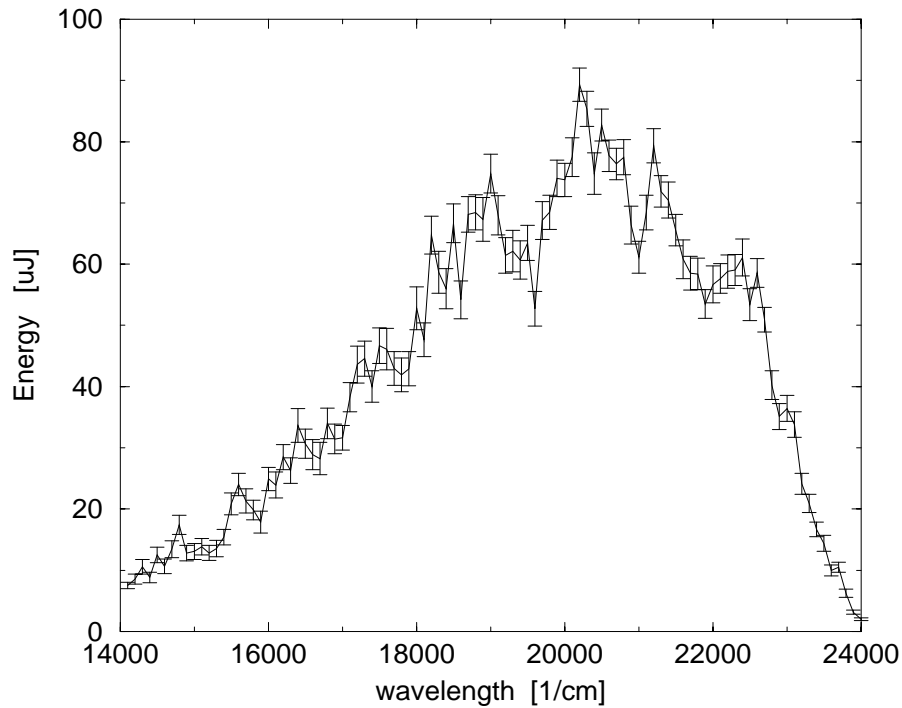


Figure 3.4: Energy output of the OPG-OPA-unit with a width of the slit of  $50 \mu\text{m}$  as function of the wavelength of the signal component (14096 - 24000  $\text{cm}^{-1}$ ). The complementary idler component (14096 - 4192  $\text{cm}^{-1}$ ) has not been separated and contributes to the energy.

The spectral width of the LBO-OPG-OPA has been measured directly with a Mc-Pherson Monochromator at  $14100 \text{ cm}^{-1}$  and at  $21600 \text{ cm}^{-1}$ . The lowest width obtained is  $4 \text{ cm}^{-1}$  for  $14100 \text{ cm}^{-1}$  and  $12 \text{ cm}^{-1}$  for  $21600 \text{ cm}^{-1}$ . The width of the slit in these cases was  $50 \mu\text{m}$ . With the slit completely open (3

mm) the spectral width only increases to  $40 \text{ cm}^{-1}$  and  $18 \text{ cm}^{-1}$ , respectively. The reason for this is that in this case the pump beam acts as aperture in the second LBO crystal. For further narrowing of the bandwidth, a grating with a higher line density should be used<sup>2</sup>.

### 3.2.3 The OPA for the mid infrared

With the LBO-OPG-OPA described in chapter 3.2.2 narrow band radiation down to  $4200 \text{ cm}^{-1}$  can be created. In the second stage this radiation is used to seed another OPA unit. This unit consists of two silver gallium thioate ( $\text{AgGaS}_2$ ) crystals, cut for type I phase matching, which are placed in collinearly and pumped by the fundamental laser beam ( $9398 \text{ cm}^{-1}$ ). Through this difference frequency mixing process the accessible wavelength range can be extended down to  $1200 \text{ cm}^{-1}$ , thus covering an important range for vibrational spectroscopy (see figure 3.6). The created radiation has the same spectral width as the seeding radiation under the condition that the pump density is low enough so that the  $\text{AgGaS}_2$  crystals do not generate superfluorescence.

The pump beam is a portion of 15 percent<sup>3</sup> of the fundamental beam, split off directly before the frequency tripling unit (Fig. 3.2). Its energy density and divergence is also adjusted by two telescopes. One is placed at the beginning of the delay distance and the other right before the  $\text{AgGaS}_2$  crystals. The beam profile is smooth due to the initial "cleaning" procedure. Its energy is about 1 mJ and its energy density in the center is adjusted with the help of a 1 mm pinhole to  $200 \mu\text{J}$  per pulse ( $\cong 0.5 \frac{\text{GW}}{\text{cm}^2}$ ). Great care has been taken in order not to surpass this energy density, which is a factor of two below the damage threshold<sup>4</sup>. Other groups report under similar operation conditions a blackening of the crystal surfaces after several month of service which can be removed by polishing the surfaces. After one year our crystals show no sign of damage. The  $\text{AgGaS}_2$  crystals are mounted on stepping motors and

---

<sup>2</sup>gratings with 2400 lines/mm are available

<sup>3</sup>This is the maximum which can actually be taken off in order to leave enough energy for the LBO-OPG-OPA unit. One can take off more when the conversion efficiency from the fundamental to the third harmonic is increased for example by using LBO crystals instead of  $\text{KD}^*\text{P}$  crystals

<sup>4</sup>The low damage threshold is also the reason why the direct creation of the mid infrared light without seeding is not possible

heated to 50°C. Like the LBO crystals they are cut in a way that the second crystal compensates the displacement of the beam caused by the first, so that wavelength ( $\cong$  angle) tuning does not alter the beam position. Unfortunately, the cut of the two crystals differs of about 3 degrees which results in a slight angular motion of the beam, which can cause a slow varying intensity in the recorded spectra. For the sum frequency spectra only the idler component is used. The signal component is blocked together with the rest of the pump beam by a filter (Laser Components LCRL-2500-F). The direction of the mid infrared beam is adjusted through two pinholes and for the adjustment of the further experiment a helium-neon laser is used as tracer which is coupled in with a removable mirror (Fig.3.5).

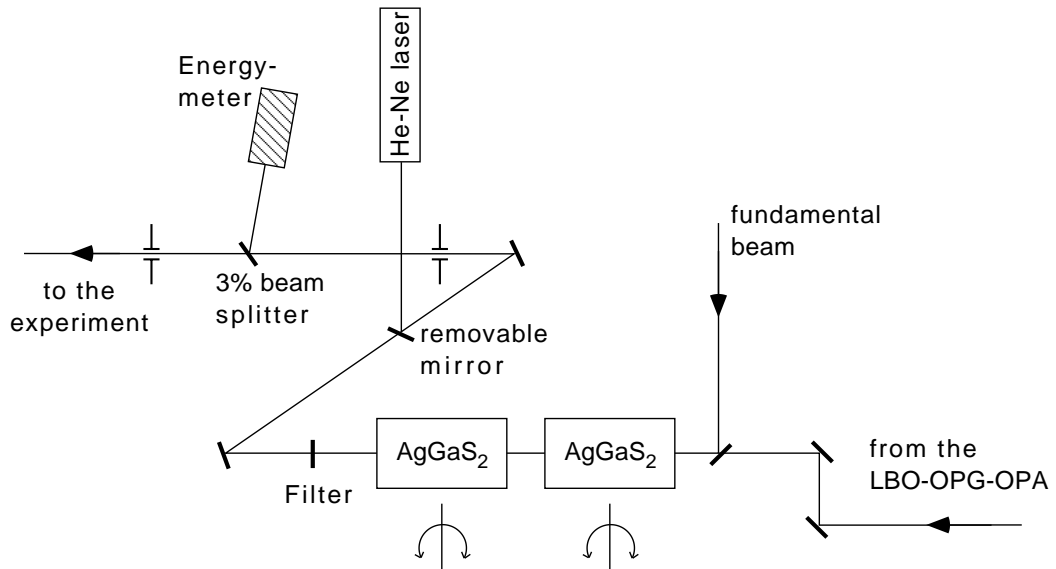


Figure 3.5: The OPA for the mid infrared. The crystals are pumped with a part of the fundamental beam and the seeding radiation is the idler component from the LBO-OPG-OPA. See also text.

Energies of typically 100  $\mu\text{J}$  per pulse at  $3000\text{ cm}^{-1}$  can be obtained routinely. Figure 3.6 shows the energy dependence as a function of the wavelength.

The spectral width for the LBO-OPG-OPA has been determined in section 3.2.2 to  $12\text{ cm}^{-1}$  at  $21600\text{ cm}^{-1}$ . This corresponds also to  $12\text{ cm}^{-1}$  at  $2805\text{ cm}^{-1}$ . In the spectra, peaks with about the same width should therefore easily

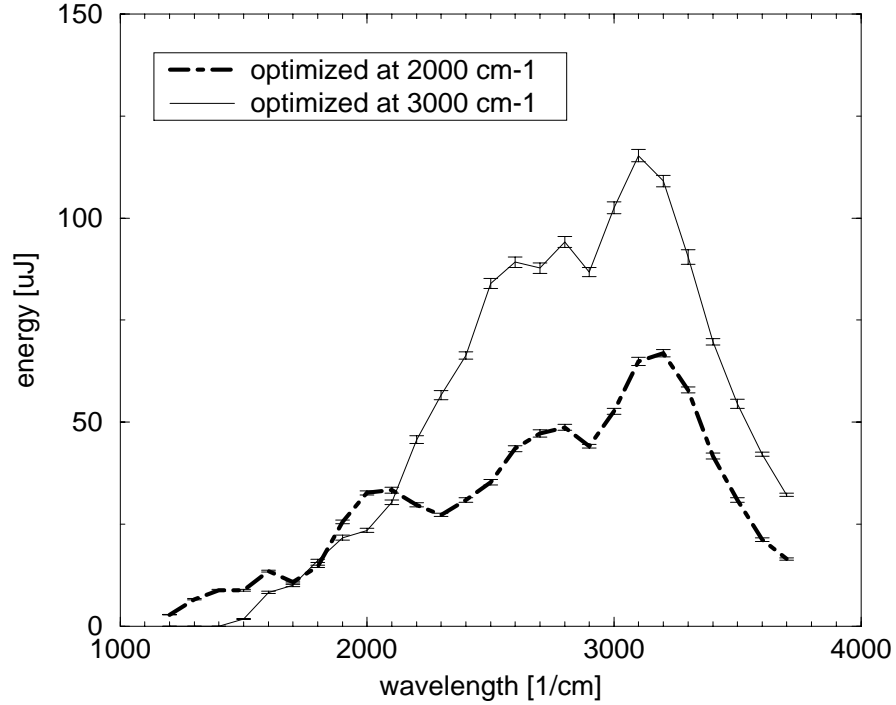
AgGaS<sub>2</sub>-OPA Output

Figure 3.6: Energy output of the AgGaS<sub>2</sub> OPA as function of the wavelength of the idler component (3700 - 1200 cm<sup>-1</sup>). For one measurement the crystals have been adjusted at 3000 cm<sup>-1</sup> (solid line) and for the other one at 2000 cm<sup>-1</sup> (dashed line). The corresponding signal component (5698 - 8198 cm<sup>-1</sup>) is blocked by a filter.

be resolved if there is no broadening due to broadband optical parametrical generation in the AgGaS<sub>2</sub> crystals. In order to test this, the transmission spectrum of a polystyrene foil is recorded and compared to a conventional FTIR transmission spectrum of the same foil, which has been recorded with a resolution of 4 cm<sup>-1</sup> (Fig.3.7).

All peaks are resolved, which signifies that there is no enlargement of the spectral bandwidth in the AgGaS<sub>2</sub>-OPA due to parametric generation. The peaks in the FTIR measurement are slightly sharper than the peaks recorded



## Spectral resolution and calibration

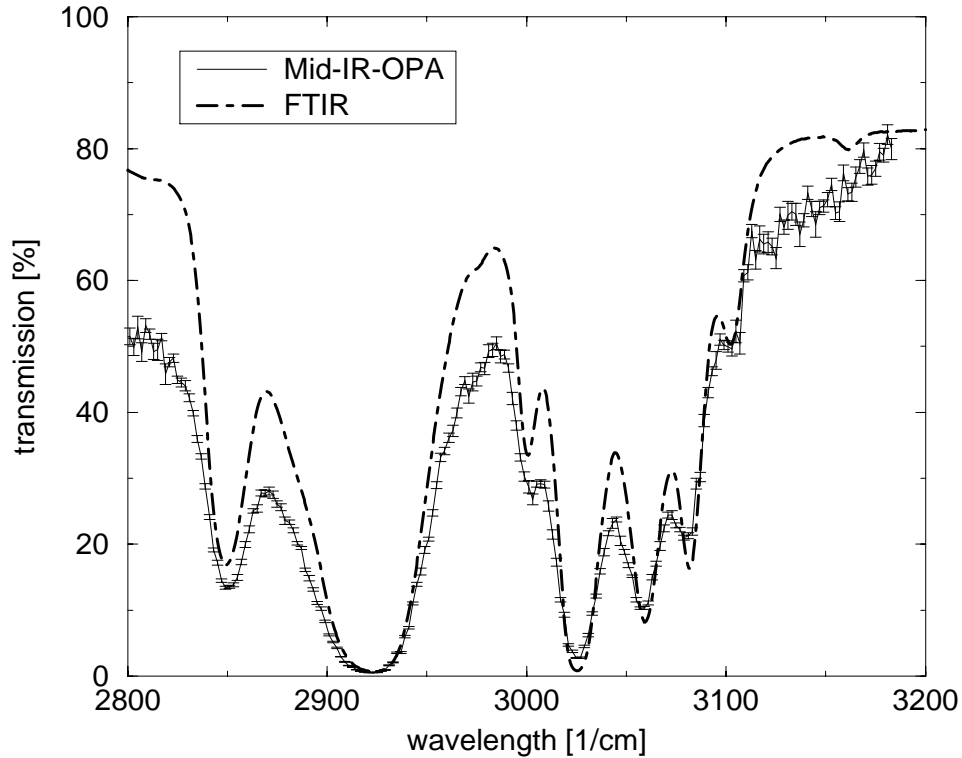


Figure 3.7: Transmission spectrum of a polystyrene foil, recorded with a FTIR spectrometer (dashed line). The solid line is the energy of the laser beam recorded after transmission and is scaled to 80% at  $3200\text{ cm}^{-1}$ . All transmission peaks are resolved.

with the tunable laser beam due to the larger bandwidth of the latter. The comparison of these two spectra additionally gives the wavelength calibration. Day to day changes of the wavelength calibration of about  $10\text{ cm}^{-1}$  are possible. The reason for this is that the beam alignment in the setup performed at the beginning of the day is never exactly identical with the alignment of the day before. During the day the wavelength calibration does not shift significantly. This is why the absorption spectrum is recorded once a day. The wavelength calibration of the sum frequency spectra is better than  $2\text{ cm}^{-1}$ . When record-

ing spectra in ranges far from the absorption resonances of the polystyrene, other suitable absorption lines, like the center of the CO<sub>2</sub> absorption line at 2348 cm<sup>-1</sup> can be used.

### 3.3 Normalization strategies

The measures taken to eliminate thermal drifts in beam profile, in the phase matching angle of the frequency tripling unit and in the monochromator of the LBO-OPG-OPA result in an excellent long term stability of the whole laser system. Several hours of measurement can be achieved without loss of energy in the beams, thus greatly reducing the adjustment time with respect to the previous setup described in section 3.1.

The limiting factor now is the pulse to pulse stability of the laser. Typical pulse to pulse fluctuations of the system are shown in the following table.

Beam	1064 nm	532 nm	355 nm	LBO-OPG-OPA	AgGaS <sub>2</sub> -OPA
Fluctuations (rms)	4 %	7 %	9 %	30 %	15 %

The amplitude of these fluctuations causes substantial noise in the spectra thus inducing long acquisition times. In order to reduce the required time of acquisition, different strategies have to be applied.

For the SH measurements, where the tunable light from the LBO-OPG-OPA is used, all shots with an energy below a certain threshold, which normally is set to 50 % of the average pulse energy, are omitted. The energy of a shot is monitored by measuring the reflection of the beam from the filter which selects signal or idler (see figure 3.1).

For the SF-spectroscopy, the same procedure is applied by monitoring a small portion of about 3 % of the mid infrared beam which is reflected at a calcium fluoride (CaF<sub>2</sub>) window (see figure 3.5). Additionally the SF-intensity per shot is divided by the monitored energy of this shot. This normalisation is reasonable because the number of generated sum frequency photons is linear in the energy density of the visible beam (see equation 2.31). The normalisation to the pulse energy of the visible beam, like it is done for example by [13], has not been done because the visible beam is more stable.

# Chapter 4

## Fullerenes

### 4.1 Generalities

When in 1985 Kroto et al. searched the geometric form of  $C_{60}$  clusters they proposed, inspired by the form of the geodesic domes built by the architect Buckminster Fuller, that  $C_{60}$  is a truncated icosahedron, and named it buckminsterfullerene. The geometry of a truncated icosahedron is known since a long time. About 23 centuries ago, Archimedes of Syracuse truncated polyhedra into such forms including, for the first time, the truncated icosahedron, part of a family called the *Archimedean solids*. Figure 4.1 shows the way from a normal icosahedron to a truncated icosahedron. If carbon atoms are placed at the 60 vertices of the truncated icosahedron, the form of a  $C_{60}$  molecule is obtained. The  $C_{60}$  molecule forms the cage of a polyhedron and the first cages of polyhedra have been sketched by Leonardo da Vinci (see Fig.4.2). The cage of the  $C_{60}$  molecule is built out of hexagons and pentagons. Closed cage molecules containing only hexagonal and pentagonal faces are by definition called fullerenes [14]. Euler's theorem for polyhedra combines the number of faces with the number of edges and vertices. From this one can derive that fullerenes contain always exactly 12 pentagonal faces. It also follows that the smallest possible fullerene is  $C_{20}$ , which would form a regular dodecahedron with 12 pentagonal face and no hexagonal faces. It is, however energetically unfavorable for two pentagons to be adjacent to each other, since this would lead to higher local curvature on the fullerene ball and hence to more strain [14].

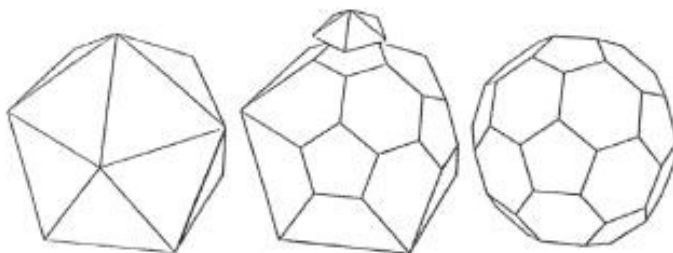


Figure 4.1: The way from a regular icosahedron to a truncated icosahedron. For the regular icosahedron the vertices are centers of fivefold symmetry, triangular faces are centers of threefold symmetry, and edges are centers of twofold symmetry. The entire object has inversion symmetry. The symmetry elements remain the same for the truncated icosahedron.

This is why fullerenes are more stable when pentagons are not adjacent but isolated by hexagons. The smallest fullerene to satisfy this so-called *isolated pentagon rule* is  $C_{60}$  which has 20 hexagonal faces and which is the most stable carbon fullerene. The next bigger fullerene which satisfies the isolated pentagon rule is  $C_{70}$  which is also stable. It has 25 hexagons and its shape is similar to a rugby ball.

Fullerenes differ from diamond and graphite in the way of the hybridization of the  $2s$  and  $2p$  orbitals of the carbon atoms. Whereas the carbon in the diamond structure is  $sp^3$  hybridized entailing the tetrahedral bond angle of  $109.5^\circ$  and four equivalent  $\sigma$ -type bonds, in graphite the hybridization is  $sp^2$  resulting in three planar  $\sigma$ -type bonds with a bond angle of  $120^\circ$ . The out-of-plane  $p$ -orbitals result in delocalized  $\pi$ -bonds and a weak interplanar bonding. In order to account for the curvature in the  $C_{60}$  molecule, the hybridization of the carbon atoms is intermediate, yet near to the graphite case. Thus every carbon atom is bound via three  $\sigma$ -like bonds to its three nearest neighbors and the  $p$ -like orbitals are delocalized over the shell. The  $\sigma$ -orbitals form strong bonds and lie thus far below the Fermi level and therefore do not significantly contribute to the electronic transport or optical properties, which are dominated by the  $\pi$ -orbitals lying near the Fermi energy. Thus the analysis of these properties can be restricted to the 60  $\pi$  electrons of the  $C_{60}$  molecule.



Figure 4.2: A design of a truncated icosahedron, first published in the book “De Divina Proportione” of Luca Pacioli (Venice, Pagani 1509). It is generally believed that Leonardo da Vinci made the illustrations for this book.

In the simplest way, the level filling of the 60  $\pi$  electrons can be obtained by filling the electronic states according to their orbital angular momentum while taking into account the Pauli principle. It follows immediately that 50  $\pi$  electrons fully occupy the angular momentum states from  $\ell = 0$  through  $\ell = 4$ , so that the 10 remaining  $\pi$  electrons are available to start filling the  $\ell = 5$  state. In spherical symmetry, the  $\ell = 5$  state can accommodate 22 electrons. In icosahedral symmetry however the  $\ell = 5$  state splits into the  $h_u + t_{1u} + t_{2u}$  irreducible representations [14]. The level of lowest energy is the fivefold  $h_u$  level, which is thus completely filled by the 10 remaining  $\pi$  electrons. The  $t_{1u}$  and  $t_{2u}$  level are both threefold degenerate. According to Hückel calculations [15], the lowest unoccupied level is the  $t_{1u}$  level and the

next higher level is not the  $t_{2u}$  level, but the  $t_{1g}$  level which is pertinent to the states with an angular momentum of  $\ell = 6$  (see Fig.4.3).

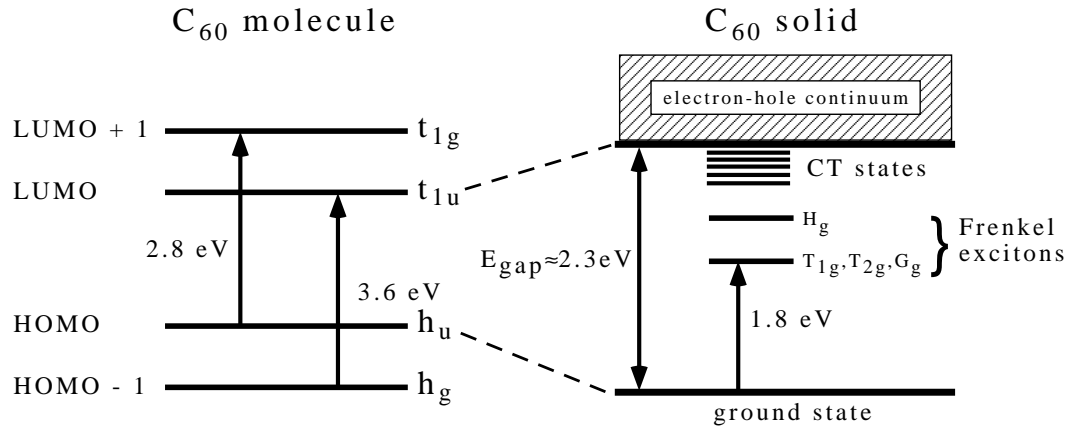


Figure 4.3: The electronic levels of the  $C_{60}$  molecule in the one-electron picture (left). Dipol allowed transitions are from HOMO (highest occupied molecular orbital) the LUMO+1 (lowest unoccupied molecular orbital) and from HOMO-1 to LUMO. Right: The excitonic electronic levels in the band gap in solid  $C_{60}$  are derived from the lowest lying singlet electron-hole multiplets of an isolated  $C_{60}$  molecule.

Optical excited states are formed by promoting one of the electrons from an occupied to an unoccupied level by absorption of a photon. For an electron promoted from the  $h_u$  level in the  $t_{1u}$  level the symmetry of the resulting electron-hole pair is determined by the direct product of the symmetries of the electron ( $t_{1u}$ ) and the hole ( $h_u$ ) which results in  $t_{1u} \otimes h_u = H_g + T_{1g} + T_{2g} + G_g$ . These multiplets are singlet states due to the symmetric parity of the space dependent representations. In *solid*  $C_{60}$  the electronic excitations are similar to the excitations in the isolated molecule, since the interaction between the molecules is small. However in the solid a band structure is formed and the energy of the lowest lying singlet excitons is about 100 meV lower than in the isolated molecule [14].

In the following sections we investigate  $C_{60}$  and  $C_{70}$  by means of SH spectroscopy. Then we will study the energy transfer of excited  $C_{60}$  molecules to gold and silver when the molecule is situated near the surface of the metal. The third point is the diffusion of excitons in photoexcited  $C_{60}$ .

## 4.2 Second-harmonic spectroscopy of fullerenes

### 4.2.1 Introduction

Fullerenes are known to have large non-linear polarizabilities which have been attributed to the delocalization of  $\pi$  electrons on the carbon shell. Even though the initial hopes of extraordinarily large efficiencies have not become true the non-linear properties of the fullerenes remain a field of substantial interest. Second-harmonic generation (SHG) spectroscopy can contribute to the spectroscopy of solids with a dipole-forbidden band-gap. Due to its resonance enhancement one can observe signal maxima in SHG spectra which can be due to electronic transitions at the fundamental photon energy (the frequency of the incident laser beam) or at the doubled energy (the emitted, frequency doubled light). The symmetry of the  $C_{60}$  solid and the selection rules of the SHG process forbid the observation of electric dipole (ED) transitions in the bulk so that the intensity of these transitions will be strongly reduced due to a restriction of the generation process to the surface. This facilitates the observation of forbidden transitions which can generate a SHG signal also in the bulk region. Theoretical studies [16, 17] have elucidated different aspects of SHG from  $C_{60}$  and  $C_{70}$ . The relative importance of forbidden transitions and allowed transitions is, however, rarely addressed [18, 19] and still requires experimental studies.

In this chapter we present SHG spectra of  $C_{60}$  and  $C_{70}$  thin films over a wide spectral range employing a tunable OPG/OPA apparatus. Between the fundamental photon energies 1.0 eV and 2.3 eV we find four resonances for  $C_{60}$  and two for  $C_{70}$ . We discuss the assignment of the observed peaks and their strengths. A second subject of this chapter is the study of transient suppression of the non-linear signal by excitation of the electronic system. A similar change of non-linear efficiency is known for third order non-linear effects [20, 21]. An efficient suppression by visible and UV pump pulses for pristine  $C_{60}$  samples has already been demonstrated for the resonance at a fundamental frequency of 1.18 eV [22]. Here we investigate the response to electronic excitation for other SHG resonances.

### 4.2.2 Experimental

Fullerene thin film samples are prepared by evaporation of  $C_{60}$  (MER corporation >99.9% pure) or  $C_{70}$  (MER >99% pure) on amorphous quartz discs.  $C_{60}$  and  $C_{70}$  were evaporated from a graphite crucible at 670 K and 715 K, respectively, after having been degassed at 500 K for more than 24 h. Evaporation times of 10 hours give a film thickness of about 100 nm. During evaporation the substrate is heated to 415 K in order to increase the crystallinity of the film. A typical absorption spectrum is shown in figure 4.4.

The SH measurements were performed at room temperature in a high vacuum chamber. Tunable pulses have an energy of 10-100  $\mu\text{J}$ . The pulses are focused by a lens to a spot smaller than 1  $\text{mm}^2$  on the sample. Displacement of the lens allows to adjust the energy density so that the beam stays safely below the damage threshold. The spectral width of the pulses in the scanning range is <0.01 eV. Only between 1.70 eV and 1.80 eV the spectral width of the tunable beam exceeds 0.02 eV reaching a sharp maximum of about 0.13 eV at 1.75 eV. The detector resolution of 2 nm corresponds to <0.02 eV over the entire scanning range. The SH signal is generated at the sample in reflection

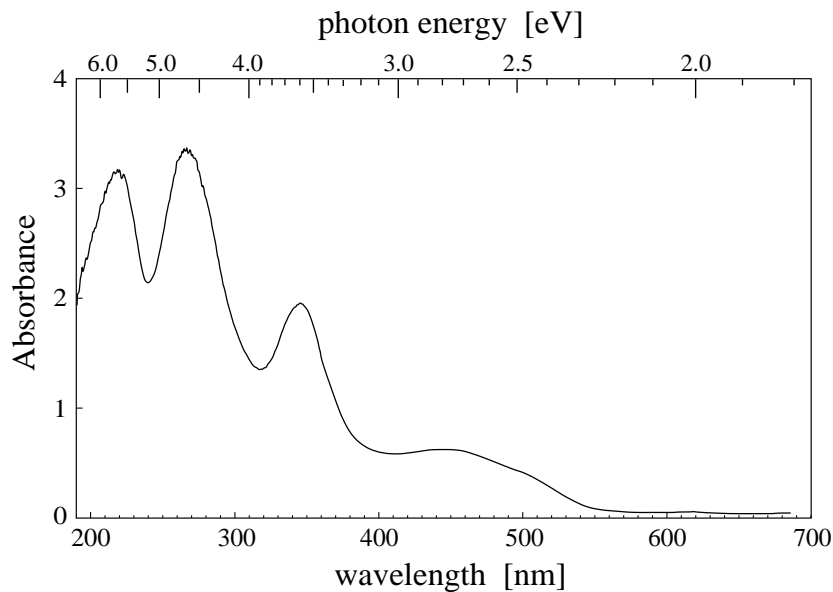


Figure 4.4: Absorbance spectrum of a  $C_{60}$  sample in transmission geometry.



geometry with a beam incident at an angle of  $45^\circ$ . The SH signal arising from the amorphous quartz substrate is below the detection limit. In the incident beam one of three commercial band-pass filters with transmission ranges 2700-850, 1000-700, and 750-400 nm clean the beam from SH intensity generated along the beam path. The reflected fundamental beam which is collinear with the generated SH intensity is attenuated by 750-400 or 400-240 nm band pass filters, or a  $\text{CuSO}_4$  solution before the SH photons pass into a double monochromator with a standard bialkali photomultiplier tube.

Repetitive spectral scans with alternating scan direction are performed by stepping the wavelength of the incident beam and scanning the monochromator at the doubled frequency. Because the filters in the beam path have to be exchanged to obtain the full scan range and the beam energy varies with wavelength the spectrum had to be divided in 5 overlapping ranges (0.85-1.15, 1.0-1.3, 1.17-1.77, 1.74-2.16 and 1.95-2.30 eV). Simultaneously with the measurement of each spectral range a spectrum with a crystalline quartz plate (WP) in the beam path is recorded. The intensity maxima obtained in the WP scans are interpolated by a spline function and this function serves to normalize the spectrum. Finally, the complete spectrum is obtained by scaling the five sections with respect to each other in the overlapping regions.

The resulting spectra are averaged over several samples. Care was taken to avoid significant polymerization of the films. Polymerization of  $\text{C}_{60}$  proceeds continuously with the exposure to light at wavelengths in the absorption region of  $\text{C}_{60}$  (visible to UV) [23]. The scan intervals are therefore measured for each of the samples beginning with the lowest energy range and finishing with the highest energy range. The measured spot on a sample is frequently changed and a sample is discarded after a few hours of exposure to the laser pulses in the visible range. In addition, we avoid any exposure of a sample to light from the room illumination.

The SHG suppression measurements are made in a pump-and-probe scheme. With the tunable probe beam set on the peak of a selected SHG resonance a 30 ps pump beam at 3.49 eV photon energy generates the electronic excitation of the sample. The pump pulse is incident at an angle of about  $40^\circ$  from the sample normal. Transients are recorded by varying the time delay of the probe pulse with respect to the pump pulse.

### 4.2.3 C<sub>60</sub> SHG spectroscopy

The SHG spectrum of C<sub>60</sub> (Fig.4.5) shows three pronounced resonances and a weak one. In the following the peak assignment will be discussed. The observed transitions and resonance conditions are illustrated in Fig.4.6

Within the measured range, two major ED transitions are known to occur. They correspond to transitions between the HOMO and the LUMO+1 (2.8 eV) and between the HOMO-1 and the LUMO (3.6 eV). In the SHG spectrum (Fig.4.5) they appear at the fundamental energies 1.35 eV and 1.82 eV, respectively. The allowed transition at 1.35 eV is weak even compared to the observed forbidden transitions (see below). This may result from the fact that its transition dipole moment is small and due to the symmetry rules of SHG only an interface contribution can be observed.

For the dipole forbidden electronic transitions between the HOMO and LUMO states four transitions can be derived. They are between the A<sub>g</sub> ground state and excitonic states of T<sub>1g</sub>, T<sub>2g</sub>, G<sub>g</sub> and H<sub>g</sub> symmetry. Whereas the first three states are almost degenerate and were calculated to lie within an interval of 0.1 eV the last one is higher by approximately 0.5 eV [24, 25]. The lowest singlet excitonic state in the solid has been shown to have a majority T<sub>1g</sub> symmetry [26, 27]. In the solid it has been assigned to observed resonances at 1.80 eV [28] and 1.846 eV [29]. It is reached from the ground state by a magnetic dipole (MD) transition and is another transition which can be assigned to the SHG peak at 1.82 eV. In accordance with its substantial intensity this peak is doubly resonant as reported already by Koopmans et al. [28]. The peak at 1.18 eV lies at a one photon energy which is below the lowest excitonic state in C<sub>60</sub> (1.55eV [30]). It must thus be resonant at the two photon energy, namely at 2.36 eV, which is 0.54 eV above the T<sub>1g</sub> state and may thus be assigned to the electric quadrupole (EQ) transition to the H<sub>g</sub> state [18]. We remark that a peak observed in electroabsorption spectroscopy at 2.35 eV was assigned to a charge transfer (CT) exciton [31, 32] which can contribute in SHG spectroscopy. It may, in fact, be that both states are identical as the H<sub>g</sub> state lies already close to the band gap and possesses a much larger CT character than the lower excitons [24].

The resonance at 2.02 eV lies in the range of the above mentioned excitonic states. However, it is too high in energy (0.2 eV above T<sub>1g</sub>) to be assigned to the T<sub>2g</sub>, or the G<sub>g</sub> state derived from the HOMO-LUMO transitions. There

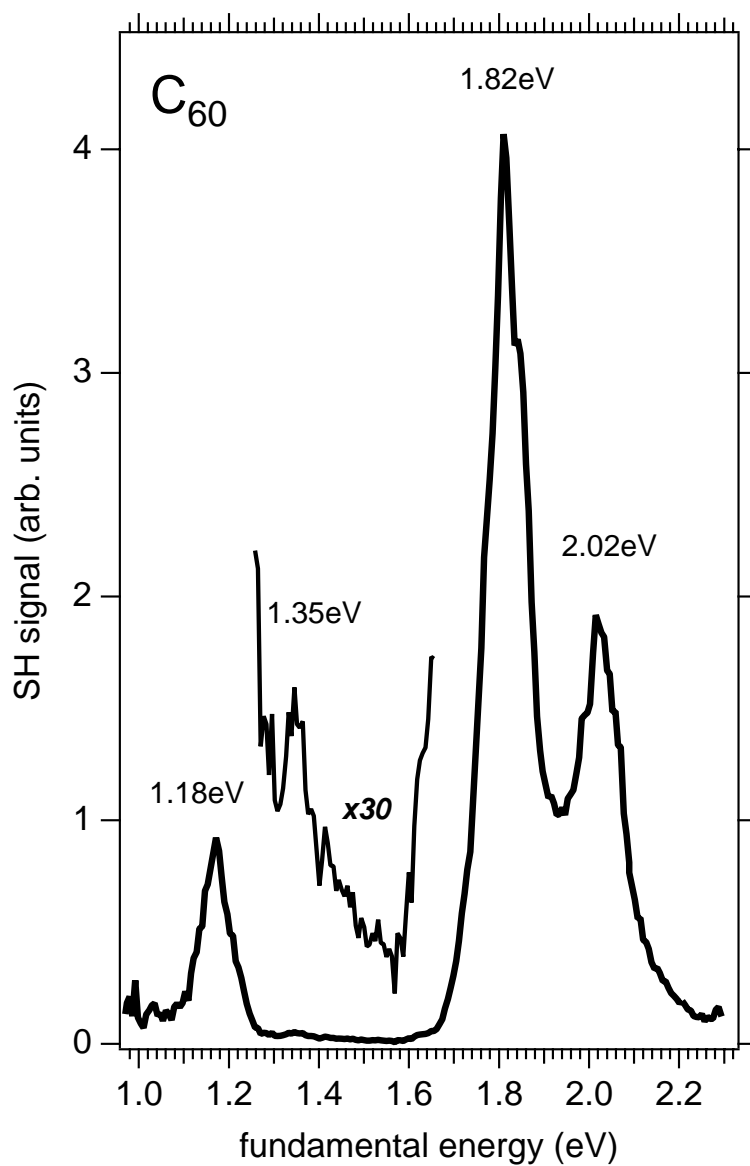


Figure 4.5: C<sub>60</sub> thin film SHG spectrum. The incident beam is s-polarized. The energy values indicate the peak positions (see also Table 4.1).

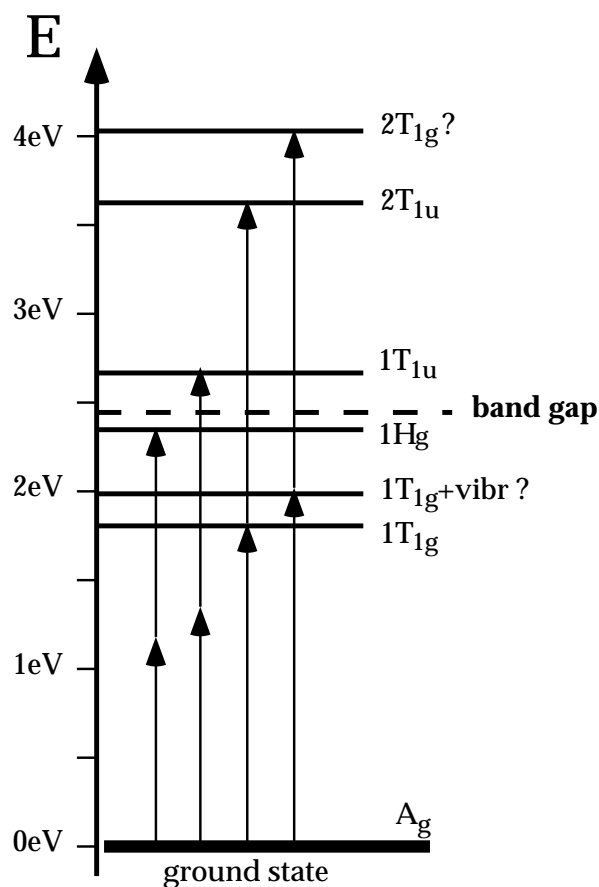


Figure 4.6: Assignment of the four resonances in the C<sub>60</sub> spectrum (Fig.4.5) to excitonic transitions in C<sub>60</sub>. The resonance conditions are indicated by the arrows. For assignments with question marks please refer to the discussion in the text.

are three possible origins of the peak: It can (a) be a transition to a T<sub>2u</sub> state (obtained for an electron in the LUMO and a hole in the HOMO-1) which was found in a calculation only 0.15 eV above the G<sub>g</sub> state and confirmed at 2.07 eV by experiment for matrix isolated molecules [33]. (b) It can be a vibronic transition based on the T<sub>1g</sub> electronic state by coupling to a vibration near 1600 cm<sup>-1</sup>. Finally, (c) it can be due to a transition at the doubled energy at 4.04 eV. Concerning case (a) the electronic T<sub>2u</sub> transition is of high

Observed SHG peaks of C <sub>60</sub>		
peak energy (eV)	FWHM (eV)	relative peak height
1.18	0.08	0.2
1.35	0.06	0.005
1.82	0.11	1.0
2.02	0.12	0.3-0.5

Table 4.1: Resonance positions, widths and relative peak heights for the four observed transitions in Fig.4.5. The proposed assignment is represented in Fig.4.6.

multipole order and should be much weaker than MD or EQ transitions. Concerning case (b) several vibrational modes are located near  $1600\text{ cm}^{-1}$ . If the intensity distribution was similar to the case of molecular spectroscopy we may in fact expect an intensity maximum between  $1400\text{ cm}^{-1}$  and  $2000\text{ cm}^{-1}$  [33]. The slow decrease of the 1.82 eV peak on its high energy side also suggest a vibrational origin. However, we cannot expect that the coupling to vibrations alone can be sufficiently intense to compensate for the loss of the double resonance condition due the displacement from the 3.6 eV transition. Even in the case of Herzberg-Teller active vibrations which lead to a well pronounced peak in low temperature absorption spectra near 2.0 eV [34,35] the transition would not remain strong as it would gain intensity only at the surface but not in the bulk. We would have a situation comparable to the one of the ED transition at 1.35 eV. In order to give an explanation of both, the substantial intensity in the 2.02 eV peak as well as the absence of a peak at 1.01 eV we propose a transition which is resonant near 4.04 eV. A peak at 1.01 eV would be expected for a transition at 2.02 eV which is strong and not doubly enhanced. Making a choice for the assignment with the possibly highest intensity we propose a double resonance with a transition at 4.04 eV and the vibrational structure of the T<sub>1g</sub> state peaking at 2.02 eV. The transition at 4.04 eV might correspond to a broadened ED transition calculated to appear about 0.3 eV above the 3.6 eV resonance [25]. However, as absorption spectra show a minimum at 4.0 eV it is more probable, that the peak is due to a transition between HOMO-1 and LUMO+1 states some 0.6 eV above the 3.6 eV ED transition [25] which provides states of T<sub>1g</sub> and H<sub>g</sub> symmetry reached from the ground state by MD and EQ transitions, respectively. Calculations of the nonlinear suscepti-

bility discussed below indicate that there is no 2.02 eV transition of strong EQ character which suggests an ED or MD transition at 4.04 eV.

The full peak width at half maximum of the resonances range from 0.06 eV to 0.12 eV (see Table 4.1). It is evident from the discussion in the experimental section (4.2.2) that these widths contain only negligible contributions from the instrumental resolution. The resonances are much sharper than the structures in absorption spectroscopy of the  $C_{60}$  solid [36–38] as can also be seen by comparison with Fig.4.4. Below room temperature still smaller line widths have been observed by SHG spectroscopy [39]. A small peak width can be expected for the lowest excitons from their band width as has been shown by Eder et al. [40]. On the other hand line widths of ED transitions in solid  $C_{60}$  are larger than 0.2 eV. One reason is the efficient decay of the molecular state to free carrier states. It is surprising that the line width of the peak at 1.35 eV which corresponds to the ED transition to the  $1T_{1u}$  state at 2.7 eV is the sharpest line in the spectrum. The decay must therefore still be comparatively slow for the  $1T_{1u}$  state. Other contributions to line broadening (e.g. due to vibrations) contribute less to SHG spectra than to absorption spectra. In a similar line of arguments the narrow line width of the 2.02 eV peak supports an assignment to a double resonance rather than a single resonance at 4.04 eV.

We shortly remark that no SHG peak is found at the spin-forbidden excitation of the lowest triplet exciton at 1.55 eV [30].

Comparison with the literature shows that the peak at 1.82 eV confirms very well position and width of the resonance first found by Koopmans et al. [28]. A significant SH signal is also found for a fundamental energy of 1.165 eV which was the energy of the study at fixed wavelength by Wilk et al. [18]. Our measurement demonstrates that this study was in fact done close to the maximum of the resonance. The observation of a resonance at 2.02 eV in a sum-frequency generation (SFG) measurement was only recently reported [41]. That work is a non-linear spectroscopic study on  $C_{60}$  extended to SFG and temperature dependent measurements thus presenting additional information to our study. SFG allows to lift the  $\omega - 2\omega$  ambiguity present in SHG. It is reported that at 78 K the 2.02 eV mode is not observed in the SHG configuration (i.e. with the second harmonic frequency at 4.04 eV). The difference to our experiment is the low temperature and the much longer pulse length (8 ns). The 2.02 eV mode is, however, observable if the sum frequency is at 3.5 eV due to double resonance enhancement. It remains smaller than

one tenth of the resonance at 1.82 eV. This difference in observability suggests that no resonance of a strength comparable to the 3.5 eV resonance is present at 4.04 eV. It is further shown that while the 2.02 eV mode exhibits about the same intensity at 78 K and 300 K the 1.86 eV resonance decreases by a factor of 3 in the same range. This can qualitatively explain why in our spectrum (taken at 300 K) the ratio between the intensities at 2.02 eV and 1.82 eV is much larger than at 78 K. The dephasing of the pure electronic transition at 1.82 eV due to the rotation of the  $C_{60}$  molecules leads to a decrease of SHG intensity with temperature. In contrast, the 2.02 eV resonance which is assigned to a vibronic transition due to Herzberg-Teller coupling of the  $t_{1u}$  vibrational mode with the  $T_{1g}$  excitonic transition is at higher temperatures dominated by the temperature dependence of the phonons.

Qin et al. [16] determined theoretically the dispersion of the quadrupole response for single  $C_{60}$  molecules. They find resonances at 1.09 eV and 1.86 eV. The first one is only about 0.1 eV lower than the lowest peak we observe. The second one is in good agreement with our measurement. The calculated peak is of asymmetric shape but no separate feature appears near 2 eV. This indicates that the peak observed at 2.02 eV is not due to an EQ transition. Between the two calculated peaks a sharp minimum appears which seems to be due to a change of amplitude sign. The experiment shows a similarly sharp minimum at 1.57 eV. The overall agreement with the calculation is good although one may suspect that the peak calculated for 1.86 eV has a different physical origin than suggested by the assignment of the observed 1.82 eV resonance. Shuai et al. [17] calculated EQ and MD hyperpolarizabilities. While the MD hyperpolarizability tensor element which they plotted shows essentially an increase with energy the quadrupole tensor element exhibits maxima at 0.6, 1.8 and 2.4 eV. The maximum at 1.8 eV agrees with experiment.

#### 4.2.4 $C_{60}$ SHG suppression

The response of resonant SH signals to the excitation of the sample with UV pulses is shown in Fig.4.7. The signal on the 1.18 eV resonance (Fig.4.7 top) decreases rapidly and remains at a substantially reduced level for much longer than 1 ns as described in an earlier publication [22]. In contrast, the resonances at 1.82eV and 2.02eV show no comparable change of signal for the same excitation intensity (Fig.4.7 middle and bottom panel). The pump response of

the 1.35 eV peak can not be measured due to the small signal.

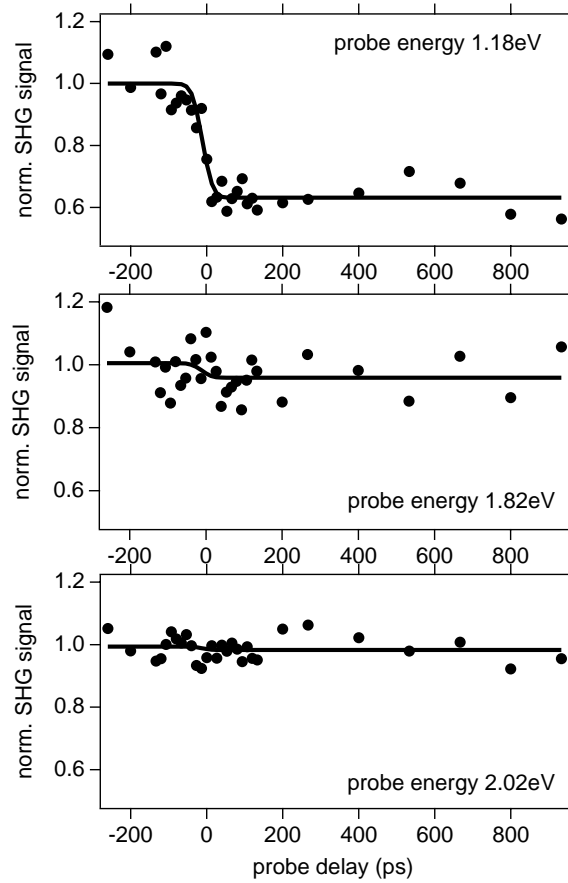


Figure 4.7: Pump-and-probe transients normalized to the signal without pump beam. The points are the data and the lines represent the best fit of a step function convoluted with the time resolution of the measurement. 3.49 eV pulses generate the excitation at  $t = 0$ . The pump density is the same in all three measurements ( $\sim 5\mu\text{J}/\text{cm}^2$ ). The probe beam which generates the SH signal is on the resonances indicated by their peak energy.

We demonstrated earlier that the SHG suppression is due to the presence of excitons at low concentration ( $<1\%$ ) [22]. As discussed in chapter 4.3, transients measured for  $\text{C}_{60}$  films separated from a Au surface by a thin spacer layer of varied thickness are in very good agreement with the assumption that



the signal suppression is due to the singlet  $T_{1g}$  exciton. For the pump intensities used in the experiments the ground state is not remarkably depleted which excludes a reason for the SH signal change corresponding to the mechanism in transient absorption spectroscopy. From Fig.4.7 we see that the SH intensity at 2.02 eV is not affected by the low exciton concentration. The effect on the 1.82 eV peak is possibly small but not statistically significant. We thus find that the strong SHG suppression does not work equally well for all resonances but appears to be specific to the 1.18 eV peak.

A likely mechanism for SHG suppression is a loss of phase coherence between the radiating states located on different molecules. A corresponding mechanism was suggested by Janner et al. to explain the decrease of SH signal from the  $C_{60}$   $T_{1g}$  exciton with increasing temperature [39]. The specific behavior of the 1.18 eV resonance could then be due to an increased sensitivity to dephasing for an excitonic transition at the doubled frequency compared to a transition at the fundamental frequency. Based on the formalism by Villeda et al. [42] we find that a strong difference between fundamental and SH dephasing exists only if the dephasing time is long compared to the pulse duration. The sharp decrease of signal at  $t = 0$  in the transient in Fig.4.7(top) demonstrates, however, that this is not the case here.

The result thus shows that there is a specifically efficient coupling between the  $H_g$  state and the lowest singlet or triplet excitons generated by the pump pulse. One may speculate that this efficient interaction is due to the CT character of the  $H_g$  state and the fact that the diffusion of the lowest excitons proceed via a virtual CT state [39].

#### 4.2.5 $C_{70}$ SHG spectroscopy

The SHG spectrum of  $C_{70}$  (Fig.4.8) is obtained in the same way as described for  $C_{60}$ . A weak resonance is observed at 1.26 eV and a steep signal rise at 1.85 eV indicates a broad resonance in which no structure is resolved.

To our knowledge no SH intensity was yet observed for  $C_{70}$ . This may be understood from the fact that (a) the broad structure at  $E > 1.83$  eV is still very weak and (b) the peak observed at  $E = 1.26$  eV does not extend to the fundamental frequency of Nd:YAG lasers (1.165 eV). The rise at 1.85 eV coincides roughly with the onset of absorption at the energy of the singlet

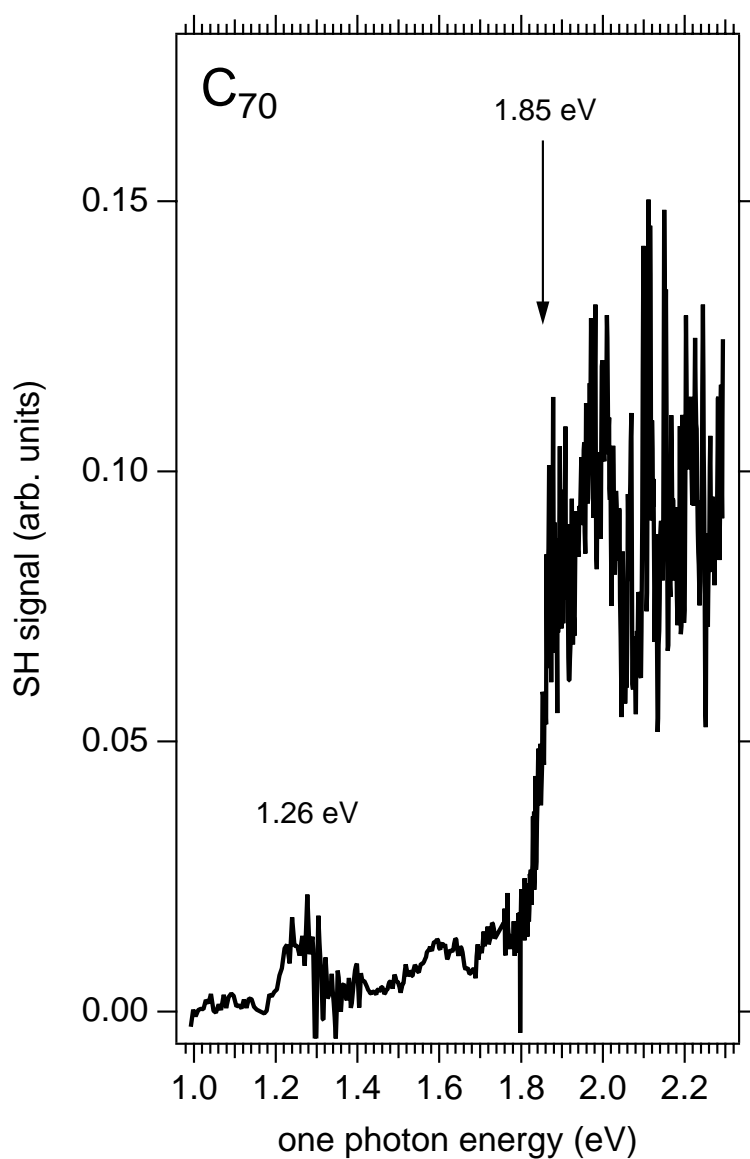


Figure 4.8:  $C_{70}$  thin film SHG spectrum. The incident beam is p-polarized.

exciton. The lowest singlet ( $S_1$ ) and triplet ( $T_1$ ) excitons were assigned for isolated molecules in Ne matrix to 1.93 eV and 1.56 eV, respectively [43]. The singlet corresponds well to the onset of SHG intensity if we assume that there

is a shift between matrix isolated  $C_{70}$  and the solid of about 0.1 eV similar as for  $C_{60}$ . The proximity of the next higher singlet exciton ( $S_2$ ) which is located 0.2 eV above  $S_1$  and higher excitonic states may lead to the broad structure above 1.85 eV. The peak at 1.26 eV, however, is too low in energy to allow an assignment to the triplet exciton. Thus, as in the case of  $C_{60}$  the spin forbidden transition is not observed. The peak coincides rather with a broad feature in absorption spectra near 2.66 eV in solution which represents according to a tight-binding calculation [44], two strong dipole allowed molecular transitions  $a_2''(\text{HOMO}) \rightarrow a_1'(\text{LUMO}+2)$  and  $e_1'(\text{HOMO}-5) \rightarrow e_1''(\text{LUMO}+1)$ . In the solid a similar feature appears at 2.41 eV [45]. Theoretical calculations of  $C_{70}$  SHG spectra were made by Shuai et al. [17]. The EQ contribution calculated for  $C_{70}$  has non-vanishing values in a sharp peak at 1.2 eV and in a broad structure between 2.0 eV and 2.4 eV which is in good agreement with the experimental  $C_{70}$  spectrum.

The lower symmetry of the  $C_{70}$  molecule with respect to  $C_{60}$  makes the low energy part of the absorption spectrum of the solid richer in ED allowed transitions. In contrast, the SHG spectrum shows only two features with low intensity. Numerous dipole allowed transitions are absent. This and the agreement with calculated spectra suggest that like in the case of  $C_{60}$  the forbidden transitions may be observed most easily. A dipole-forbidden transition was in fact predicted at 2.49 eV by Kajzar et al. [46]. It would be in even better agreement with the 1.26 eV peak than the dipole allowed transitions discussed above.

#### 4.2.6 Conclusion

We presented optical second harmonic generation (SHG) spectra of  $C_{60}$  and  $C_{70}$  between 1.0 eV and 2.3 eV fundamental photon energy. Line widths of typically 0.1 eV are observed. Transitions of lower multipole orders can be readily observed for  $C_{60}$ . For  $C_{70}$  the signals are much weaker and many ED allowed transitions are missing. For both fullerenes the lowest singlet excitons are observed while intensity due to the triplet excitons is not found. The pump beam induced suppression of the SH signal on  $C_{60}$  resonances is only efficient for the peak at the lowest fundamental photon energy. This suggests that the suppression is due to a coupling between the lowest  $H_g$  and  $T_{1g}$  excitonic states.

## 4.3 $C_{60}$ exciton quenching near metal surfaces

### 4.3.1 Introduction

Energy transfer from an excited state to an energy acceptor is of fundamental importance in physics and chemistry. The classic example is the non-radiative damping of a dipole (e.g. an electronically excited molecule) outside a metal surface [47, 48]. In a simple picture a dynamic dipole creates eddy currents within the metal which lead to the dissipation of the dipoles energy. The key result, the decrease of the non-radiative transfer rate with the cube of the metal-dipole distance, was confirmed in numerous experiments probing the decay of excited molecules separated from metallic substrates by dielectric spacers [49–53].

These experiments were, however, limited to metal-molecule distances larger than  $\sim 3$  nm. The fundamental question down to which distance classic electromagnetic theory is still valid and where it breaks down could not be addressed. Indeed, in close proximity substantial deviations from the classical picture due to the onset of tunneling are expected. In this chapter we present an experimental study of excited state decay near a metal. The distance range from 3 nm down to 1 nm is probed quantitatively. The experimental data for the  $C_{60}$ /alkanethiol/Au,Ag sandwich structures demonstrate that even at distances as small as 1 nm classic electromagnetic decay prevails.

The distance dependence of excited state life times can be measured only if a significant number of probe molecules is positioned at a well defined distance from the metal substrate. This has to be done with increasing absolute precision when the distance is reduced. Inhomogeneities and defects can substantially affect the results. Up to date multi-layers of Langmuir-Blodgett films or rare gases were employed [49–53]. They allow distance control down to about 3 nm. The rare gas layers have the disadvantage of preparational difficulty in the generation of uniform and flat layers and potential problems with interdiffusion, while the Langmuir-Blodgett technique involves building blocks which are too thick to allow a fine-tuning of distance. The ultimate length scale of distance variation is the interatomic distance ( $\sim 0.1$  nm). If spacers of rigid atomic chains are employed which are oriented perpendicular to the surface, small units can be added or removed in the chain allowing a distance adjustment with a precision of less than 0.1 nm.

We present a model sandwich system which exhibits such ideal spacer layer properties. Alkanethiol spacer layers which self-assemble from solution are known to form dense and uniform adlayers on many metal surfaces [54]. The molecules adsorb with the hydrocarbon chain nearly perpendicular to the surface and can be commercially obtained with different chain lengths. Avoiding the difficulties due to the different properties of chains with even and odd numbers of carbon atoms, the spacer thickness can easily be varied by multiples of  $-(\text{CH}_2)_2-$  groups, i.e. by multiples of 0.2 nm. We further demonstrate for our sandwich system that alkanethiols have a negligible influence on the excited state life time of the probed molecules which physisorb on the functional methyl group of the thiol.

### 4.3.2 Experimental

The probed molecule in the sandwich system is the fullerene C<sub>60</sub> which was demonstrated to exhibit a transient reduction of optical second harmonic generation (SHG) for pump densities of only a few  $\mu\text{J}/\text{cm}^2$  [55]. The life time measurement is performed as follows: A UV (3.49 eV) pump pulse of 25 ps duration excites the C<sub>60</sub> film thus defining time zero. After a variable delay the pulse is followed by an IR (1.17 eV) probe pulse (35 ps) which generates a second harmonic (2.35 eV) signal at the sample (see chapter 4.2 and Fig.4.5). C<sub>60</sub> is transparent at the probe beam wavelength. At any delay the SH signal reduction is (for sufficiently weak excitation) proportional to the density of excited states. Thus, from the SH signal as a function of the pump-probe time delay the decay rate of the excited electronic state is directly obtained. In an earlier study the excited state was determined to be a low-lying excitonic state [55]. SH thus gives us the opportunity to monitor these states without employing fluorescence or phosphorescence measurements. The lowest singlet exciton decays in approximately 1.2 ns [56] to the lowest triplet exciton which has a life time of the order of 100  $\mu\text{s}$  [57]. We find that the SH signal is reduced in faster than 30 ps and recovers with a time constant which must lie between 20 ns and 20 ms. We conclude that singlet and triplet excitons must both contribute to SH quenching.

The experimental geometry is shown in Fig.4.9. Pump and probe beams are incident at an angle of  $45^\circ$  with respect to the surface normal forming a small angle ( $\sim 8^\circ$ ) between each other. The SH photons are generated in

a narrow beam in specular reflection from the interface. The geometry and the small intensity of the pump beam exclude the detection of pump - probe difference frequency generation in the measurements.

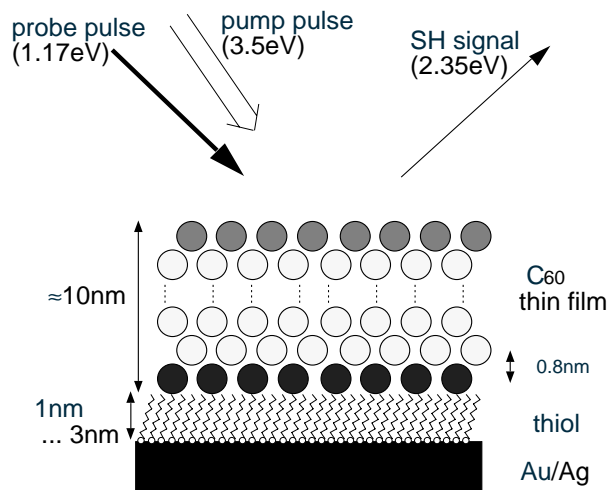


Figure 4.9: Schematic representation of the metal/alkanethiol/C<sub>60</sub> sandwich structure and the beam geometry for pump-and-SH-probe transient spectroscopy.

The preparation of well ordered thiol monolayers on Au and Ag surfaces is described in detail elsewhere [58]. Pure C<sub>60</sub> powder (99.9%) preheated in high vacuum for some 50 h is evaporated at 680 K from a Knudsen cell onto the thiol layer to obtain thin films of less than 20 nm thickness. The sample is transferred to a high vacuum ( $10^{-6}$  mbar) chamber in which the experiments are performed at room temperature.

### 4.3.3 Results and discussion

In Fig.4.10 a scanning tunneling microscopy (STM) image for a sub-monolayer C<sub>60</sub> coverage is shown. The Au substrate exhibits flat terraces on a 100 nm scale. The pits of one Au layer depth are due to the etching of the substrate during thiol self-assembly. Like the terraces, the etching pits are covered by the thiol layer [58]. The dark, parallel lines represent domain boundaries which separate highly ordered molecular domains [58]. The bright spots in the image

are the C<sub>60</sub> molecules which are mobile enough to reach preferential adsorption sites at thiol domain boundaries or in the etching pits. This strongly suggests that C<sub>60</sub> physisorbs on the thiols and does not chemically react with the methyl group. This conclusion is supported by the fact that the C<sub>60</sub> film can be completely removed by rising in chloroform [59].

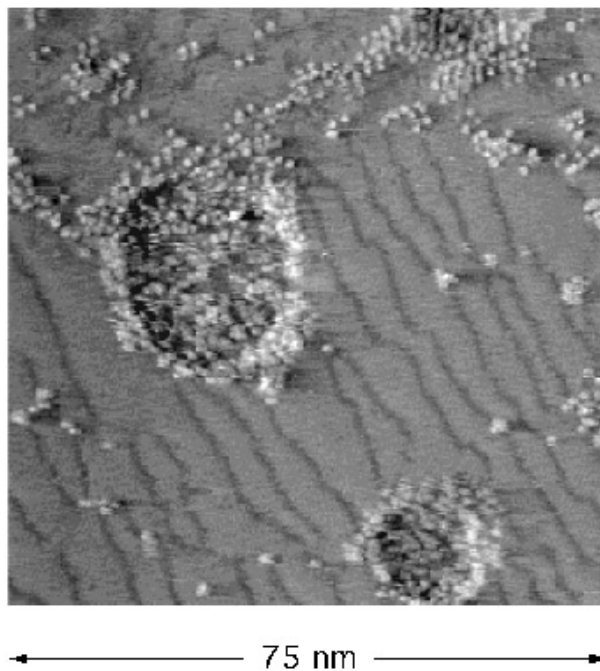


Figure 4.10: STM image of the initial stage of growth of C<sub>60</sub> on decanethiol covered Au(111).

Fig.4.11 shows pump-and-SH-probe transients of C<sub>60</sub>/alkanethiol/Au(111) sandwiches for different alkane chain lengths  $n$  adsorbed on Au. The measurements for Ag exhibit equivalent features. The transients exhibit two contributions, one with a long life time ( $\tau \gg 1$  ns) and a second with a reduced life time. Similar to the earlier interpretation of C<sub>60</sub> thin films on quartz [55], we ascribe the long lived state to the surface of the C<sub>60</sub> film and the short lived state to its interface with the substrate. Because of the optical properties of Au a significant part of the second harmonic signal at 2.35 eV is due to the Au substrate which results essentially in a signal offset.  $\chi_0^{(2)}$  is the second order polarizability of the sandwich system at the probe frequency when no

excitation is present. We can describe the normalized transient signal by the following formula:

$$\frac{S(t)}{S_0} = \left( \left\{ 1 - \theta(\tilde{t}) \left[ \frac{\Delta\chi_{\text{long}}^{(2)}}{\chi_0^{(2)}} + \frac{\Delta\chi_{\text{short}}^{(2)}}{\chi_0^{(2)}} \cdot \exp\left(-\frac{\tilde{t}}{\tau}\right) \right] \right\} \circ R(\tilde{t} - t) \right)^2 \quad (4.1)$$

Here,  $\theta$  is the Heaviside function [ $\theta(t) = 1$  for  $t > 0$  and  $\theta(t) = 0$  for  $t < 0$ ] and  $R$  is a Gaussian representing the time resolution function of the experiment. The formula is based on the following model: At  $t = 0$  the pump beam excites a long lived and a short lived state which both reduce the second order non-linear susceptibility  $\chi_0^{(2)}$  related to the sample without excitation.  $\chi^{(2)}$  is assumed to return to its original value  $\chi_0^{(2)}$  by a single exponential decay for the short lived state plus a decaying long lived state, here approximated by a constant. This amplitude function is convoluted with the experimental time resolution  $R$  and then squared to obtain the normalized SH intensity.

Fig.4.12 shows the decay rate  $1/\tau$  as a function of the spacer layer thickness obtained by fitting the data with Eq.4.1. The results for the Au and Ag substrates are marked by circles and triangles, respectively. The spacer thickness  $d$  for thiols adsorbed on Ag is obtained from the formula  $d = 5.6\text{\AA} + (1.3\text{\AA})n$  [54], where  $n$  is the length of the carbon chain. In the determination of the thickness on Au it was taken into account that the thiol molecules are not adsorbed perpendicularly as on Ag but tilted by  $25^\circ$ . The thiol layer itself has a negligible effect on the observed decay: The coupling between the exciton and the methyl groups of the thiol to which the  $C_{60}$  molecule is physisorbed will not change with the thiol chain length. As we do not observe that the decay rate tends towards a constant value for the thickest spacer layers the transfer rate from the exciton to the thiol must be much smaller than the smallest measured decay rate. From the single exponential decay specifically of the measurements for  $n = 5$  and  $n = 7$  we conclude that the observed short lived state results from only one  $C_{60}$  layer at the interface. Else we should observe, because of the large  $C_{60}$  layer distance of 0.8 nm (see Fig.4.9), a series of exponentials with distinct time constants, each resulting from a different  $C_{60}$  layer. The sensitivity to the immediate interface is a prerequisite for a precise evaluation of the dependence of the rate constant on  $C_{60}$ -metal distance.

The data in Fig.4.12 were fitted in two ways. First, a power-law fit



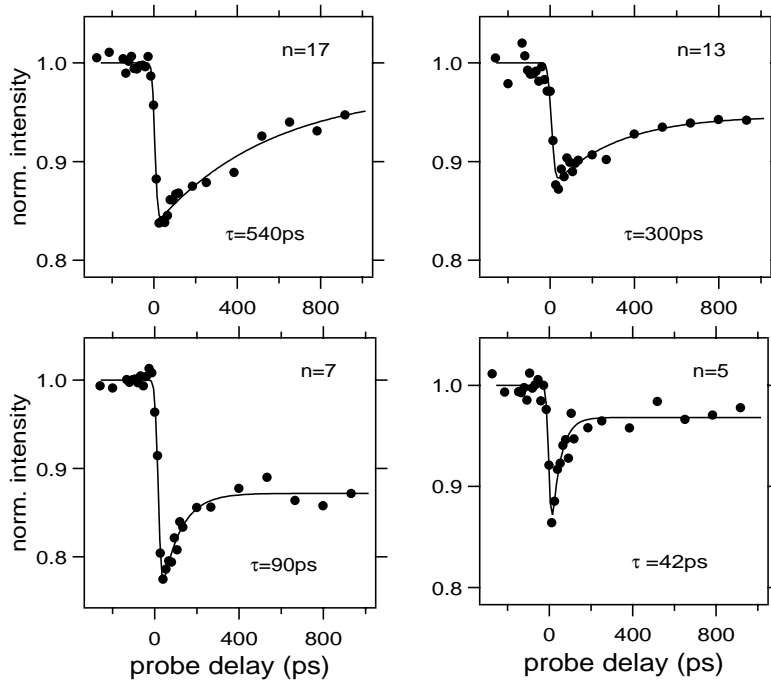


Figure 4.11: Pump-and-SHG-probe transients for sandwich structures with Au substrates and different thiol  $\text{HS}(\text{CH}_2)_n\text{CH}_3$  chain lengths  $n$ . The points represent the data and the dotted lines are fits according to Eq.4.1. For each measurement the life time  $\tau$  of the short lived component is indicated.

$$\tau_{\text{eff}}^{-1} = \alpha d^{-m} \quad (4.2)$$

allows one to determine the multipole order of the coupling and the dimensionality of the acceptor system by means of the positive integer  $m$ ;  $\alpha$  is a proportionality constant which will not be analyzed. An electric dipole to bulk transfer, e.g., is characterized by  $m = 3$ , a magnetic dipole to bulk transfer by  $m = 1$  and an electric dipole to surface transfer will have  $m = 4$  [48, 60]. Best fits for the Au and Ag surfaces according to Eq.4.2 are shown as dashed lines in Fig.4.12. The best fit exponents are  $m = 2.9(+0.7/-0.5)$  for Au and  $m = 3.9(+0.6/-0.9)$  for Ag. The results already indicate that the transfer is dominated by electromagnetic decay. No evidence for tunneling contributions are observed. In the case of Ag the transfer to the surface is more important

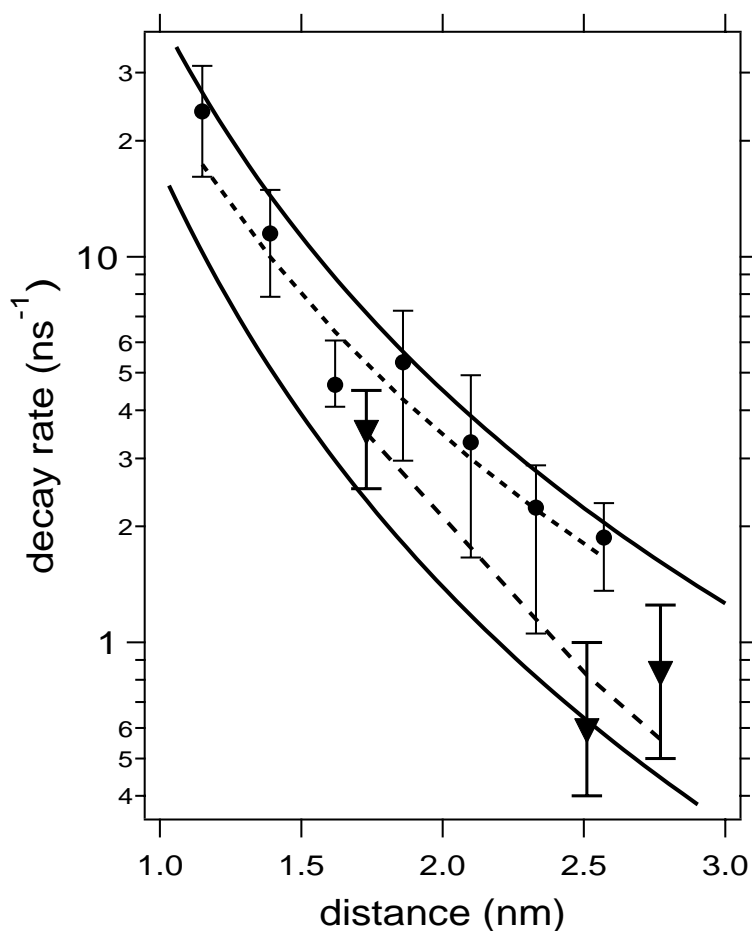


Figure 4.12: Decay rate  $1/\tau$  as a function of thiol layer thickness. The circles and triangles represent the measurements for Au and Ag substrates, respectively. The dotted lines are algebraic fits according to Eq.4.2 while the solid lines are obtained according to Eq.4.3 (see text). The upper lines refer to measurements of samples with Au substrates and the lower lines refer to Ag samples.

while Au exhibits transfer to electrons in the bulk.

The second fit (solid lines in Fig.4.12) allows a quantitative analysis based on the analytic expression for the decay rate developed by Persson and Lang

[61]:

$$\tau_{\text{eff}}^{-1}(d) = \tau_{\infty}^{-1} \left( 1 + \frac{1}{d^3} \frac{1}{2k^3} \text{Im} \left\{ \frac{\varepsilon_m(\omega) - \varepsilon_1}{\varepsilon_m(\omega) + \varepsilon_1} \right\} + \frac{1}{d^4} \frac{1}{4k^3} \xi(r_s) \frac{\omega}{\omega_F k_F} \right) \quad (4.3)$$

which includes in the bracket three terms, corresponding to the free radiation decay, the electric dipole transfer to the bulk metal and to the metal surface. The approximation inherent in the last term is valid for both Au and Ag as  $d \gg \omega_F/(\omega k_F) = 0.25$  nm. In Eq. 4.3  $k$  and  $\omega$  are the wave vector and the frequency, respectively, of the electromagnetic field generated by the excited state. We can assume that the exciton decay occurs in the C<sub>60</sub> fluorescence region at  $\hbar\omega = 1.7$  eV.  $\omega_F$  and  $k_F$  are the Fermi frequency and the Fermi wave vector of the metal, respectively, which were taken from [62].  $\xi(r_s)$  is a function discussed in [61] with  $\xi(r_s) = 1.2$  for Au and Ag ( $r_s = 3$ );  $r_s$  is the free electron radius.  $\varepsilon_1$  is the permittivity of the thiol layer ( $\varepsilon_1 = 2.1$ ) [54] and  $\varepsilon_m(\omega)$  is the (complex) permittivity of the metal at the dipole radiation frequency. The term in brackets is thus completely determined by literature values.

The second term in the bracket is due to the bulk absorption and dominates the decay rate for Au substrates even at 1 nm because of the onset of strong interband transitions in the visible. This is in agreement with the observed  $d^{-3}$  behavior in this case (Fig.4.11). For Ag the second term is much smaller and the surface term begins to dominate at about 2 nm separation which is reflected in a transition to a  $d^{-4}$  behavior. The only unknown parameter in Eq.4.3 is the C<sub>60</sub> exciton free radiation life time  $\tau_{\infty}$ . By assuming  $\tau_{\infty} = 1.0 \pm 0.5$   $\mu$ s we obtain an agreement with the Au and the Ag data (solid lines in Fig.4.12). In the case of the Au samples the good agreement demonstrates that the distance dependence is well described by the theoretical model. The data for the Ag substrates appear to be less conclusive. The Ag samples were more difficult to prepare in good quality so that only data for three different thiol lengths could be obtained. These data are, however, consistent with the model both in the absolute rate constant and in the exponent determined by the power-law fit according to Eq.4.2. The difference between the Au and the Ag rate constants is slightly smaller than predicted by theory.

As we already discussed, the candidates for the monitored excitonic state are the lowest singlet and triplet states.  $\tau_{\infty}$ , however, must be greater than

the effective life time of an observed state. The small value obtained for  $\tau_\infty$  suggests that in this experiment the singlet exciton is observed rather than the triplet exciton. The comparison of  $\tau_\infty$  with the effective life time of the singlet state of approximately 1.2 ns suggests a fluorescence quantum efficiency of  $1.2 \times 10^{-3}$  ( $+1.2 \times 10^{-3} / -0.5 \times 10^{-3}$ ) which in fact agrees with the experimental value of  $0.7 \times 10^{-3}$  [63].

It is known from the literature that the singlet exciton is of  $T_{1g}$  symmetry and its decay to the  $C_{60}$  ground state of  $A_g$  symmetry is dipole-forbidden and takes place via a magnetic dipole transition. This transition multipole, however, would result in a  $d^{-1}$  dependence of the decay rate in the case of Au and a  $d^{-2}$  dependence at short distances in the case of Ag. The exponents obtained in our study do thus explicitly show that the forbidden transition acquires electric dipole character by intensity borrowing from dipole allowed modes via Herzberg-Teller coupling. This result is also important for the interpretation of resonant second harmonic generation at  $C_{60}$  interfaces: By this mechanism forbidden transitions can become electric dipole allowed. Dipole allowed transitions, however, can not efficiently generate SH radiation in centrosymmetric bulk structures. We thus obtain for such transitions in  $C_{60}$  the interesting result that resonant SHG becomes allowed at the interface while it remains forbidden in the bulk. The surface and interface sensitivity of SHG spectroscopy can thus be restored even for forbidden transitions which is remarkable because  $C_{60}$  was shown to exhibit substantial SHG bulk contributions [19].

In conclusion, we have shown that thiol spacer layers allow a controlled fine tuning (0.2 nm) of separations in sandwich structures at short distances ( $d = 1 - 3$  nm). The spacer layer does not contribute to the life time reduction due to the weak coupling (physisorption). We have further demonstrated that at short distances  $> 1$  nm the quenching of a  $C_{60}$  exciton at a Au surface is still dominated by a  $d^{-3}$  dependence which can be ascribed to efficient volume damping due to accessible inter-band transitions. The result is described by the Persson-Lang model containing only one adjustable parameter which reproduces correctly the known fluorescence efficiency. For a limited number of Ag substrates we find longer life times than for Au samples and a distance dependence which indicates the predominance of surface damping. The distance dependence for both substrates directly confirms that the forbidden exciton decay obtains electric dipole character due to vibronic coupling.

## 4.4 Fast transport of excitons in C<sub>60</sub>

### 4.4.1 Introduction

Electronic states within the band gap play an important role for transport properties of semiconductors. The diffusion of excitations in the band gap is of special interest for spatial energy transport following photoexcitation. This especially if the decay of strongly absorbing states above the gap is fast and finishes by populating excitonic states. These may diffuse for extended times until they become trapped on the lattice and decay. These excitonic states of C<sub>60</sub> have been studied extensively by a variety of techniques like optical linear [34,36,64,65] and non-linear spectroscopy [18,28,29,39] as well as electron energy loss spectroscopy (EELS) [30] and other techniques [24,30,66] but not many experimental results are available on their diffusion properties [39]. Theoretical studies, however, provide a basis for the understanding of the diffusion process of isolated excitons at low temperature [40]. One expects that the propagation at low energies is slow in a molecular crystal like C<sub>60</sub> in which the electronic coupling between molecules is weak. In this chapter we present an energy resolved study of spatial diffusion of excitons in C<sub>60</sub> thin films at room temperature. The photoexcitation is tuned over a wide range around the band gap between 1.8 eV and 2.6 eV. We use the transient grating technique well suited to study exciton diffusion directly [67,68] and employ second harmonic generation (SHG) to monitor the grating decay. Above 1.86 eV we find a surprisingly high diffusion constant of 100 cm<sup>2</sup>/s which we assign to the lowest singlet exciton. The diffusion is several orders of magnitude faster than expected from theoretical studies. We suggest that the strongly increased diffusion rate is due to the presence of charged excitations created by the excitation pulse and thermal phonons.

At temperatures above 260 K the C<sub>60</sub> crystal forms an fcc lattice with a lattice constant of 1.42 nm [69]. In molecular crystals excitons are obtained from molecular electronic states transformed to bands by the intermolecular coupling in the solid. The C<sub>60</sub> excitons with the lowest energies are Frenkel excitons situated at 1.55 eV (triplet) and 1.82 eV (singlet). The lowest molecular states are only weakly disturbed by the intermolecular coupling in the solid. The solid state shift from the states of isolated molecules is small (about 100 meV). In a solid state picture the dissociation of an electron and a holes situ-

ated on the same molecule requires about 0.4 eV [14, 70]. The propagation is by hopping and was proposed to proceed via a transitory charge transfer (CT) state [39, 40].

We have shown in the previous chapters (4.2 and 4.3) that SHG can be employed to monitor  $C_{60}$  excitation below the band gap with ps time resolution and without the need to detect luminescence. In SHG a coherent signal is detected allowing to study diffusion in thin films by grating techniques. The presence of photogenerated excitation leads to a substantial reduction of the resonant SH signal generated at 2.33 eV from a 1.17 eV incident light pulse. In SHG pump-and-probe transients the SHG signal forms a step function: After photoexcitation the SHG signal decreases within the experimental time resolution (35 ps) and stays constant for much longer than 1 ns for photoexcitation energies between 3.5 eV and 1.7 eV. We can thus exclude that the excited states leading to SHG quenching are charge carriers as their properties change drastically over this energy range. The properties of SHG quenching demonstrate that the lowest excitons play the essential role in the quenching [55]. Using the suppression of the SHG signal as a means to monitor the density of excitons we carried out a grating experiment to measure the diffusion constant. A pump beam at 3.5eV photon energy generated the grating [12]. We observed the appearance and an immediate ( $< 10$  ps) decay of an excitation grating of 8 mm fringe spacing. This result is surprising because a diffusion constant with a lower limit of  $800 \text{ cm}^2/\text{s}$  (or a ballistic propagation velocity of  $> 400 \text{ km/s}$ ) is required, which are very large values for excitons in a molecular crystal at room temperature. As the energy of the photoexcitation in this experiment is, however, far above the energy of the low lying excitons in  $C_{60}$  we present here a study which was extended to energies below the band gap.

#### 4.4.2 Experimental

The  $C_{60}$  thin film samples were prepared as described in chapter 4.2. As  $C_{60}$  films are subjected to photopolymerisation all exposure to ambient light was avoided. It was verified that the absorption of the employed laser beams is weak enough to allow measurements over several hours without detectable polymerization [12].

The excitation grating on the sample is generated by interference of two

pulses derived from the same tunable source (OPG/OPA). As in the previous experiments, a third pulse at 1.17 eV probes the excitation at the sample and can be time-delayed with respect to the other two with a motorized delay line (Fig.4.13). The SH photons (2.33 eV) generated in reflection from the film are detected by a photo multiplier mounted on a double monochromator. The excitation fringe spacing is similar in all measurements. The pump energy densities were 10 – 100  $\mu\text{J}/\text{cm}^2$ ; depending on photon energy lower densities were used at pump wavelengths of high C<sub>60</sub> absorption. The probe density is adjusted to be at least a factor of two below the damage threshold.

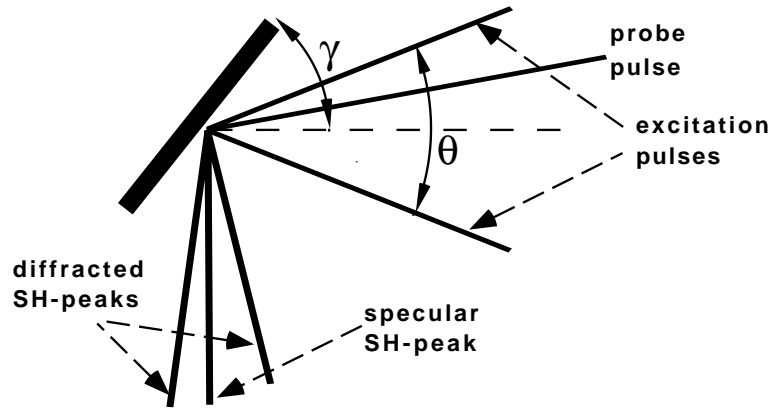


Figure 4.13: Scheme of the beams for the grating experiment

### 4.4.3 Results

The optical excitation by a pump beam in the visible and near UV leads to the creation of excitations which cause a decrease in the effective second order nonlinear susceptibility  $\chi^{(2)}$  responsible for the SHG signal  $S_0$  according to  $S_0(2\omega) \propto (\chi^{(2)} \cdot E(\omega)E(\omega))^2$ . The excitation grating with the fringe spacing  $L$  gives rise to a periodic spatial modulation of  $\chi^{(2)}$  and generates angular side peaks in the SH radiation. Fig.4.14a shows an angular scan in which

the sample is rotated. From the position of these two diffraction peaks the excitation fringe spacing  $L$  can be determined.

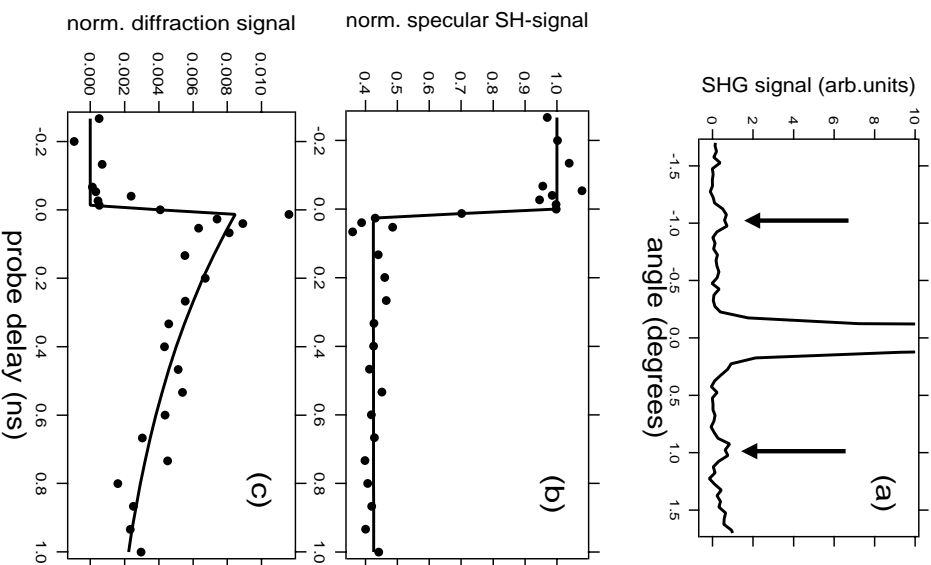


Figure 4.14: Grating experiment with a pump photon energy of 2.5 eV: a) Angular scan in which the sample is rotated by  $\phi$ . Probe delay: 20 ps. The strong SH intensity is due to specular scattering and the two side peaks (arrows) arise from diffraction by the grating. b) Transient of the specular SH beam. c) Transient of a diffracted peak.

The intensity in the first order side peaks provides a direct measure of the amplitude of spatial modulation of  $\chi^{(2)}$ . As the pump grating in the experiment is generated by beams with large band width it exhibits a rather low



contrast. It is thus important to use medium excitation densities in order to maximize the modulation amplitude of  $\chi^{(2)}$  and to obtain sufficiently intense diffraction from the grating. By probing at various time delays between pump and probe pulses the decay of the excitation grating is measured. Fig.4.14c shows an example of a transient in first order diffraction. It exhibits a steep rise when the grating is generated followed by an exponential decay. In contrast, the specularly generated SH intensity (Fig.4.14b) shows the usual SHG suppression behavior described above. We conclude that the spatial modulation decays while the average excitation density remains constant. We remark for clarity that the intensity in the side peaks is generated only for coincident (i.e. interfering) pump beams.

We assume that the interaction between the low lying excitations and the SHG resonance at 1.17 eV which leads to signal quenching is a local effect and the decay of the grating represents a true diffusion of excitation. The decay can then be modeled in the usual way starting with an initial sinusoidal density modulation on a uniform background. We further assume that the diffusion constant  $D$  does not strongly depend on the concentration of excited species which is in the experiments of the order of 0.1% of the molecular density. For these concentrations the nonlinear susceptibility  $\chi^{(2)}$  decreases in a good approximation linearly with excitation density [55]. The SH-intensity is proportional to the square of  $\chi^{(2)}$  and we obtain an exponential decrease with the signal decay time [71]:

$$\tau = \frac{\Lambda^2}{8\pi^2 D} \quad (4.4)$$

In order to determine  $\tau$  the transient measurements are fitted by the decay function convoluted with the time resolution function of the experiment.

In Fig.4.15 the measured SH-transients (dots) in first order diffraction for different excitation wavelength and the corresponding fits (lines) are presented. In the wavelength range covered by the data the decay time  $\tau$  changes by more than two orders of magnitude. While for the excitation at 3.5 eV in Fig.4.15a the decay time  $\tau$  is below the experimental time resolution as already discussed in the introduction, the decay times  $\tau$  in Fig.4.15b and c are on a time scale accessible to measurement. The fits to angular scans and transients provide the parameters  $L$  and  $\tau$  from which the diffusion constant  $D$  is calculated

using Eq.4.4. The result is represented in Fig.4.16. The extremely fast decay (Fig.4.15a) is omitted in that figure because we can only give a lower limit of the diffusion constant and the decay is most probably due to charge diffusion and not to exciton diffusion, as will be discussed below.

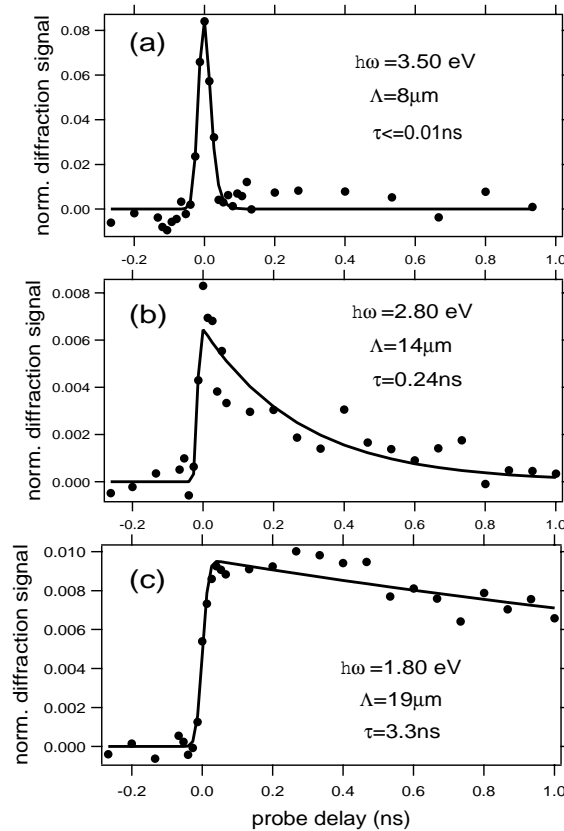


Figure 4.15: Transients of the SH intensity in the first order diffraction peak for different photon energies of the grating. Dots are measured points while lines represent fits with the function discussed in the text. Grating photon energy  $\hbar\omega$ , fringe spacing  $L$ , and decay time  $\tau$  obtained from the fit are given on each panel. The signal is normalized to the specular signal without pump beam.

#### 4.4.4 Discussion

The diffusion constant above 1.86 eV is found to be 100 cm<sup>2</sup>/s and independent of photon energy. A steep decrease is observed below 1.86 eV. This onset is a clear signature of a state situated at this energy. It can be identified with the lowest singlet T<sub>1g</sub> exciton (see chapter 4.2). If the pump photon energy is insufficient to excite this state ( $\hbar\omega < 1.86$  eV) a strongly reduced diffusion of about 10 cm<sup>2</sup>/s is observed. Possible excitations at these energies are the lowest triplet exciton and trapped singlet excitons. We emphasize that the decrease of diffusion constant is not due to a reduced excitation as can be seen from the amplitudes of the normalized traces in Fig.4.15 b and c for which the spatial modulation of non-linear response is similar. We thus find that even at excitation energies far below the band gap the diffusion remains fast.

As the ratio between film thickness and grating parameter is much smaller than one the diffusing excitation will encounter the interfaces a large number of times before the grating disappears. We see that the interfaces scatter the excitation but do not destroy it. A trapping at point defect sites which would result in a freezing of the excitation grating and thus of the diffracted SH signal is clearly not observed at excitation energies above 1.86 eV. The diffracted signal decreases to zero which means that the grating completely disappears on a 1 ns time-scale. However, we cannot exclude that some freezing occurs below 1.86 eV. A fit in which a non-zero probability for trapping is assumed would yield a larger diffusion constant at 1.8 eV.

From the bandwidth of the T<sub>1g</sub> exciton of about 100 meV obtained in SHG spectroscopy of thin films at room temperature [28] we estimate a lower limit for the time between exciton scattering events of 0.02 ps. In order to obtain the measured diffusion constant of 100cm<sup>2</sup>/s we then have to assume a mean free path of 40 nm (i.e. about 40 C<sub>60</sub> nearest neighbor distances). The resulting group velocity for exciton propagation is about two orders of magnitude above the maximum slope obtained in the exciton dispersion relation [40] calculated for the singlet T<sub>1g</sub> exciton in the low temperature phase. In the high temperature phase the average orientation of neighboring molecules is more favorable to hopping and its frequency is expected to increase [39] approximately by a factor of three [24]. This correction is too small to explain the experimental value.

This discussion shows that the pure exciton diffusion can not explain the ob-

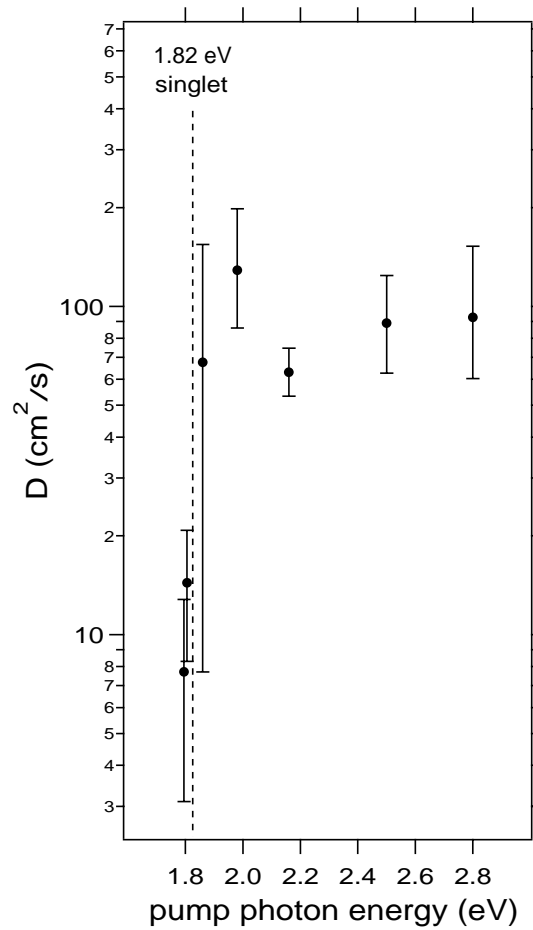


Figure 4.16: Measured exciton diffusion constant as a function of photon energy of the beams generating the excitation grating.

served diffusion constant. Other excitations may, however, facilitate diffusion. We will discuss two possibilities: phonons and charge carriers. Phonons may promote exciton transport by a phonon wind mechanism [72] which is due to temperature gradients created by the absorbed pump beam. This mechanism can, however, be excluded for two reasons: First, the total energy deposited by the pump beam is small and the local temperature rise does not exceed 1 K which is small compared to the sample temperature. Second, the results show that the exciton velocity exceeds sound velocity by more than an order

of magnitude even when perfectly coherent propagation (ballistic transport) is assumed. In contrast to this mechanism a homogeneous distribution of lattice vibrations is in general responsible for the reduction of the exciton coherent propagation length and accounts for the reduction of diffusion constants with increasing temperature. However, intramolecular vibrations and crystal lattice phonons can also facilitate diffusion as they represent a heat bath. The associated molecular and lattice deformations could increase the average propagation rate of the excitons.

Charge carriers even at low concentrations can substantially modify the properties of a solid. Their presence may increase exciton diffusion for example through an increased screening in the solid or by a direct coupling to the excitonic states. Free electron-hole pairs can be generated above the band gap (2.3 eV). However, in  $C_{60}$  the onset of photoconductivity is observed already at the onset of optical absorption [73, 74], a fact which has been explained by the formation of a hole polaron state and a mobile electron [14]. The polaron state at 0.8eV has been shown to become substantially populated above the band gap at 2.3eV [32] but charge carriers of reduced mobility can already be generated below the band gap. While free charge carrier were reported to exhibit initial time constants of picoseconds the photoconductivity below the band gap decays in oxygen-free samples with initial decay times of 0.7 ns (at 2.0 eV) [75]. These long lived photocarriers generated at  $t = 0$  together with the excitons will thus be present on the time scale where diffusion is measured in our experiment. The experimental result shows that crossing the threshold of free electron-hole creation does not affect the exciton transport.

The mechanisms suggested above do not explain the very fast decay after excitation at 3.5 eV (Fig.4.15a). In this spectral region free electrons and holes are formed efficiently and they might promote exciton diffusion much more than charge carriers formed below or just above the band gap. However, at these high excitation energies low energy excitons are not created directly but by recombination of free electrons and holes. The fast destruction of the grating ( $< 10$  ps) in Fig.4.15a may thus be determined by charge diffusion before excitons are created.

In conclusion, diffusion constants of  $C_{60}$  excitations for optical pump energies above and below the band gap were determined by grating experiments. We find that low energy excitations propagate efficiently in  $C_{60}$ . Above 1.86 eV excitation energy singlet excitons are generated and the measured diffusion

constant of  $100 \text{ cm}^2/\text{s}$  is proposed to result from singlet diffusion. The constant is much larger than estimated from theoretical studies for low temperatures. Below 1.86 eV excitation energy the diffusion constant drops steeply. We propose that the presence of phonons or charged excitations promotes the diffusion.

There is however one point which makes the data less conclusive: The diffusion constants  $D$ , presented in Fig.4.16, are determined according to equation 4.4 from measurements where the excitation fringe spacing  $\Lambda$  has been kept constant for a specific excitation energy. This has been done since the SH suppression in the specular peak is constant over at least 1 ns (see Fig.4.14b) and thus we concluded that the excitonic lifetime  $\tau_{\text{lifetime}}$  can be assumed infinite on this timescale. In order to take account of finite lifetimes of the excitons, equation 4.4 has to be replaced by [67]:  $\frac{1}{\tau} = \frac{8\pi^2}{\Lambda^2}D + \frac{2}{\tau_{\text{lifetime}}}$ . From measurements of the signal decay time  $\tau$  with different fringe spacings  $\Lambda$ , the diffusion constant  $D$  as well as the excitonic lifetime  $\tau_{\text{lifetime}}$  could then be extracted by plotting  $\frac{1}{\tau}$  against  $\frac{8\pi^2}{\Lambda^2}$ . According to Fig.4.13 this requires varying the angle  $\theta$  between the two excitation beams over a large range which was however, not possible due to the geometrical restrictions imposed by the vacuum chamber in which the sample is mounted (chapter 4.2.2).

## Chapter 5

# Thiolates - vibrational SF spectroscopy

In the last years self-assembled monolayers (SAMs) have attracted a lot of interest. A SAM is formed by molecules composed of three parts (see Fig.5.1). Firstly an anchor group (head group) which can bind the molecule to a solid surface; secondly the middle part which is the backbone and influences the orientation of the molecules and the mechanical stability of the monolayer; finally, the terminal group (tail group) which determines the chemical properties of the monolayer. In an ideal case the SAMs are well ordered and densely packed. As head groups mercapto (thiol, -SH), carboxyl (-COOH), trichlorosilyl (-SiCl<sub>3</sub>), trialkoxysilyl (-Si(OR)<sub>3</sub>), or phosphonic acid (-P(OH)<sub>3</sub>) groups are used. Substrates can be metal (Au, Ag, Pt,Cu, ...) and semiconductor surfaces. A very extensively investigated class of SAMs are *organothiulates bound to metal surfaces* due to their stability and high quality. In this part of this work we will regard some organothiolate SAMs in more detail.

A nice example for an application of alkanethiolate SAMs is presented in chapter 4.3 where the SAMs adsorbed on gold or silver served as a spacer layer in order to control the distance of C<sub>60</sub> molecules in front of a metal surface from 3 nm down to 1 nm in steps of 0.2 nm by choosing the appropriate chain length - a distance range not easily accessible with other techniques.

But the main interest for these monolayers comes from the fact that by modifying the functional chemical tail group in the SAMs, surface properties

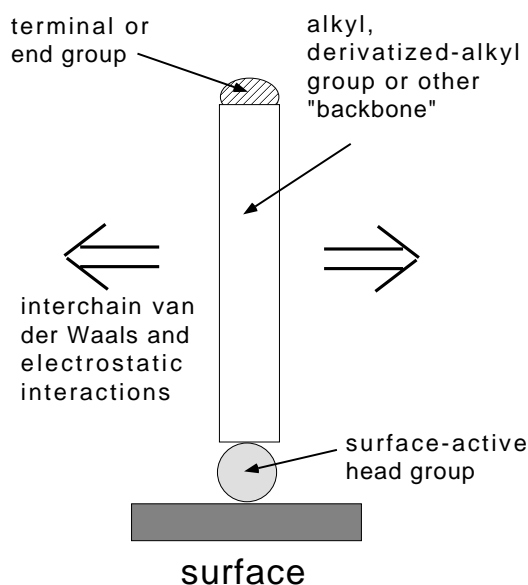


Figure 5.1: Schematic view of a self-assembling molecule

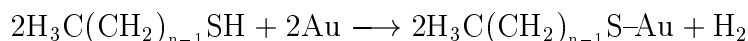
can be chosen (which is also known as *tailoring surface properties*). A field where end group-modified SAMs play an important role is the development of biosensors, where the biomolecules are linked to the functional tail groups of the SAMs [76]. A further potential application is the two dimensional nanostructuring of surfaces. It has been shown that cobalt islands can be grown on end group-modified alkanethiolates if they are activated with palladium [77]. Also non-modified alkanethiolate SAMs (i.e. choosing the hydrophobic methyl group as functional group) have properties which are interesting for technical applications. Thus it has been shown that alkanethiolate SAMs protect copper and gold surfaces from corrosion [78], [79]. Furthermore alkanethiolate SAMs can be used as surfactants. Cavalleri et al. have demonstrated that copper which normally grows on Au(111) in a three dimensional mode can be grown in a pseudo layer-by-layer mode when the gold surface is covered with alkanethiolate [80]. However, in this case the SAMs are not classical surfactants which are normally added in excess to metal plating baths; but they are present as a single layer only. Like classical surfactants they are adsorbed on the gold surface prior to the copper deposition and remain on the gold surface or on the deposited copper layers. The given examples of the application of SAMs are



by no means exclusive, they only serve to demonstrate the enormous potential which SAMs have. Yet in general the behavior of the SAMs is rather complex. For their properties not only the functional terminal group is responsible but also their conformation [81]. This is why a better understanding of the geometrical structure of the SAMs in the different applications is desirable for achieving the goal of tailoring surface properties.

## 5.1 Properties of alkanethiols on gold

Alkanethiols have the formula  $\text{H}_3\text{C}(\text{CH}_2)_{n-1}\text{SH}$ , which we abbreviate as “ $\text{C}_n$  thiol”. When the  $\text{C}_n$  thiol adsorbs from the solution or from the gas phase at a Au(111) surface, a strong S – Au bond is formed and the Au(111) reconstruction, which exists on the bare, freshly prepared surface, is lifted. The reaction is:



The binding energy of the thiolate  $\text{H}_3\text{C}(\text{CH}_2)_{n-1}\text{S-Au}$  is about 126 kJ/mol, nearly independent of  $n$  [82]. The behavior of the adsorbate is rather complex, which is why we first turn to the properties of the thiolates with long alkyl chains ( $n > 14$ ).

Experimental findings demonstrate that the sulfur arranges in a  $(\sqrt{3} \times \sqrt{3})\text{R}30^\circ$  superstructure and that the chains are in the all-trans conformation (see figure 5.2). The C-S-Au angle is believed to be close to the tetrahedral angle,  $110^\circ$ . Theoretical studies however, suggest the possibility of the presence of  $110^\circ$  and/or  $180^\circ$  angles [83, 84]. The sulphur atoms seem to be located not only in the three-fold hollow sites of the Au(111) surface [85–87] as was earlier proposed [83, 88].

The S–S distance is too large to allow a stable packing of *vertical* methylene chains on gold and thus, interacting via van-der-Waals forces, the chains take a position tilted away from the surface normal (angle  $\alpha$ , see Fig.5.2) by about  $30^\circ$ , thus reducing the distance between the chains in order to minimize their free energy [89–94]. The chain-chain distance is now close to the alkane bulk values [90, 95], and the structure is reminiscent of that of the bulk alkanes [95, 96]. The tilt  $\alpha$  is directed towards the next-nearest-neighbor (NNN) sulfur atom, i.e. in the  $[1\bar{1}0]$  direction of the densely packed Au rows (angle  $\phi$ ); this

direction varies slightly with  $n$  [90]. The twist angle  $\beta$  determined from IR spectra is about  $50^\circ$  [91–94]; experimental [91] and theoretical evidence [84,97] as well as the alkane bulk structure suggest an alternative model where a chain and its neighbor show values about  $+45^\circ$  and  $-45^\circ$ , respectively.

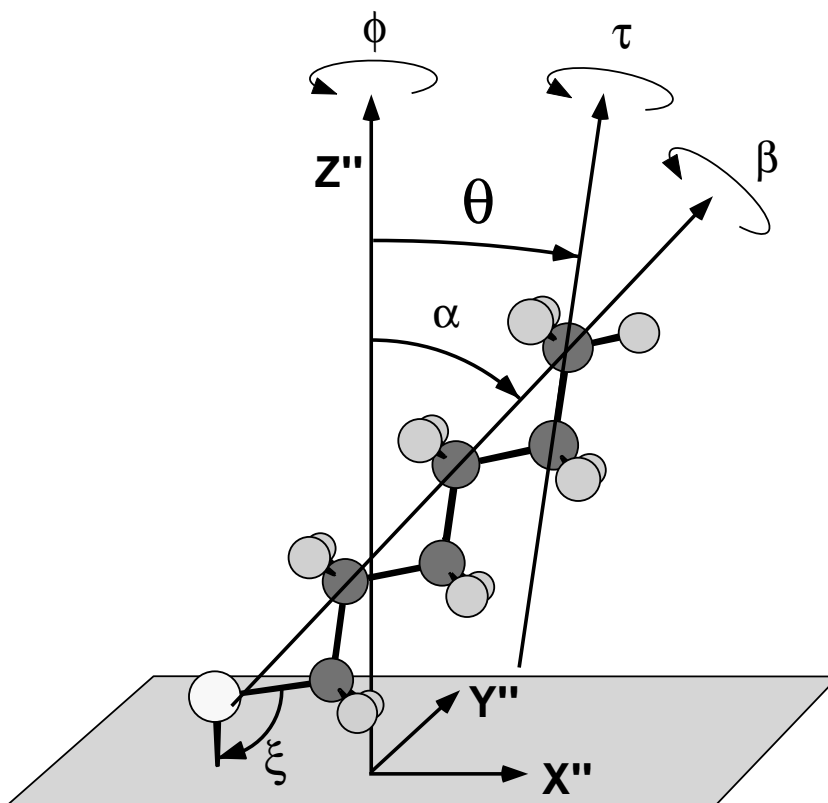


Figure 5.2: Scheme of a Hexanethiolate  $n=6$  adsorbed on a gold surface. In the figure the twist angle of the C – C – C plane  $\beta$  and the twist angle  $\tau$  of the methyl end group are  $0^\circ$ . The molecule is in all-trans conformation.

Short chains ( $n < 12$ ) exhibit a rich polymorphism with sulfur in the usual  $(\sqrt{3} \times \sqrt{3})R30^\circ$  phase or in a  $(p \times \sqrt{3})$  ( $p=7$  up to 13) *striped phase* [98–104]. The former lattice results in the already discussed orientation, while in the striped phases the sulfur arranges in lines parallel to the  $[11\bar{2}]$  direction. The molecular orientation in the striped phases is still under discussion. It is thought that at least a fraction of the molecules is parallel to the surface

(tilt  $\alpha = 90^\circ$ ). This means that a molecule has only two neighboring chains and that the coverage is well below 30% respective to the coverage of the  $(\sqrt{3} \times \sqrt{3})R30^\circ$  pattern. Poirier postulates in some cases *interdigitation* of chains which means that a certain fraction of the flat-lying molecules is no more in all-trans conformation but exhibits gauche defects<sup>1</sup> [98] and a distorted methylene chain is placed above a neighboring flat-lying chain (see figure 5.3). In the striped structures the chain is oriented perpendicular to the sulfur stripes and thus parallel to the  $[1\bar{1}0]$  direction.

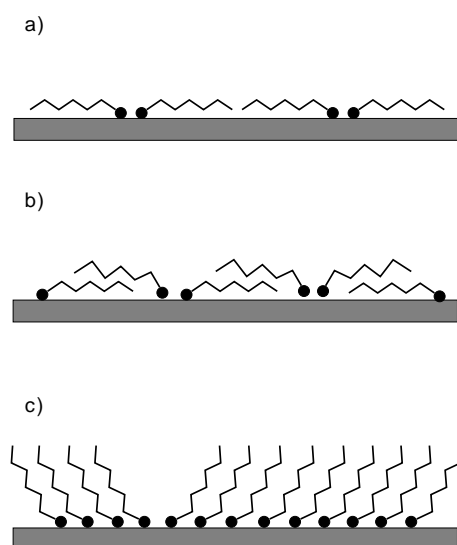


Figure 5.3: a) flat lying chains b) interdigitation c) two densely packed, well ordered domains (model)

Chains with  $n=12,13,14$  can be expected to show intermediate behavior, i.e. only in some cases they adopt striped structures and form mainly the  $(\sqrt{3} \times \sqrt{3})R30^\circ$  packing [105]. As with short chains, the structure should depend on the preparation conditions.

Altogether the ordering of the films is the result of a subtle interplay of the different interactions (sulfur-substrate, sulfur-sulfur, chain-chain) and explains the different behavior of long and short chain thiolate SAMs as well as the differences when other substrates are used. On silver for example the C-S-Ag

<sup>1</sup>rotation of  $120^\circ$  about a C-C bond

bond angle for methylthiolate is  $180^\circ$  [106]. The tilt angle  $\alpha$  of the chains on silver and on copper is about  $12^\circ$  [79, 107, 108]. On platinum the monolayer is less ordered [93, 109].

## 5.2 Alkanethiolate SAMs on gold in air

### 5.2.1 Signatures in vibrational spectroscopy

The C-H stretching vibration range of alkanethiolate SAMs on gold has been extensively investigated by IR spectroscopy [92, 110–113]<sup>2</sup>. At least 6 resonances are found. The symmetric  $d^+$  and asymmetric  $d^-$  vibrations pertain to the methylene group. There also are the asymmetric stretches in plane  $r_{ip}^-$  and out of plane  $r_{op}^-$  pertaining to the methyl group as well as the symmetric methyl stretch which is split up by Fermi resonance into two components  $r_a^+FR$  and  $r_b^+FR$ . Fermi resonance splitting is due to the mixing of the C – H stretching mode with an overtone of a C – H bending mode which has the same symmetry and nearly the same energy. If the overtone and the stretching vibration have exactly the same energy, the intensity of the observed two resonances is equal.

Table 5.1 lists the vibrations with their frequency and the direction of the transition dipole moment in molecular coordinates. In polycrystalline samples of long alkyl chains additional features are clearly visible in the spectra [114]. They come from the fact that the vibrational energy of the methylene groups can shift due to a different chemical environment, i.e. neighboring sulfur or methyl groups at both ends of the alkyl chain. The corresponding additional vibrations are labeled with an  $\alpha$ . Additionally, Fermi resonance splitting of the  $d^+$  vibration has been observed [114]. These vibrations are reported in the second part of table 5.1. All these vibrations are infrared active. Whether they can also be seen in SF spectra depends on the transition matrix elements of the Raman polarizability (see chapter 5.3) and on the conformation of the molecules in the film (see chapter 5.2.3). The investigation of the C – H stretching vibration range reveals differences in excitation energy between IR and Raman energies of up to several  $10\text{ cm}^{-1}$  for methylene vibrations [115, 116]. This is due to the fact that the methylene groups in the chain interact

---

<sup>2</sup>and references therein

Desig.	in $\text{cm}^{-1}$	Orientation of transition dipole moment
$d^+$	2851	in C-C-C plane, in H-C-H plane
$r_a^+$ FR	2878	$\parallel$ to C - CH <sub>3</sub> bond
$d^-$	2918	$\perp$ to C-C-C plane
$r_b^+$ FR	2937	$\parallel$ to C - CH <sub>3</sub> bond
$r_{op}^-$	2957	$\perp$ to C-C-C plane
$r_{ip}^-$	2964	in C-C-C plane, $\perp$ to C - CH <sub>3</sub> bond
$d^+(\alpha)$	2853	in C-C-C plane, in H-C-H plane
$d^+$ FR	2894	in C-C-C plane, in H-C-H plane
$d^-(\alpha)$	2925	$\perp$ to C-C-C plane

Table 5.1: IR resonances of alkanethiols in the C - H stretching vibration range.

with each other and thus their motion is no more isolated but coupled with the other methylene groups. This is why new normal modes arise. The different selection rules for IR and Raman spectroscopy lead to the excitation of different normal modes. For example, when probing the  $d^-$  resonance of an alkyl chain in all-trans conformation with Raman spectroscopy, the methylene groups are excited in a mode where neighboring groups oscillate in phase ( $d^-(0)$ ) whereas, when excited with IR radiation, they oscillate in anti phase ( $d^-(\pi)$ ). The difference in excitation energy of these modes is  $40 \text{ cm}^{-1}$ . [115, 116].

## 5.2.2 Experimental

### Sample preparation

For the preparation of the samples different substrates were used. For the SFG measurements either Au(111) gold crystals or gold films on mica were used. For the films 120 nm gold (99,99% purity) was evaporated onto cleaved preheated mica sheets. The evaporations were carried out at a base pressure of  $2 \times 10^{-6}$  mbar at substrate temperatures of 550-560 K. The films were annealed during three hours at 620 K (see also [117]). Before use the gold films were flame annealed to dark red glow and cooled in air before immersing them into the thiol solution (see below).

The Au(111) crystal was cleaned in a nochromix/H<sub>2</sub>SO<sub>4</sub> conc. (Thomas Sci-

entific, USA) oxidizing solution and rinsed with MilliQ water (resistivity 18.2 M $\Omega$ cm, Millipore Intertech, USA). Then it was placed onto a clean Ceran plate (Schott) and annealed during 5 to 10 minutes by placing a Bunsen burner under the Ceran plate which is heated to red glow. The crystal was cooled in air under a little glass jar, protecting it from dust particles. Then it was immediately immersed in the thiol solution.

For the IRRAS measurements macroscopically flat surfaces are necessary. Thus we used glass disks of 17 mm diameter onto which 120 nm gold was deposited by means of argon ion sputtering, directly before immersing them into the thiol solution. The chamber had a base pressure lower than  $6 \times 10^{-6}$  mbar (argon pressure during deposition  $5 \times 10^{-2}$  mbar).

Octadecanethiol ( $\text{CH}_3(\text{CH}_2)_{17}\text{SH}$ ,  $\text{C}_{18}$ ), dodecanethiol ( $\text{CH}_3(\text{CH}_2)_{11}\text{SH}$ ,  $\text{C}_{12}$ ), and hexanethiol ( $\text{CH}_3(\text{CH}_2)_5\text{SH}$ ,  $\text{C}_6$ ) (Fluka) were used as received to prepare 100  $\mu\text{M}$  solutions in absolute ethanol. All the glassware was cleaned in nochromix/ $\text{H}_2\text{SO}_4$  conc. solution and rinsed with MilliQ water.

For the self-assembly the gold samples were kept in the solutions at 40°C for at least 24 hours ( $\text{C}_{18}$ ) and 12 hours ( $\text{C}_{12}, \text{C}_6$ ), respectively. After emersion they were thoroughly rinsed with ethanol, dried in air and then mounted for the experiments.

It should be noted that long chain alkanethiol monolayers are stable in air for several days. For example the IRRAS spectra of  $\text{C}_{12}$ ,  $\text{C}_{16}$  and  $\text{C}_{18}$  remain unchanged up to 20 days [118].

### Optical setup

The SFG measurements were performed as follows (see figure 5.4). The sample was mounted horizontally (parallel to the table). As visible beam we used the rest of the 532 nm radiation, which is left from the frequency tripling of the fundamental beam. After tripling, its shape is rather irregular. The energy distribution is smoothed out by cutting off the margins and letting the beam travel over a distance of 8 m. The beam energy can be selected by the pinhole diameter. Typical pulse energies are 0.5 mJ at a beam diameter of 3 mm ( $35 \mu\text{J}/\text{cm}^2$ ). The beam impinges unfocused onto the sample. Another pinhole, placed about 20 cm before the sample, limits the size of the spot to a diameter of about 1 mm. The beam passes through a polarizer and then its polarization is adjusted by rotating a  $\lambda/2$  wave plate to be  $p$ -polarized

at the sample. A narrow band pass filter makes sure that no other frequency components are in the beam. The polarization of the infrared beam is linear as defined by the generation process and it impinges  $p$ -polarized onto the sample surface. Its energy is about  $100 \mu\text{J}$  at  $3000 \text{ cm}^{-1}$  and it is slightly focused with a  $\text{CaF}_2$  lens to a spot of a diameter of about 1 mm on the sample surface. The infrared and the visible beam have a common plane of incidence.

The emitted SFG signal first passes through a short pass filter (505FD64-50SX, LOT/ORIEL) and then through a holographic-notch filter (HNF-532-1.5, LOT/ORIEL) before being focused on the entrance slit of a double monochromator. In order to prevent stray light from the OPG/OPA unit, which is always exactly at the same wavelength as the SFG signal, this unit is enclosed in a light-proof box. At the exit slit of the double monochromator a photomultiplier tube is fixed. The photomultiplier pulses are measured with a gated charge integrator (Camac, LeCroy ADC 2249 SG). Normalization techniques are described in chapter 3.3.

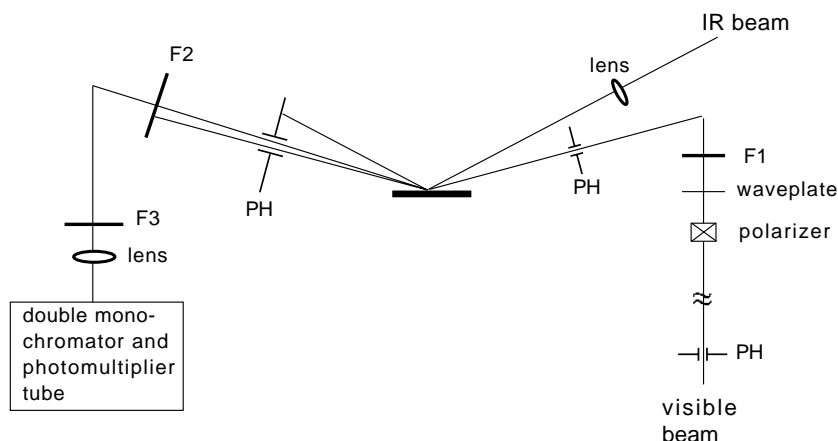


Figure 5.4: Setup for the SFG measurements in air: PH pinhole, F1 band pass filter 532 nm, F2 short pass filter, F3 holographic notch-filter (suppresses 532 nm radiation), see also text.

Nearly all SF-measurements are performed in co-propagating geometry, i.e. the visible and the infrared beam impinge from the same side onto the sample (see figure 5.4 and 5.5a). The visible and the infrared beam have an angle of about  $62^\circ$  and  $58^\circ$  to the surface normal, respectively. Additionally we

measured a C<sub>18</sub> SAM also in a counter-propagating geometry as well as with co-propagating DFG (see figure 5.5b and c). The filter combinations are the same for SFG co- and counter-propagation whereas for DFG the short pass filter is replaced by a long pass filter (OG570, Schott).

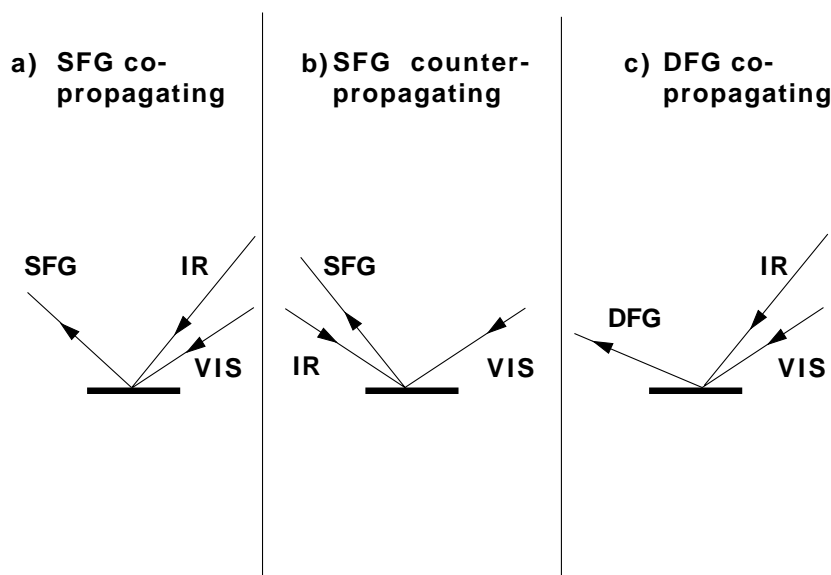


Figure 5.5: Beam geometries for SFG co- and counter-propagation as well as for the DFG measurements.

In the experiment the incidence angles of the visible and infrared beam are fixed. However, tuning the frequency of the infrared beam from  $2800\text{ cm}^{-1}$  to  $3000\text{ cm}^{-1}$  changes the angle of the radiated SFG or DFG beam according to equation 2.19. Assuming incidence angles of  $58^\circ$  (IR) and  $62^\circ$  (vis) in co-propagation geometry gives an angular variation for the radiated beam of  $0.07^\circ$  for SFG and  $0.03^\circ$  for DFG. For the SFG measurement in the counterpropagation geometry ( $-58^\circ$  instead of  $+58^\circ$  for the IR incidence angle) the variation is  $1.04^\circ$  and thus 15 and 35 times larger than in the other cases. The sample detector distance is about 1.5 m, and with a diameter of the notch-filter of about 2.5 cm the maximal acceptance angle is  $0.95^\circ$ . Taking into account that the beam diameter is of the order of 1 cm, it is clear that parts of the beam are cut off during frequency tuning and do not reach the detector. This would cause a significant slope in the recorded spectra. This is



why in counter-propagation geometry the sample is mounted on a rotational stage and rotated about the  $y$ -axis ( $\perp$  to the plane of incidence) during the measurement in order to compensate for the angle variation and for keeping the SF beam in the same direction.

### IRRAS measurements

For the IRRAS measurements presented in this chapter a Mattson 6020 Galaxy series FT-IR spectrometer with a liquid nitrogen cooled MCT (mercury cadmium telluride) detector was used. The sample compartment is in air, the angle of incidence was chosen to about  $75^\circ$  with respect to the surface normal and the measurements were averaged over 400 scans. The background spectrum was recorded with an identical gold sample which was immersed in absolute ethanol instead of the thiol solution.

### 5.2.3 Results $C_{18}$ thiolate in air

#### Resonances in SFG/DFG compared to IRRAS

In figure 5.6, SFG measurements in co- and counterpropagation and a DFG measurement - all in *ppp*-polarization - are presented.

As expected from the literature [89, 109, 119] the spectra show three strong resonances. They are at  $2878\text{ cm}^{-1}$ ,  $2938\text{ cm}^{-1}$ , and  $2968\text{ cm}^{-1}$  and can be attributed to the methyl stretching vibrations  $r_a^+$ FR,  $r_b^+$ FR, and  $r^-$ , respectively. The nearly degenerated in-plane and out-of-plane asymmetric stretching vibrations  $r^-$  cannot be separated. No resonances belonging to methylene stretches can be observed indicating a well ordered monolayer with the molecules nearly exclusively in the all-trans conformation. Since in the all-trans conformation the methylene groups are distributed symmetrically along the chain, their contributions nearly cancel each other because of inversion symmetry [120]. A significant number of gauche defects would lead to the apparition of methylene bands [119]. It should be remarked here that some types of conformational defects, such as kinks<sup>3</sup>, retain an inversion center and are thus not visible in

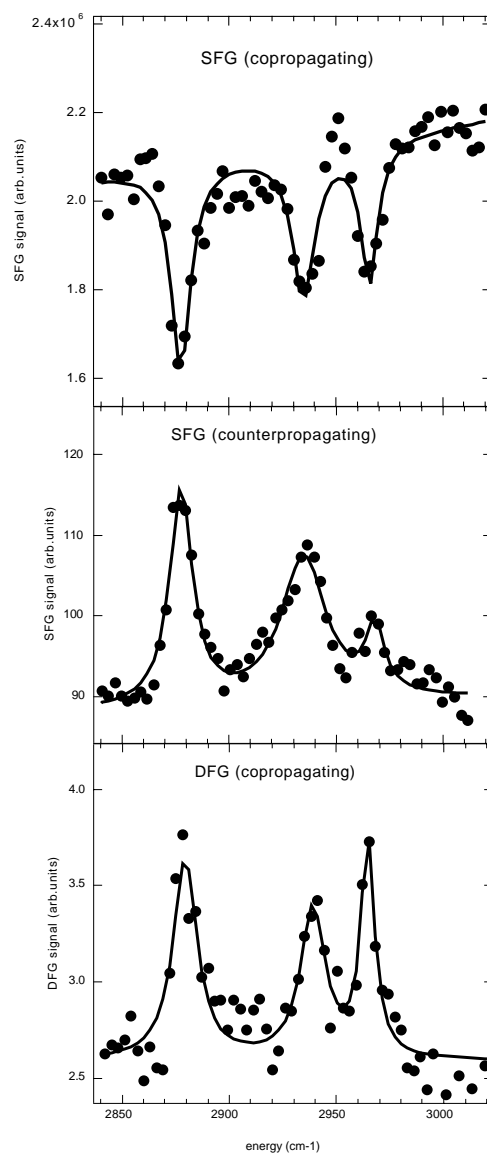
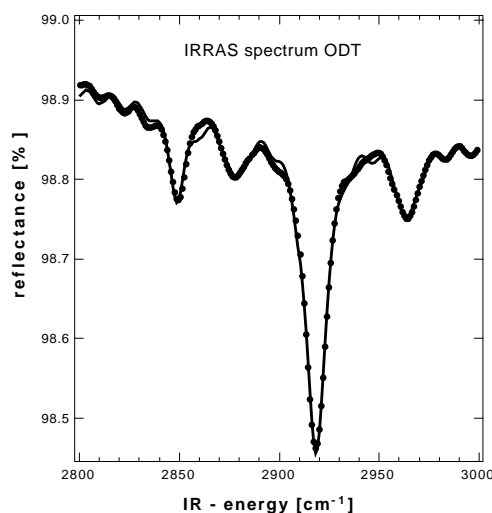


Figure 5.6: Spectra of  $C_{18}$ . The SFG spectrum a) is recorded in copropagation geometry and is normalized to the intensity of the IR beam. In the spectra b) (SFG) and c) (DFG) the values directly read from the A/D card give the signal in arbitrary units. The points represent the data and the solid lines are fits with lorentzian shapes. The phase between the resonant and the nonresonant contributions was fixed to 0 or  $\pi$  (see also text).

Figure 5.7: IRRAS-spectrum of C<sub>18</sub>, see text

SF spectra [121].

Figure 5.7 presents a typical IRRAS spectrum of C<sub>18</sub>. The resonances at 2850 cm<sup>-1</sup> and 2918 cm<sup>-1</sup> originate from the symmetric d<sup>+</sup> and asymmetric d<sup>-</sup> stretching vibrations of the methylene groups. They are much more intense than the peaks of the methyl group at 2877 cm<sup>-1</sup>, 2935 cm<sup>-1</sup>, and 2966 cm<sup>-1</sup> due to the large number of methylene groups with respect to the number of methyl groups per molecule (ratio 17:1).

### Comparison between SFG co- and counter-propagating

The SFG spectra show a large nonresonant background on which the resonant features are situated. The resonant contribution is due to the molecules and the nonresonant contribution comes only from the gold substrate; the nonresonant susceptibility of the molecule is negligible compared to that of gold [10]<sup>4</sup>. The SF signal  $I$  is proportional to

$$I \propto |Ae^{i\varphi} + B|^2 = |A|^2 + |B|^2 + 2|A||B|\cos\varphi \quad (5.1)$$

<sup>3</sup>two gauche defects of opposite rotation directions with an unchanged bond in between (also called g<sup>+</sup>tg<sup>-</sup>sequences)

<sup>4</sup>and references therein

where  $A$  is the nonresonant substrate contribution and  $B$  is the resonant contribution of the adsorbate (also see Eq.5.6).  $\varphi$  is the phase between the two contributions. The phase is near 0 or  $\pi$ , otherwise the resonances would have an asymmetric line shape.

In the SFG counter- and co-propagating measurements the resonances appear as peaks and as dips, respectively. This comes from the phase difference between the nonresonant background signal and the resonant signal which depends on the beam geometry and can be explained by means of the Fresnel factors  $F_{ijk}$  which are different in the two geometries. We find the phase difference by considering the signs of the resonant and the nonresonant contributions:

As explained in chapter 2.6 the radiated SF field has the following general form:

$$E_p^{out}(\omega_{SF}) = E_p^{in}(\omega_{vis})E_p^{in}(\omega_{IR}) \times \left\{ \chi_{xxz}^{(2)} F_{xxz} + \chi_{xzx}^{(2)} F_{xzx} + \chi_{zzz}^{(2)} F_{zzz} + \chi_{zxx}^{(2)} F_{zxx} \right\} \quad (5.2)$$

with  $F_{ijk} = L_i K_j^{vis} K_k^{IR}$ . Since the dominant Fresnel factors for the SAM are  $F_{xxz}$  and  $F_{zzz}$  (see chapter 2.6) the field radiated from the SAM is

$$E_p^{SAM}(\omega_{SF}) = \left\{ \chi_{xxz}^{(2)} F_{xxz} + \chi_{zzz}^{(2)} F_{zzz} \right\} \cdot E_p^{in}(\omega_{vis})E_p^{in}(\omega_{IR}) \quad (5.3)$$

When regarding the nonresonant contribution from the gold one has to use the Fresnel factors for the substrate. For this the term  $\left(\frac{n_2}{n_1}\right)^2$  in the expressions for  $L_z$  and  $K_z$  (Eq. 2.26) has to be replaced by unity. Now the dominant factors are no more  $F_{xxz}$  and  $F_{zzz}$ , but  $F_{xzx}$  and  $F_{zxx}$ . Thus the field radiated by the gold substrate can be written as

$$E_p^{gold}(\omega_{SF}) = \left\{ \chi_{xzx}^{(2)} F_{xzx} + \chi_{zxx}^{(2)} F_{zxx} \right\} \cdot E_p^{in}(\omega_{vis})E_p^{in}(\omega_{IR}) \quad (5.4)$$

By passing from co- to counter-propagation the  $x$ -component of the IR-field changes sign and  $K_x^{IR}$  has to be replaced by its negative. It follows that all the factors  $F_{ijx}$  change sign too. This does not affect the field radiated from the SAM (Eq.5.3), however the field from the substrate (Eq.5.4) changes the sign (phase change of  $\pi$ ) which leads to the inversion of the resonant features (see also [109]).

### Comparison between SFG and DFG

When regarding the spectra b) and c) in figure 5.6 one can see that the non-resonant background in DFG is substantially smaller than in SFG. The large “nonresonant” background of SFG on gold comes from an interband transition of which the threshold lies at about 506 nm ( $= 19763 \text{ cm}^{-1}$  SFG) [122]<sup>5</sup>. The DFG frequency lies below this interband transition and thus the nonresonant background is much lower. In the measured spectral range the signal from gold is essentially independent of frequency.

A consequence of this is that the absolute height of the resonant feature in the DFG case is about 20 times smaller than in the SFG case. This can be explained by considering the expression for the intensity (Eq. 5.1). In the SFG case the amplitude of the nonresonant background  $A$  is about 10 times larger than the amplitude of the resonance  $B$ . Squaring of the expression essentially gives the nonresonant part  $|A|^2$  and the interference part  $2|A||B|\cos\varphi$  which scales with the nonresonant amplitude. This interference term is 20 times larger than the purely resonant term. In contrast, in the DFG measurement the nonresonant substrate background is nearly negligible and thus the resonant feature originates solely from the purely resonant term  $|B|^2$  and is not “amplified” through the interference term.

The small amplitude of the DFG resonant feature itself is no disadvantage as long as it is not obscured by background contributions [122]. However in our case the background comes mainly from the fluorescence of the gold substrate, which is induced by the visible beam and has - even though filtered - the same order of magnitude as the resonant feature. DFG has been used very successfully in a case where the magnitude of the resonant - non-resonant ratio was equal to 10 and 1, for the DFG and SFG signals, respectively [122].

---

<sup>5</sup>and references therein

### 5.3 Orientation analysis of methyl groups

The experimental determination of the orientation of molecules is an important application of optical vibrational spectroscopies as infrared absorption spectroscopy (IRRAS) [123] Raman spectroscopy [124], and sum frequency spectroscopy. In sum frequency spectroscopy, information on the orientation can be obtained from measuring in different polarization combinations (*sps* and *ssp*) independent  $\chi^{(2)}$  tensor elements of *one* vibrational mode [120, 125–128]. In these analysis apart from the scattering geometry also Raman tensor element ratios have to be known from independent measurements.

But on metal surfaces, as already remarked in chapter 2.6, only the *ppp*-polarization leads to efficient SF generation. These spectra provide a pronounced sensitivity to molecular orientation (see Chapter 5.5). Since our experiments do not allow a quantitative analysis of other polarization combinations due to the low SF yield, an analysis along the line of earlier studies is not possible.

However, even though organic molecules adsorbed on gold surfaces have been largely investigated by SFG [89, 109, 119], no method which allows orientation analysis of methyl ( $-\text{CH}_3$ ) groups solely from the *ppp*-spectrum, has been presented yet. In such an analysis  $\chi^{(2)}$  tensor elements of *different* vibrational modes are involved. Since these tensor elements are not well known for the methyl vibrations we construct them in a simple bond superposition model. From this bond model we calculate the SFG intensity ratio of the symmetric and the asymmetric stretching vibrations as a function of the orientation of the methyl group.

#### 5.3.1 Basis of the model

The contribution of the molecules to the SF spectra stems from their nonlinear susceptibility  $\beta^{(2)}$ . The nonlinear susceptibility  $\chi^{(2)}$  of the medium is proportional to the number  $N$  of the molecules:

$$\chi_{ijk}^{(2)} = N\beta_{ijk}^{(2)} \quad (5.5)$$

The molecular nonlinear susceptibility  $\beta^{(2)}$  is generally expressed in a coordinate system adapted to the symmetry of the molecule. For a vibration the

resonant part of the  $\beta^{(2)}$  tensor can be written as [89]

$$\beta_{ijk}^{(2)} = \frac{M_{ij}A_k}{\omega_{IR} - \omega_{vib} + i\Gamma} \quad (5.6)$$

where  $\vec{A}$  is the IR dynamic dipole moment and  $M$  is the Raman dynamic polarizability tensor. In the approximation of linear superposition we have  $\vec{A} = \sum_l \frac{\partial \vec{\mu}}{\partial q_l} \cdot u_l$  and  $M = \sum_l \frac{\partial \alpha}{\partial q_l} \cdot u_l$  with  $\vec{\mu}$  and  $\alpha$  the IR dipole moment and the polarizability tensor, respectively.  $q_l$  are the normal coordinates of the vibration with the respective amplitudes  $u_l$ .  $M_{ij}$  and  $A_k$  are the projections of  $M$  and  $A$  on the axis of the coordinate system defined for the molecule.

Numerical values may be obtained from the literature but are often available only for a few of the vibrational modes of interest. An analysis may then be based on calculated Raman tensors as e.g. in the case of adsorbed  $\text{NH}_3$  [129]. As similar data are, however, not available for the C – H stretching modes, we attempt a strongly simplified approach, in which IR dynamic dipole moment and Raman tensor are constructed from the properties of the single C – H bonds.

From IR intensity analysis performed in the 1970ies it is known that such an approach gives only rough estimates for IR absorption strengths [130] to which corrections have to be added. The essential problems of a linear combination of bond properties are the knowledge of the bond lengths changes in the normal modes and the polarization changes in one bond due to the variation of the length of another. This coupling appears to be somewhat less critical for polarizabilities in the modeling of Raman intensities than for IR intensities [131]. However, detailed studies comparable to the case of quantitative absorption studies are rare.

### 5.3.2 Construction of the tensor elements

The first step is the analysis of the relative intensities of the symmetric and antisymmetric  $\text{CH}_3$  vibration in a functional group of an adsorbed alkanethiol for which the geometry is fairly well known from the literature. We make the simplifying assumption that the differential (or dynamic) dipole moment  $\vec{A}$  and the differential polarizability tensor  $M$  of a C – H bond stretching vibration is represented by the change of the IR dipole moment  $\vec{\mu}$  and the

polarizability tensor  $\alpha$  with the change of the bond length  $q$ , respectively. Setting proportionality constants to 1, the values of  $A_{bond}$  and the diagonal Raman differential polarizability tensor  $M$  are

$$\vec{A}_{bond} = \frac{d\vec{\mu}}{dq} = \begin{pmatrix} 0 \\ 0 \\ 1 \end{pmatrix}; M_{bond} = \frac{d\alpha}{dq} = \begin{pmatrix} \delta & 0 & 0 \\ 0 & \delta & 0 \\ 0 & 0 & 1 \end{pmatrix}; \quad (5.7)$$

in the natural C–H bond coordinates with rotational symmetry about the C–H bond direction ( $z$ -axis, see Fig.5.8). These bond tensors are transformed

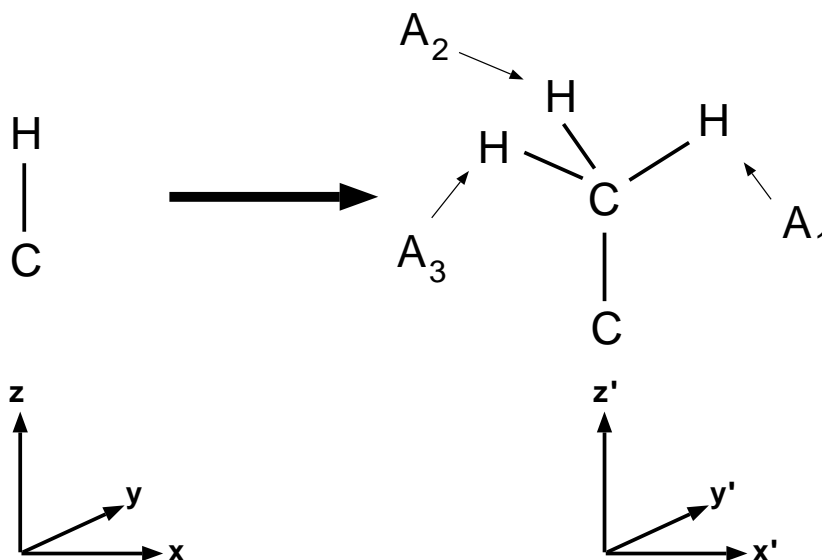


Figure 5.8: Definition of the coordinate systems for the methyl group.

to molecular or group coordinates by rotation. Defining the new  $z'$ -direction along the three-fold axis of the  $\text{CH}_3$  group, we obtain for example for the three C–H bonds

$$\vec{A}_1 = D_{y'}(71^\circ) \circ \vec{A}_{bond} \quad (5.8)$$

$$\vec{A}_2 = D_{z'}(120^\circ) \circ D_{y'}(71^\circ) \circ \vec{A}_{bond} \quad (5.9)$$

$$\vec{A}_3 = D_{z'}(-120^\circ) \circ D_{y'}(71^\circ) \circ \vec{A}_{bond} \quad (5.10)$$



where  $D_i(\gamma)$  is the rotation around axis  $i$  by the angle  $\gamma$ .  $71^\circ$  is the complementary angle to the tetrahedral angle ( $\sim 109^\circ$ ). The Raman tensors are transformed equivalently, but like second rank tensors and their representations (in  $x', y', z'$ ) are called  $M_1, M_2$ , and  $M_3$ .

Next, the tensors for a vibrational mode are constructed: Assuming that the motion of the C atom in the alkane chain is negligible, the  $\text{CH}_3$  vibrational eigenmodes become simple. The eigenvectors with respect to the three bond lengths  $u_i$  (normal modes) are the symmetric stretch as well as the in-plane and out-of-plane antisymmetric stretching modes:

$$\vec{u}_{sym} = \frac{1}{\sqrt{3}} \begin{pmatrix} 1 \\ 1 \\ 1 \end{pmatrix}; \vec{u}_{asym,ip} = \frac{1}{\sqrt{6}} \begin{pmatrix} 2 \\ -1 \\ -1 \end{pmatrix}; \vec{u}_{asym,op} = \frac{1}{\sqrt{2}} \begin{pmatrix} 0 \\ 1 \\ -1 \end{pmatrix} \quad (5.11)$$

The tensors for a vibrational mode  $\nu$  are obtained by multiplying the dynamic polarization  $\vec{A}_i$  and the dynamic polarizability tensors  $M_i$  (both in  $x', y', z'$ ) by the amplitude  $u_i$  of the bond length vibration for a given normal vibration and summing over all bonds (weighted sum).

$$\vec{A}_\nu = \sum_i u_{i,\nu} \cdot \vec{A}_i \quad M_\nu = \sum_i u_{i,\nu} \cdot M_i \quad (5.12)$$

In principle, in this way, the tensors for any vibration can be constructed. However, it is known from IR spectra that this approximation is not very accurate, thus we can only expect results which are qualitatively correct. For the symmetric mode we obtain:

$$\vec{A}_{sym} = \begin{pmatrix} 0 \\ 0 \\ 0.59 \end{pmatrix} \quad (5.13)$$

$$M_{sym} = \begin{pmatrix} 0.77 + 0.97 \cdot \delta & 0 & 0 \\ 0 & 0.77 + 0.97 \cdot \delta & 0 \\ 0 & 0 & 0.20 + 1.53 \cdot \delta \end{pmatrix} \quad (5.14)$$

As can be expected from symmetry arguments, the dynamic dipole is parallel to the  $z'$ -axis in the  $\text{CH}_3$  group coordinate frame, and the Raman tensor is diagonal. Next we determine the value of  $\delta$ : Assuming  $\delta = 0$  we obtain a

ratio of 4.2 between the components  $M_{x'x'}$  and  $M_{z'z'}$ . From this we calculate a Raman depolarization ratio (ratio of total scattered light for *differently* polarized incident light) of  $\rho_n = 0.12$  in good agreement with the values for  $\text{CH}_3$  groups attached to long chains [132]. In the literature of orientation analysis of the methyl group the symmetric stretching mode of methanol with an experimental value of  $\rho_s = 0.014$  [133] (ratio between polarizations of scattered light for *unpolarized* incident light) has been employed [125]. We believe that the reference to this small molecule with a neighboring hydroxyl group is less adequate. The experimental data show that the  $\rho_s$  value of the symmetric  $\text{CH}_3$  stretch at the end of an alkane chain increase slightly with increasing chain length [132]. The methanol value would suggest a bond Raman anisotropy of  $\delta = 0.25$ . When we move from  $\delta = 0$  to  $\delta = 0.25$  the effect on the SFG intensities calculated below is a strengthening of the symmetric and a weakening of the asymmetric mode. The angular positions of maxima and minima in SFG intensity are only insignificantly changed.

Much less is known about the properties of the asymmetric modes and it is for this reason that we have to decompose the Raman tensor of the symmetric mode into tensors assigned to single bonds and then construct the Raman tensors of the two asymmetric modes. In this way we obtain for the vibration in the C – C – C plane:

$$\vec{A}_{asym,ip} = \begin{pmatrix} 1.15 \\ 0 \\ 0 \end{pmatrix} \quad (5.15)$$

$$M_{asym,ip} = \begin{pmatrix} 0.54 \cdot (1 - \delta) & 0 & 0.39 \cdot (1 - \delta) \\ 0 & -0.54 \cdot (1 - \delta) & 0 \\ 0.39 \cdot (1 - \delta) & 0 & 0 \end{pmatrix} \quad (5.16)$$

and for the vibration out-of-plane:

$$\vec{A}_{asym,op} = \begin{pmatrix} 0 \\ 1.15 \\ 0 \end{pmatrix} \quad (5.17)$$

$$M_{asym,op} = \begin{pmatrix} 0 & -0.54 \cdot (1 - \delta) & 0 \\ -0.54 \cdot (1 - \delta) & 0 & 0.39 \cdot (1 - \delta) \\ 0 & 0.39 \cdot (1 - \delta) & 0 \end{pmatrix} \quad (5.18)$$

As expected the dynamic dipole moments are thus along the  $x'$  and  $y'$  direction and they are larger than the one of the symmetric mode.

Finally, the tensors have to be transformed to their representations in the surface coordinate system  $(x'', y'', z'')$ . The orientation of the methyl group in the surface coordinate system is defined by the twist angle  $\tau$  (rotation  $D_{z'}(\tau)$ ) and tilt angle  $\vartheta$  (rotation  $D_{y''}(\vartheta)$ ) of the methyl group (see also Fig.5.2)

### 5.3.3 Intensity

The polarization induced in the molecules (Eq.2.8) gives rise to the radiation of the SF beam. We calculate the SF intensity by full evaluation of Eq.2.8 with all tensor elements  $\chi^{(2)}$  using the formalism for the Fresnel factors presented in chapter 2. The Fresnel factors are calculated for the experimental situation and are given in the appendix A.

### 5.3.4 Results

#### The SFG signal from a methyl group

Fig.5.9 shows 3-D plots of the SFG intensity in laboratory coordinates as a function of the angles  $\theta$  and  $\tau$ .

Here the amplitude was averaged over the azimuthal orientations of the molecule (rotation  $D_{z''}(\phi)$ , see also Fig.5.2). At the intensity maxima of the in-plane antisymmetric mode (Fig.5.9b), the  $\text{CH}_3$  group is oriented with one C–H bond pointing approximately towards the surface normal. This corresponds to the maxima at  $(\tau = 0^\circ, \vartheta \approx -60^\circ)$  and  $(\tau = 180^\circ, \vartheta \approx +60^\circ)$ . If we regard the intensity of the out-of-plane mode (Fig.5.9c) we find somewhat weaker maxima to occur as well for nearly perpendicular C–H bonds at  $(\tau \approx \pm 115^\circ, \vartheta \approx -60^\circ)$  and  $(\tau \approx \pm 25^\circ, \vartheta \approx \pm 60^\circ)$ . Thus only in orientations where one of the three C-H bonds points towards the surface normal strong SFG intensity can be expected. The maxima of the asymmetric modes are much sharper than for both, IRRAS or Raman spectroscopy which indicates the orientation sensitivity of the method.

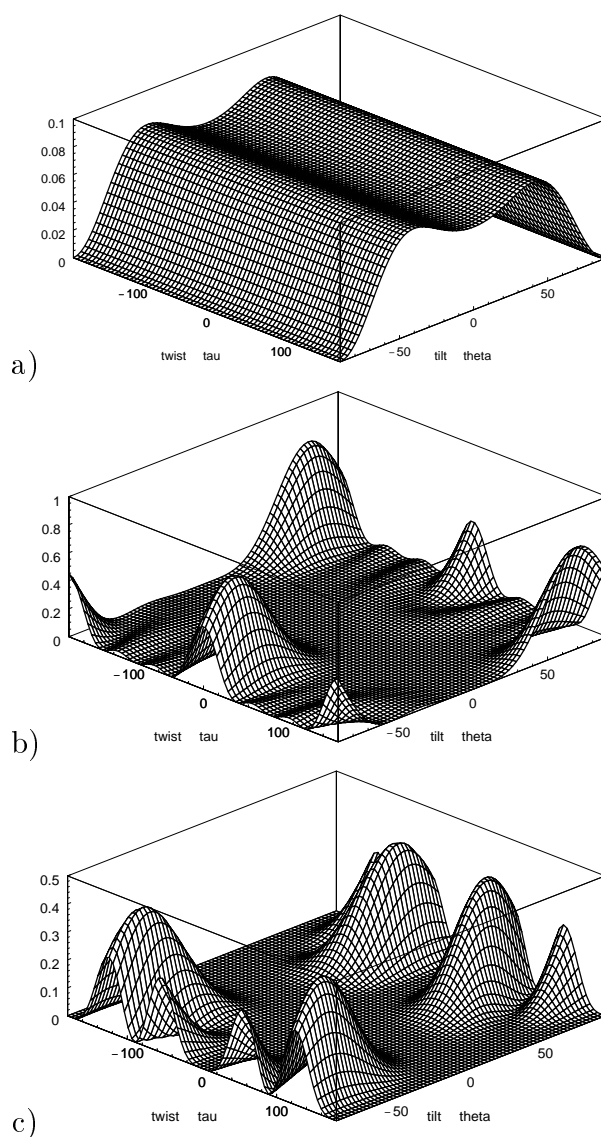


Figure 5.9: SFG intensity from the methyl group as a function of twist  $\tau$  and tilt  $\vartheta$  angle (in degrees). The amplitudes were averaged over all azimuthal angles  $\phi$ . Symmetric methyl stretch mode (a), in-plane antisymmetric mode (b) and out-of-plane antisymmetric stretching mode (c). The intensities are in arbitrary units, however, for the different modes the intensities can be compared.

### Averaging over a rotating $\text{CH}_3$ group and intensity ratio

At room temperature the  $\text{CH}_3$  group is known to rotate almost freely around the  $\text{C} - \text{C}$  axis [134]<sup>6</sup>. Thus an average over all twist angles has to be taken. If we average the *intensities* of the antisymmetric modes shown in Fig.5.9 b) and c) over all twist angles  $\tau$ , we obtain in both cases the result shown in Fig.5.10a). In this incoherent average (average of  $|\chi^{(2)}|^2$ ) we assumed that

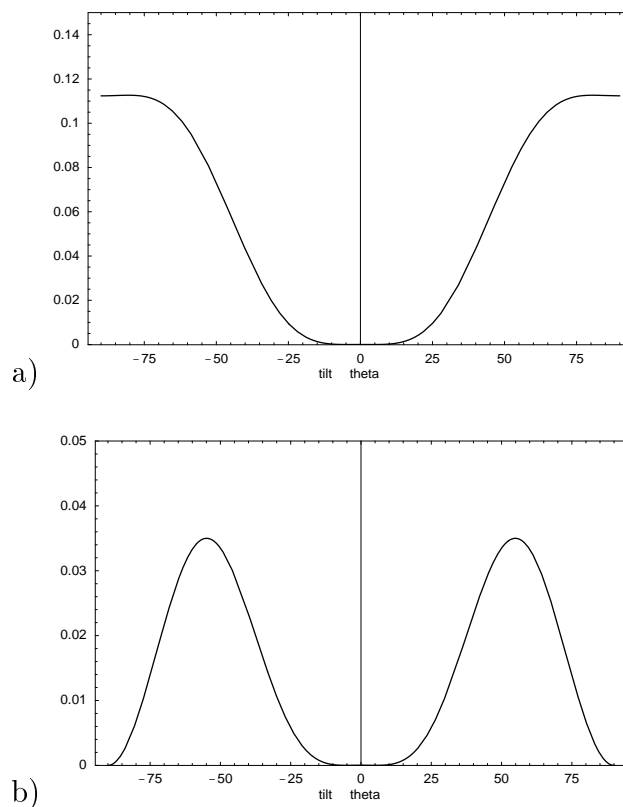


Figure 5.10: SFG intensity from the methyl group averaged over the twist angle  $\tau$ : Incoherent (intensity) average (a) and coherent (amplitude) average (b).

different orientations contribute independently to the intensity. However, as the frequency change of the vibration during the rotation is small compared to

---

<sup>6</sup>and references therein

its line width we have to take into account the interference from  $\text{CH}_3$  groups in different orientations at the instant when the sum frequency is generated. The corresponding coherent average (average of  $\chi^{(2)}$ ) is shown in Fig.5.10 b). SFG is a coherent technique, thus the coherent average has to be performed. In Fig.5.11 a) the coherent average for the symmetric and the antisymmetric stretching vibrations is presented. *From the intensity ratio of these vibrations (Fig.5.11 b) the tilt angle  $\vartheta$  of the methyl group can be determined.*

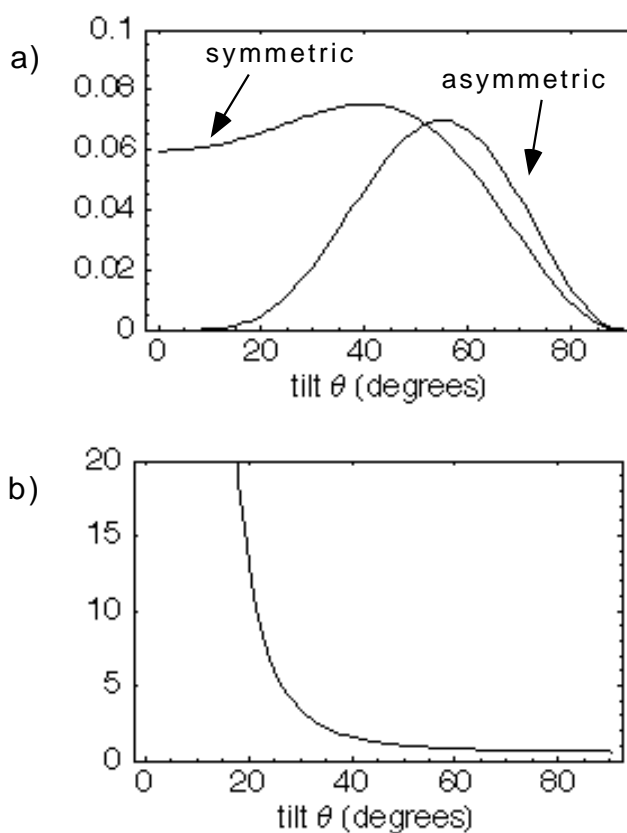


Figure 5.11: a) SFG intensity of symmetric to antisymmetric methyl stretch modes as a function of tilt angle (in degrees). b) SFG intensity ratio of symmetric and antisymmetric methyl stretching mode.

### 5.3.5 Analysis of spectra - Test of the model

In order to test the model we determine the tilt angle  $\vartheta$  of the methyl group of the C<sub>18</sub> thiolate from the SF spectrum presented in Fig.5.6 a).

The value  $I_{SFG}$  calculated in the model represents the square of the amplitude of the radiated SF field. In cases where the signal interferes with a much stronger substrate signal the in the spectra observed amplitude has to be squared in order to compare the data with the calculation. Similarly, when the symmetric mode is split by Fermi resonance both amplitudes have to be added, then squared in order to compare the data with the calculation.

Table 5.2 presents the quantitative analysis of the C<sub>18</sub> spectrum in (Fig. 5.6 a). The intensity ratio is calculated by summing the values of the two relative amplitudes of the symmetric resonances ( $r_a^+FR$  and  $r_b^+FR$ ) dividing it by the relative intensity of the asymmetric resonance  $r^-$  and squaring the result. One obtains a value of  $5.6 \pm 0.8$ .

$r_a^+FR$			$r_b^+FR$			$r^-$			$Res.$
<i>pos.</i>	<i>width</i>	<i>rel.ampl.</i>	<i>pos.</i>	<i>width</i>	<i>rel.ampl.</i>	<i>pos.</i>	<i>width</i>	<i>rel.ampl.</i>	$(\frac{B_{r^+}}{B_{r^-}})^2$
2877	11	$22 \pm 2$	2935	13	$16 \pm 2$	2966	10	$16 \pm 2$	$5.6 \pm 0.8$

Table 5.2: Quantitative analysis of the spectrum in Fig.5.6. The position and the widths (FWHM) of the resonances are given in  $\text{cm}^{-1}$ . The relative amplitude is the height of the resonance with respect to the nonresonant substrate background in percent.

As can be inferred from the graph in figure 5.11 b) this corresponds in the frame of the model to a methyl tilt angle of

$$\vartheta = 24^\circ \pm 1^\circ \quad (5.19)$$

This has to be compared with the literature values. However, normally not the methyl tilt angle is given there, but the *molecular* cant (or tilt) angle  $\alpha$  and the twist angle  $\beta$  of the C-C-C plane (see figure 5.2). These two angles have to be converted to  $\vartheta$ . Care has to be taken in order to properly include thiolate chains with odd and even number of carbon atoms. As can be seen

from figure 5.2, for  $\alpha = 0$  and  $\beta = 0$  the methyl axis points in the direction of negative  $\alpha$  values if  $n$  is even. For odd  $n$  it points in directions where  $\alpha$  is positive.

The molecular orientation of alkyl chain thiolates on gold has for example been determined by quantitative reflection infrared spectroscopy to  $\alpha \sim 34^\circ$  and  $\beta \sim 55^\circ$  [123] which corresponds to  $\vartheta = 30^\circ$ . A similar study [93] found  $\alpha = 26^\circ$  and  $\beta = 52^\circ$  or  $\vartheta = 27^\circ$ . With near edge x-ray absorption fine structure (NEXAFS) [135] the angles have been determined to  $\alpha = 35^\circ$  and  $\beta = 45^\circ$  yielding<sup>7</sup>  $\vartheta = 25^\circ$ . Finally a SFG study [127] directly determined  $\vartheta = 26.4^\circ \pm 1.8^\circ$  for a C<sub>22</sub> SAM by analyzing the intensity ratio of the r<sub>a</sub><sup>+</sup>FR resonance in *ppp*- and *ssp*-polarization.

Thus, the results of the model are in good agreement with the literature values. It has to be noted that due to the simplifying assumptions made for the construction of the tensor elements a high accuracy can not be expected. However as will be seen, an accuracy of several degrees is sufficient and the interpretation of the measurements of chapter 5.5 is not limited by the accuracy of the model.

Another remark concerns the compatibility of the reported  $\alpha$  and  $\beta$  values with the hybridization state of the sulfur. Assuming the Au-S bond parallel to the surface normal and a *sp*<sup>3</sup> hybridization (tetrahedral angle 109.5°) the minimum value for  $\alpha$  is 35.25°. This is for  $\beta = 0^\circ$ , higher  $\beta$  values increase  $\alpha$  (see also figure 5.2). This means that for example the combination of  $\alpha = 26^\circ$  and  $\beta = 52^\circ$  is incompatible with an exact *sp*<sup>3</sup> hybridization.

## 5.4 Instability of C<sub>6</sub> thiolate in air

Long chain alkyl thiolates on gold are stable in air [118]. We were able to verify this with the C<sub>18</sub> thiolate. The SFG and IR spectra remained unchanged from several days up to several weeks. In order to prepare the in-situ copper deposition measurements (see chapter 5.5) where the influence of long and

---

<sup>7</sup>NEXAFS measurements are not sensitive to even or odd  $n$ . The influence of the methyl group was negligible against the greater number of the methylene groups. Thus the determination of  $\vartheta$  is not unique. The other value is  $\vartheta = 64^\circ$  which we would associate with an odd  $n$ .



short chain alkanethiolate SAMs is investigated, we also measured a C<sub>6</sub> thiolate SAM in air in order to elucidate the effect of the different ordering of short chain thioliates in the SFG spectra.

It turned out, that successively recorded spectra did *not* show the same result. The strong resonances become weaker with time until they vanish. Figure 5.12 shows this behavior.

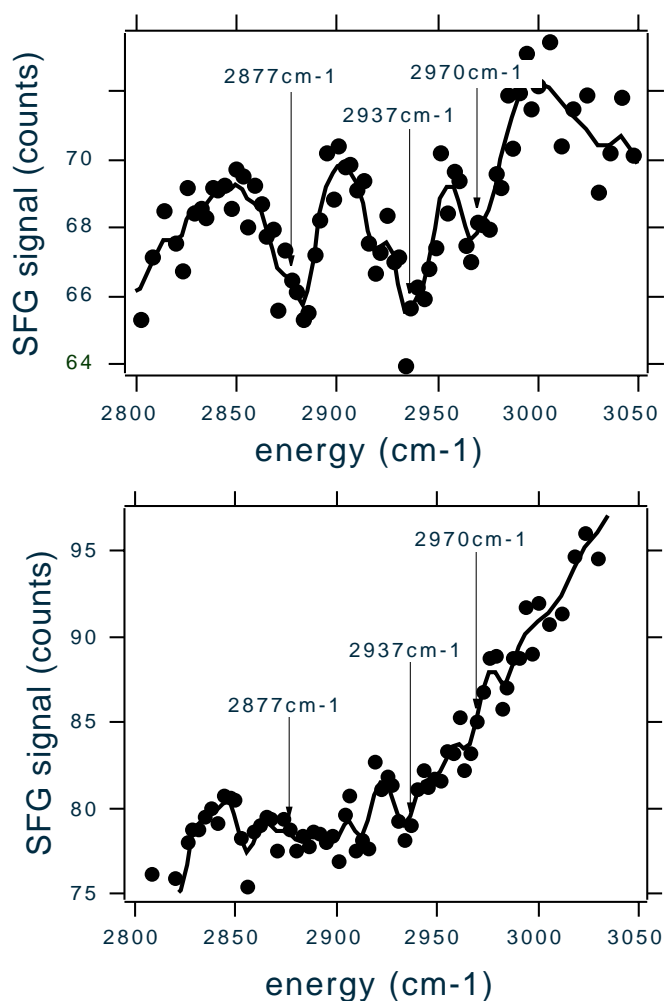


Figure 5.12: Hexanethiolate SAM: SF spectra in air. a) directly after preparation, measurement from 0-2 hours b) measurement from 2-4h

The disappearance of the resonances can have different reasons. The SAM can become disordered, can be destroyed or can desorb.

- Disordering can come from absorption of the IR-light or from energy dissipation which heats the crystal and the SAM.
- The destruction of the SAM can be induced through high laser intensities and the multiphoton processes which come along.
- Desorption can be temperature-induced and arise after the disordering of the SAM or can come from the oxidation of the sulfur group which can be due to the simultaneous presence of laser light and oxygen (photo oxidation)

Disordering or desorption of the hexanethiolate SAM are unlikely to come from the energy deposition and heating of the substrate since the measurements of C<sub>18</sub> and C<sub>6</sub> have been performed under the same conditions. In fact the binding energies of C<sub>18</sub> and C<sub>6</sub> are very similar. The major contribution comes from the S-Au bond of which the energy is 126 KJ/mol. The van-der-Waals interaction per methylene unit in an ordered SAM is about 2.8 kJ/mol [136] and thus small compared to the energy of the thiolate bond. Since the binding energies of C<sub>6</sub> and C<sub>18</sub> are comparable, C<sub>18</sub> should also desorb if C<sub>6</sub> does. The heating should at least cause disorder i.e. create a substantial number of gauche defects in the in the C<sub>18</sub> SAM [137] which would lead to the appearance of methylene bands in the C<sub>18</sub> spectra [119]. This is why temperature rise can be ruled out as reason for the disappearance of the SAM.

The disappearance of the resonances has also been reported by Lampert et al. [127] for all alkanethiols with chain lengths shorter than C<sub>12</sub>. They observed additionally a simultaneous increase of the nonlinear background has been observed. Further investigations showed that the short chain thiolate SAMs, which are unstable in air, are stable when measured with the same parameters under nitrogen atmosphere [127] excluding thus the destruction of the SAM through high laser energies and multiphoton processes.

The increase of the nonresonant background indicates that the electronic structure of the substrate surface is changed. In fact, the adsorption of thiols on gold diminishes the nonresonant gold signal and this independently from the chain length [138]. Inversely, the rise of the nonlinear background indicates

a decrease of sulfur gold bonds and is, together with the disappearance of the resonances, consistent with the desorption of the SAM.

## 5.5 Alkanethiolates ( $n = 6, 12, 18$ ) and electrochemical copper deposition

### 5.5.1 Introduction

Electrochemical deposition of Cu on Au(111) is drastically changed when the Au surface is functionalized with alkane thiolates. The system has been extensively investigated by means of scanning tunneling microscopy (STM) [80, 117, 139–141], thus detailed structural information on the deposition process is available. In this chapter we study the deposition process by STM and from the adsorbates point of view by *in-situ* vibrational SF spectroscopy. The outline of this Chapter is the following: we briefly introduce the interface *electrode-electrolyte*, specifically for the case of an alkanethiolate-covered electrode. Then, a short STM study provides the microscopic image of Cu adsorption on the modified electrodes. Finally the SF spectra are presented.

#### The electrode/electrolyte interface

The interface between electrode and electrolyte has a special structure which is called *double layer*. In the literature different models for the double layer are proposed. Here only the diffuse layer model (Gouy-Chapman) will be considered. Near the electrode one distinguishes two regions: First a compact layer which bears no charge. Its boundaries are the electrode surface and a plane which is called Outer Helmholtz Plane (OHP) and which is the plane of closest approach of solvated ions. Only specifically adsorbed ions directly contact surface atoms. These specifically adsorbed ions are of special interest, since they are bound at the surface and can form monolayers. Only these ions or ions directly situated at the OHP can be oxidized or reduced. The center of the specifically adsorbed ions is called Inner Helmholtz Plane (IHP, also see Fig.5.13).

The diffuse layer starts at the OHP and slowly merges into the bulk of the solution. In this diffuse layer the distribution of ions in the solution changes from a distorted, slightly ordered distribution at the OHP to a random distribution in the bulk.

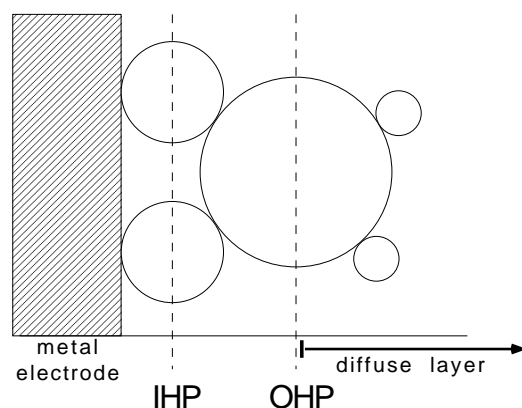


Figure 5.13: Schematic model of the interface in presence of specific adsorption.

The modification of the interfacial structure by the deposition of an organic layer on the metal electrode, requires an adaptation of this model. Thus, in aqueous electrolytes and in the case of  $\text{CH}_3$ -terminated thiolate monolayers, specific adsorption of ions is not likely to occur because of the hydrophobicity of the monolayer outer interface. This is why no IHP can be defined. An OHP, as well as a diffuse layer do exist. Concerning the potential distribution *in* the organic layer, it has been proposed in an electrochemical study of alkanethiolate-modified gold electrodes [142] that there is a linear decay taking place within the monolayer. Figure 5.14 shows the potential distribution for this case.

### Copper deposition on bare Au(111)

When considering electrodeposition of a metal (Me) on a metallic substrate (Sub) two different potential ranges can be distinguished: above and below the Nernst equilibrium potential. At this Nernst equilibrium potential the reduction/oxidation reaction  $\text{Me}^{z+} + ze^- \longleftrightarrow \text{Me}$  has the same speed in both directions. In some Me/Sub systems the metal deposition occurs already at

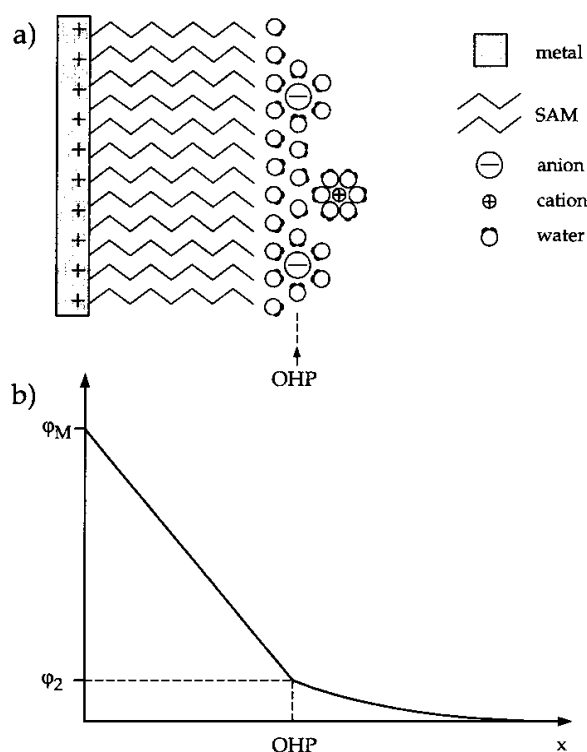


Figure 5.14: Schematic models of the ion (a) and potential (b) distribution across the metal/SAM/electrolyte interface [117]

potentials positive of the equilibrium Nernst potential. This is called underpotential deposition (UPD) and can be explained by a Me-Sub interaction which is stronger than the Me-Me one. In contrast, the case where metal is deposited at potentials negative of the equilibrium Nernst potential is referred to as overpotential deposition (OPD). Here Me is deposited onto Me, independent of the Me-Sub interaction.

The deposition of Cu on bare Au(111) is known from the literature [143–149] and it has been shown that there exist two potentials in the UPD range where Cu adsorbs. Here we will quote all potentials against the  $\text{Cu}/\text{Cu}^{2+}$  (1mM) potential, where 0 mV correspond to +250 mV on the standard hydrogen scale. In the  $\text{Cu}/\text{Cu}^{2+}$  notation the first potential where Cu adsorbs is at about +230 mV and corresponds to the adsorption of Cu in a  $(\sqrt{3} \times \sqrt{3})\text{R}30^\circ$

adlayer. When decreasing the potential to about +50 mV, another current peak indicates Cu adsorption in a  $1 \times 1$  overlayer.

After completion of the first Cu monolayer (below +50mV), no further deposition occurs in the UPD range. Bulk deposition of Cu starts at potentials below the Nernst equilibrium potential. The growth mode in the OPD range is three-dimensional (Stranski-Krastanov).

### Copper deposition on alkanethiolate covered Au(111) and STM data

The modification of the bare gold electrodes through the adsorption of self-assembled alkylthiol layers causes a drastic change in the electrochemical properties. It should be noted here that the electric potential of the interface SAM-electrolyte is not known (see above). This is why we are constrained to refer to the potential of the gold electrode. The most important change is that the adsorbed thiolate SAM exhibits a blocking behavior i.e. the faradaic current is one order of magnitude smaller than in the case of a bare gold electrode. Also the UPD copper deposition peaks at +150mV and +50mV are absent. However, as proved with STM (Scanning Tunneling Microscope) Cu adsorbs already at potentials below +200 mV. This is why we will call the range from 0 mV to +200 mV UPD range and the zone below 0 mV OPD range.

The structure of electrodeposited copper on alkanethiolates is well known for a variety of chain lengths  $n$ , temperatures, and potentials [80, 117, 139, 140, 150]. In our experiments we held the temperature at 300 K and varied the potentials for  $n=6, 12$  and 18 (the phenomena in the absence of copper will be discussed below). We started at a potential of +400 mV where copper deposits neither on bare nor on thiolated gold, then lowered the potential. The most important observation is the formation of monolayer high islands with an average diameter of 2 nm. After completion of the formation (ca. two hours) they cover 10 to 15 % of the surface. XPS confirmed the presence of copper on the emerged and water-rinsed surface [80], thus we can safely assume that the islands consist of copper. We observed that the islands only form behind a "growth front" (see figure 5.15) in an area where the thiolate layer is imaged topographically higher than usual, corresponding to lower resistivity. Such areas, attaining more than  $0.1 \mu\text{m}^2$  after 1 h, form randomly on the sample and are not tip-induced, as proven by the simultaneous observation of several areas in one image [117]. Outside the areas the normal thiolate structure prevails.

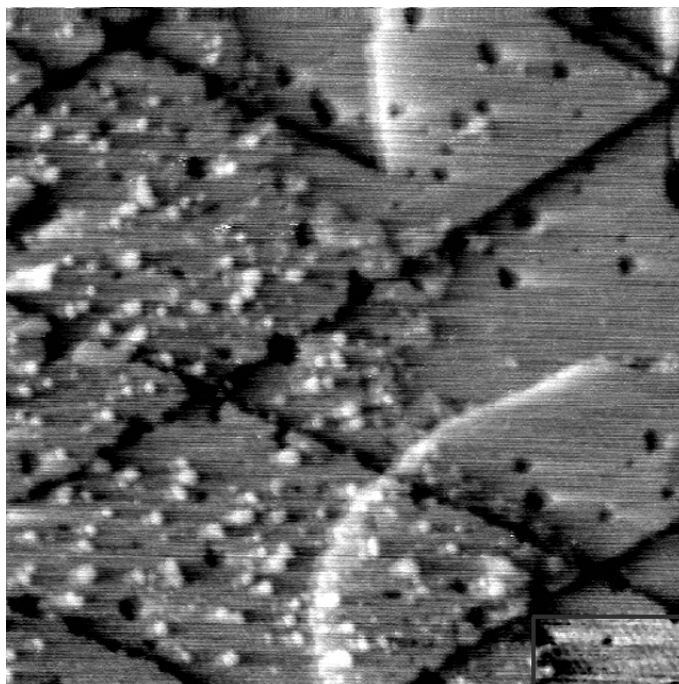


Figure 5.15: 228 nm x 228 nm in-situ STM image showing the 2D copper island formation on a C<sub>6</sub> SAM thiolate-covered Au(111) surface in the UPD range [151]. Electrolyte: 50 mM H<sub>2</sub>SO<sub>4</sub> + 1 mM CuSO<sub>4</sub>. Electrode potential: 150 mV vs. Cu/Cu<sup>2+</sup>, applied for 41 min (reference electrode here: copper wire). An irregular formed step is propagating from left to right. Its height is much lower than that of the straight or slightly curved substrate steps. Behind this "front", on the left part of the image, copper islands (bright spots, diameters ca. 2 nm) have formed, and molecular resolution is difficult. The unaffected area (right part, see also contrast-enhanced inset) shows the striped structure typical of a C<sub>6</sub> SAM thiolate.

We estimated the following coverages: Copper 10%, copper-free surface 80%, island rims 10% (assuming steps with a width of two atoms, one Cu, one Au). For  $n=18$  this scenario is valid for all potentials below ca. +150 mV.

In contrast, for  $n=6$  and 12, below ca. -100 mV a pseudo-layer-by-layer growth called "pseudo" Frank-van-der-Merwe was found: Islands grow until they coalesce; pseudo means that a second layer nucleates before the first is completed. Only islands that have already nucleated above 0 mV grow, further islands form only on existing copper islands. For  $n=6$  we observed a fractal shape of the growing and coalescing islands and a growth of about one layer per hour. Now the copper covers about 80%, of the surface, and the rest are island rims.

In order to evaluate the influence of an electrochemical potential on an adsorbate, one usually elucidates the action of the potential in absence of the deposited substance. Hence we undertook an in-situ STM study of the  $\text{CH}_3(\text{CH}_2)_{n-1}\text{S}/\text{Au}(111)$  surface for  $n=6, 12, 18$  under potential control in diluted, copper-free  $\text{H}_2\text{SO}_4$ . The well-known thiolate layer topography was reproduced: the surface consists of terraces, monoatomic (gold) steps and the substrate vacancies that are typical for thiolate-covered gold (see figure 5.16c). In some cases we detected cluster-like defects that were always pinned to steps (see figure 5.16b). This observation is valid for  $n=6, 12$  and  $18$  down to  $-200$  mV, i.e. for all potential regions investigated by SF spectroscopy (see below).

When we lowered the potential further (down to  $-400$  mV which corresponds to very fast copper bulk deposition in  $1$  mM  $\text{Cu}^{2+}$  and even to hydrogen evolution), monoatomic high islands with a diameter in the  $5$ - $10$  nm range form ( $n=6, 12$  and  $18$ , see figure 5.16a). This diameter is clearly larger than the average copper island diameter of  $2$  nm [117]. For  $n=18$  and currents above  $5$  nA (where the tip is presumably in touch with a large number of alkyl chains) we found that steps could move by  $20$  nm/min. These two observations lead us to postulate a potential-induced gold island formation. Such reconstruction phenomena of adsorbate-covered metals are well known for systems like short chain thiolates [152] or iodine on fcc-(110) surfaces [153, 154]. In these cases and also for longer chain alkanethiolates, the influence of the STM tip, especially at high tunneling currents (i.e. low distances) can be very large.

What is more important for us, is the fact that the initial structure ( $+400$  mV) does not change at potentials higher than  $-200$  mV. In view of the limited vertical resolution we cannot exclude the formation of disordered structures (lower tunneling resistivity, higher topography, but less than a substrate step), but we can exclude the formation of gold islands.



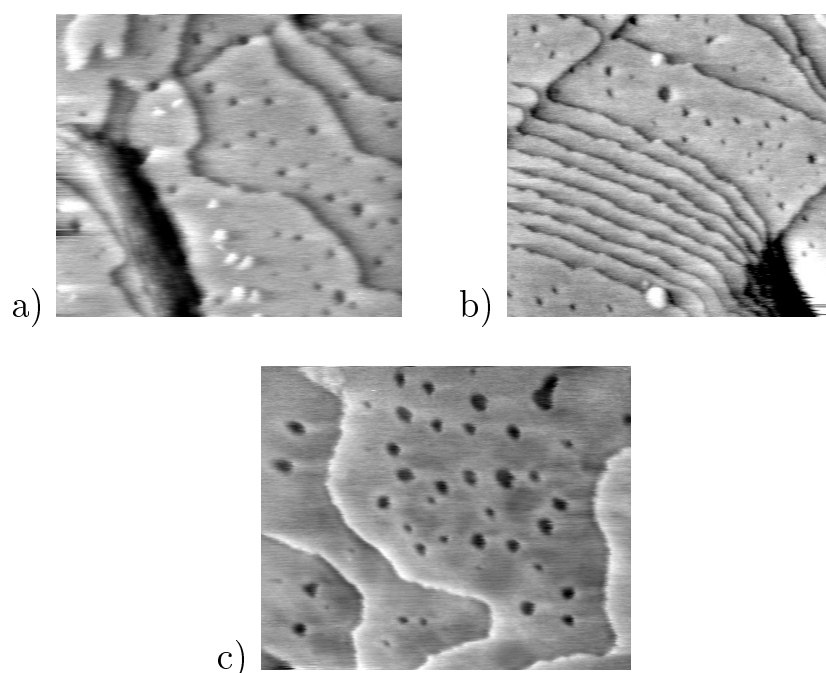


Figure 5.16: In-situ STM images showing a thiolate-covered Au(111) surface in 50 mM  $\text{H}_2\text{SO}_4$ . Surprisingly, the differences between the images are due to the different sample potentials, not due to the different chain lengths. (a)  $\text{C}_{18}$  SAM thiolate at -400 mV vs. a hypothetical  $\text{Cu}/\text{Cu}^{2+}$  (1mM) reference, 142 nm x 125 nm. Tunneling parameters:  $I = 25$  nA,  $V = 1200$  mV vs. sample. The black lines are substrate steps (the large black line in the lower left stems from a multistep); the gray terraces show the usual substrate vacancies (black spots). Islands (presumably gold, bright spots) become visible only at this extremely negative potential. (b)  $\text{C}_{12}$  thiolate at -250 mV.  $I = 2$  nA,  $V = 300$  mV, 142 nm x 129 nm. The situation is very similar to (a), but the potential is not sufficiently negative to create islands (only the two bright spots attached to substrate steps were observed, but no new islands formed). (c)  $\text{C}_6$  SAM thiolate at -50 mV.  $I = 10$  nA,  $V = 380$  mV, 142 nm x 116 nm. At this potential no islands could be observed. The substrate vacancies are rather large, as is typical for short chain thiolates.

## 5.5.2 Experimental

### Electrochemical setup

For the SFG measurements in the electrochemical cell only gold single crystals were used. A gold wire which connects the sample electrically is prepared like the crystal (see chapter 5.2.2) - but without the annealing procedure. After

preparation they are immediately mounted in the electrochemical cell and covered with the electrolyte, 50 mM  $\text{H}_2\text{SO}_4$  (p.a., Fluka) + 1 mM  $\text{CuSO}_4$  in water (Millipore). The reference electrode was a copper wire, etched in  $\text{HNO}_3$  and rinsed with water shortly before use. The counter electrode was a clean platinum wire. We always employed an EG&G PAR 400 potentiostat.

For the control experiments in the copper free electrolyte (50 mM  $\text{H}_2\text{SO}_4$  in water) the reference was a palladium wire at which hydrogen had been evolved for at least 30 min (testing the obtained Pd/H electrode showed an offset of 100 mV and in some experiments also a drift of ca. -40 mV/h for that we corrected).

The electrochemical cell for the SFG setup is made of poly-chlorotrifluoroethylene (PCTFE). While in electrochemical preparation the surface must be covered by a thick electrolyte layer, for the SFG measurements a thick electrolyte layer would lead to strong absorption of the IR beam. This is why an equilateral  $\text{CaF}_2$  prism is lightly pressed against the horizontally mounted sample surface during SFG measurements in order to minimize the thickness of the electrolyte layer. The prism is fixed in a freely rotating gimbal mount (two rotational degrees of freedom) in order to allow the prism surface to adjust parallel to the sample surface avoiding at the same time sample scratches which would occur if the prism could slide (see figure 5.17). This is a *new* design for an electrochemical cell. The main advantage of this open design is that the cell is very easy to clean and to handle. The amount of electrolyte between surface and prism is now determined only by the macroscopic roughness of the sample and the prism faces, so that only a thin electrolyte layer remains between the prism and the sample surface.

In-situ SFG spectra were taken after a sample had been immersed in electrolyte and held at a defined potential. For potentials above 200 mV (no copper deposition) the minimal holding time was 15 min; for all other potentials the minimal time was one hour. These times were chosen in accordance with typical copper deposition rates observed with STM [80, 139, 141]. After this holding time the prism was lowered onto the surface reducing the currents and the amount of electrolyte available above the surface but keeping the potential control. Recording SFG spectra took typically two hours per potential before the prism was lifted and the potential was changed. The spectra were averaged over several measurements covering 2h to 10h acquisition time.

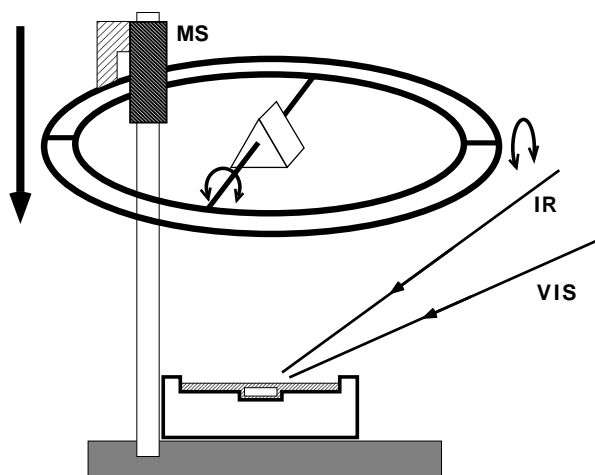


Figure 5.17: The figure shows the gimballed mount to which the  $\text{CaF}_2$  prism is fixed. The outer ring of the gimballed mount is fixed to a micrometer screw (MS). The laser beams are in the same plane as the surface normal of the entrance face of the prism.

### Evaluation of the SFG data

As discussed, the infrared beam can be absorbed by the electrolyte film which is between electrode surface and  $\text{CaF}_2$  prism, due to the macroscopic surface roughness of the electrode and the prism. This fact is illustrated by the continuous signal decrease with increasing wavenumbers in the  $\text{C}_{18}$  SAM spectrum in figure 5.18. The corresponding water absorption line is centered around  $3400\text{ cm}^{-1}$ . The spectrum is dominated by the non-resonant SFG signal from the gold substrate on which the thiolate resonances appear as small negative peaks. In order to present spectra in which the thiolate resonances are clearly discernible, the spectra were fitted by the smooth IR absorption curve of water and then divided by the fitted curve. It was found that fitting simply with a slowly varying polynomial (usually of order 5) is more efficient and gives essentially the same result. The reason is that small variations of intensity due to changing beam alignment can in this way be corrected as well. These normalized spectra are presented. We made sure that the procedure preserves the SFG vibrational resonances while the signal attenuation due to the IR absorption of water is removed. As the fitting procedure provides a mean intensity

of the normalized spectrum of one, strong negative peaks can create broad positive peaks in their wings. One has to be aware of such artifacts when evaluating the spectra.

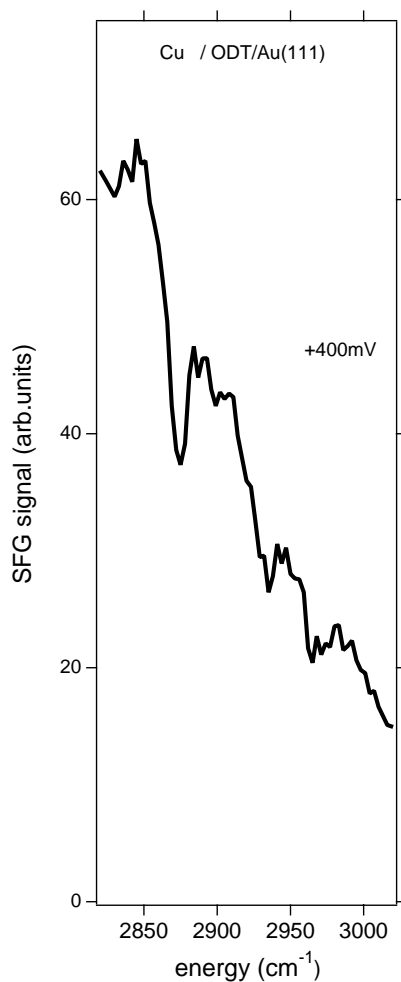


Figure 5.18: SFG spectrum of  $C_{18}$  SAM/Au(111) in-situ in a copper solution at the open circuit potential. The SFG intensity is presented as it is recorded but represents an average of several measurements. The slope of the background is due to absorption in the aqueous solution. After normalization, as described in the text, the upper spectrum in Fig. 5.19 is obtained.

### OPO measurements

The experiments on the C<sub>12</sub> SAM were carried out at LURE-CLIO (Orsay, France) in cooperation with W.Q. Zheng and A. Tadjeddine, and they furnished the first evidence of the influence of the copper deposition. At CLIO, an optical parametric oscillator (OPO) was employed which is based on an active passive mode locked Nd:YAG Laser delivering a train of pulses to a rotatable lithium niobate (LiNbO<sub>3</sub>) crystal that is in turn placed in a near-infrared lasing cavity (signal wavelength ca. 4700 to 6800 cm<sup>-1</sup>). The corresponding mid-infrared idler pulses of ca. 4700 to 2600 cm<sup>-1</sup> have a duration of 11 ps and a width of 2 cm<sup>-1</sup>. They are mixed on the sample with 10 ps long pulses of the doubled fundamental. Beam geometry and detection are similar to the OPG/OPA except for the reference signal which is produced by mixing a part of the infrared and the visible beam in a ZnS plate. The electrochemical cell setup is also similar except for a closed design and a vertically oriented sample. Details can be found in [4].

### 5.5.3 Stability of the SAMs in the electrolyte and their initial structure

In chapter 5.2.3 and 5.4 we investigated C<sub>18</sub> and C<sub>6</sub> in air, and one result was that the C<sub>6</sub> SAM is not stable under the measurement conditions. At this point we will investigate the behavior of the SAMs in H<sub>2</sub>SO<sub>4</sub> electrolyte and specifically during copper electro-deposition. Results from electrochemical STM studies indicate that C<sub>18</sub> and C<sub>6</sub> SAMs are stable in the electrolyte over at least a few hours, in the potential range from -200mV to 500mV [80]. Additionally, the SAMs exhibit the blocking behavior described in section 5.5.1. Hines et al. [109] report that vibrational spectra of C<sub>18</sub> on gold in a HClO<sub>4</sub> (0.1M) electrolyte remain unchanged when the potential is cycled from -50mV to 1150mV vs. a hypothetical Cu/Cu<sup>2+</sup> reference. Below -200 mV thiolate layers become damaged and can desorb reductively at very negative potentials in basic electrolytes [155], while above +1100 mV they are oxidatively damaged [141]. In order to exclude potential induced damages of the SAMs we restrict ourselves in this study to the potential range from -200mV to +400mV.

Figure 5.19 presents the normalized spectra of C<sub>6</sub> and C<sub>18</sub>. The potential is +400 mV where no copper adsorbs. The most important observation is

that the  $C_6$  SAM in the electrolyte is stable under the measurement conditions, which is a prerequisite for the potential dependent investigations. The spectrum is dominated by the three well known methyl stretching peaks. No methylene vibrations are visible, which again indicates the absence of gauche defects.

The other important information is that the  $C_{18}$  spectrum in the electrolyte is very similar to the one in air, thus indicating that the SAM has nearly the same geometry as in air. However the methyl peaks are somewhat broader which could result from the interaction of the terminal methyl group with the electrolyte.

Comparing the  $C_6$  spectrum with the  $C_{18}$  spectrum, the most obvious feature is that the intensity (relative to the nonresonant gold background) of the resonances in the  $C_6$  spectrum is about half as strong as in the  $C_{18}$  spectrum. Intensity changes due to disordered  $C_6$  SAMs can be excluded, since on one hand the self-assembly time was long enough to produce well ordered films and on the other hand spectra from disordered SAMs should exhibit methylene resonances. Since the intensity varies linearly with the number of molecules - when the contribution of the nonresonant background is much larger than the one of the molecules (see Eqs.5.1 and 5.5) - the density of the detected  $C_6$  molecules is about half as large as the density of the  $C_{18}$  molecules. But from the excellent blocking behavior of the  $C_6$  SAM we can infer that the gold electrode is completely covered by the SAM. This seeming contradiction can be solved when we assume that half of the electrode surface is covered by the usual densely packed  $(\sqrt{3} \times \sqrt{3})R30^\circ$  phase and the other half is covered by a striped phase (see chapter 5.1) and that this striped phase can not be detected by SFG. The fact that each phase covers half of the surface is in accord with studies where it has been found that for  $C_6$  thiolate SAMs, the gold electrode is covered by about 50% with the dense  $(\sqrt{3} \times \sqrt{3})R30^\circ$  phase and by about 50% with the striped phase [117], although the exact ratio of coverage ratio depends on the sample. The assumption that the striped phase cannot be detected with SFG is a bit more difficult to justify, since the structure of this phase is still under discussion. But taken one of the proposed possibilities where the chains are parallel to the surface (chapter 5.1) entailing a tilt angle  $\alpha$  and a twist angle  $\beta$  near  $\pm 90^\circ$ , it follows that the inclination  $\vartheta$  of the  $C-CH_3$  axis is near  $90^\circ$  too. As has been discussed in chapter 5.3, conformations with  $\vartheta = 90^\circ$  are not detectable by SFG. Thus, based on the fact that  $C_6$  SAMs

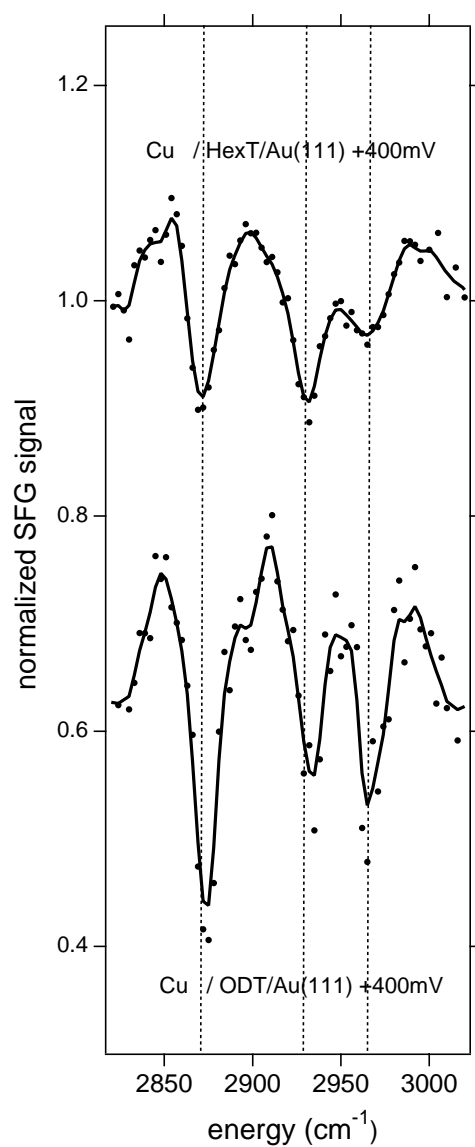


Figure 5.19: Normalized SF spectra of C<sub>18</sub> and C<sub>6</sub> SAMs in the electrolyte at +400 mV (vs Cu/Cu<sup>2+</sup>) where no Cu adsorbs.

yield half of the intensity of C<sub>18</sub> SAMs, we will take as working hypothesis for the rest of this chapter that the electrode is covered with equal parts of the

two phases before Cu is adsorbed.

In table 5.3 and 5.4 the spectra of figure 5.19 are evaluated. The intensity ratio in the electrolyte at +400mV is  $10.9 \pm 2.4$  for  $C_6$  and  $5.1 \pm 1.5$  for  $C_{18}$  which corresponds to  $\vartheta = (21 \pm 1.5)^\circ$  and  $\vartheta = (27 \pm 2)^\circ$ , respectively. Thus we found only little variations of  $\vartheta$  for the cases of  $C_{18}$  and  $C_6$  in electrolyte and  $C_{18}$  in air and can therefore assume that the conformation of the dense phases in the three cases is very similar.

#### 5.5.4 Change of the spectra through Cu deposition

After having developed some aspects of the structure of the  $C_6$  and  $C_{18}$  SAM in the electrolyte at +400 mV where no Cu is adsorbed, we will now lower the potential in the UPD and then in the OPD range in order to search for the influence of copper deposition in the spectra. Figure 5.20a) demonstrates the dramatic dependence of the  $C_6$  spectra on the copper deposition. We can see that the resonances due to the symmetric methyl stretching vibration  $r_a^+$  and  $r_b^+$  vanish. The asymmetric stretching vibration resonance  $r^-$  seems to increase, a quantitative analysis of the spectra (see table 5.3) however shows that its intensity stays about the same. We will term the spectra where the  $r_a^+$  and the  $r_b^+$  resonances are stronger than the  $r^-$  resonance, type I spectra. The spectra where the  $r_a^+$  and the  $r_b^+$  resonances are weaker than the  $r^-$  resonance are termed as type II.

An important point to verify was whether the change from type I spectrum to type II spectrum is actually induced by the copper deposition and not by the potential change. This is why we have repeated the measurements with a copper free electrolyte and a hydrogen saturated palladium reference electrode. The potentials are reported versus a hypothetically Cu/Cu<sup>2+</sup> reference. It can be seen from figure 5.20b) that the type I spectrum remains type I upon potential changes in the copper-free electrolyte. This result is not self-evident, even though - as shown by Hines et al. [109] - potential changes do not influence the spectra of  $C_{18}$  on gold and silver, since they also showed that  $C_{18}$  SAMs on platinum exhibit drastic potential dependent conformational changes. This is probably due to the less ordered and thus more open structure of the SAMs which allows ions from the electrolyte to penetrate the SAM.

Calculating the methyl group tilt angle with the intensity ratio  $0.83 \pm$



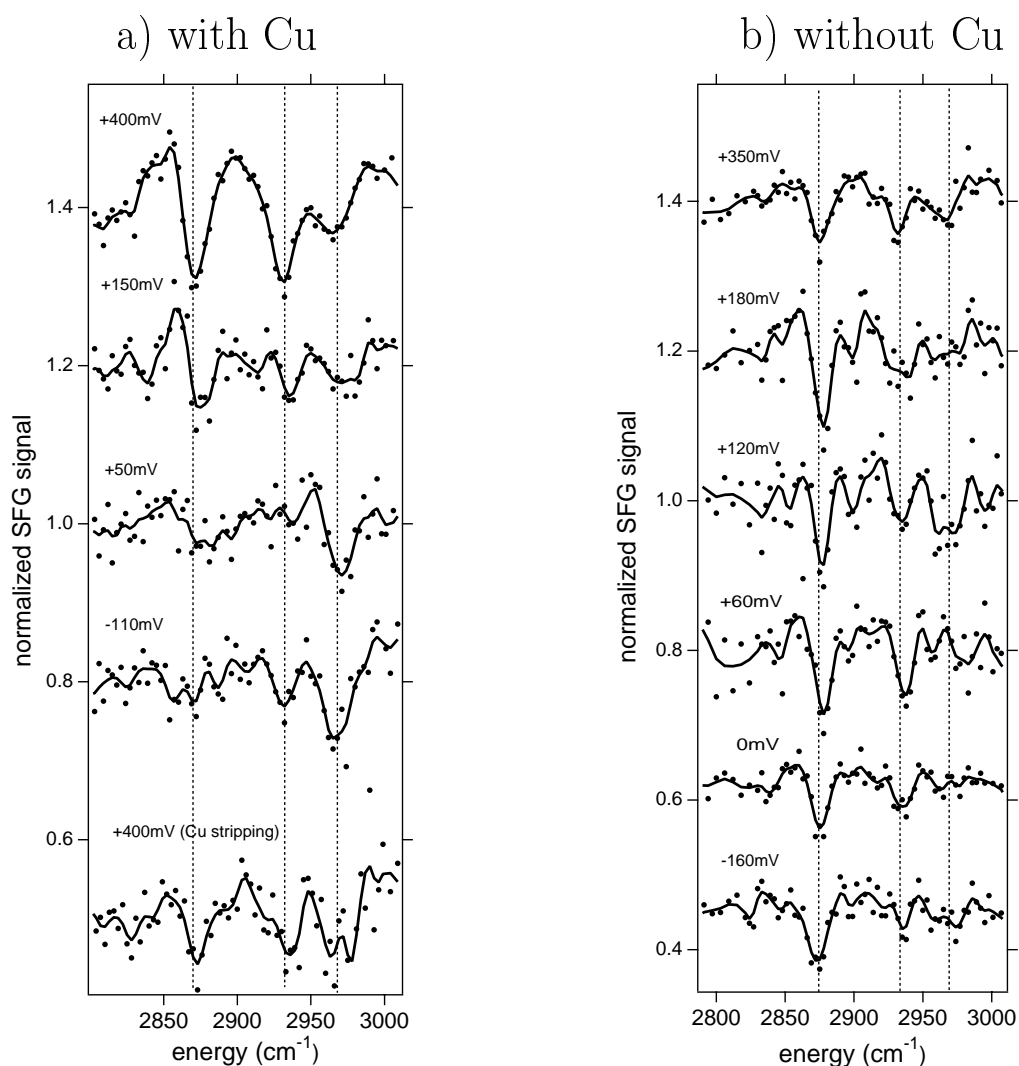


Figure 5.20: Normalized spectra of C<sub>6</sub>: during Cu deposition (a) and the potential dependence in a Cu-free electrolyte (b).

0.56 from table 5.3 yields  $\vartheta = 63^\circ$ . The error bar is large however, so we can only conclude that  $\vartheta > 45^\circ$  when evaluating only the intensity ratio (see figure 5.11 b). Additional arguments help to reduce this large range of  $\vartheta$  values. The key ingredient is that the intensity of the  $r^-$  resonance remains approximately constant. There is one other angle where the  $r^-$  resonance has

Potential	$r_a^+ FR$			$r_b^+ FR$			$r^-$			Res.
	pos.	width	rel.ampl.	pos.	width	rel.ampl.	pos.	width	rel.ampl.	$(\frac{B_{r^+}}{B_{r^-}})^2$
400mV	2871	17	16 ± 1	2932	18	17 ± 1	2965	23	10 ± 1	10.9 ± 2.4
150mV	2878	16	10 ± 2	2938	15	7 ± 2	2972	26	6 ± 2	8.0 ± 6.0
50mV	2884	31	5 ± 2	--	--	2 ± 2	2972	17	9 ± 2	0.60 ± 0.56
-110mV	2863	23	4 ± 2	2932	13	6 ± 2	2969	17	11 ± 2	0.83 ± 0.56
400mV	2874	12	13 ± 2	2937	17	10 ± 2	2971	22	12 ± 2	3.7 ± 1.9

Table 5.3: C<sub>6</sub> – Copper deposition. Quantitative analysis of the spectra in Fig.5.20 a)

the same intensity as for  $\vartheta = (21 \pm 1.5)^\circ$  and this is for  $\vartheta = (83 \pm 1.5)^\circ$  (figure 5.11 a). This range is compatible with an intensity ratio of 0.83. In this manner we have determined the angle range as  $\vartheta = (83 \pm 1.5)^\circ$  relying on the error of the  $r^-$  resonance. Arguing with the intensity of the  $r^+$  resonance gives the same result. Here a constant number of contributing molecules has implicitly been assumed. But even a diminution of 50% of the molecules in the dense phase would lead to a value of  $77^\circ$ .

After deposition we stripped the copper by rising the potential to +400 mV. The spectrum is taken after a waiting period of 15 minutes. It can be seen from figure 5.20 that the  $r^+$  resonances reappear and the spectrum resembles a type I spectrum however with a lower intensity which corresponds to a diminution of about 30% of the dense phase. The intensity ratio gives  $\vartheta = (30 \pm 7)^\circ$ .

In contrast to C<sub>6</sub>, no influence of the copper deposition is observed for C<sub>18</sub>. The spectrum remains the same over the entire potential range as can be seen from figure 5.21a. The behavior of the dodecanethiolate SAM is an intermediate one. The symmetric methyl stretching resonances always remain visible. The  $r^-$  resonance however seems to gain somewhat in intensity but no drastic change is observed (see figure 5.21b).

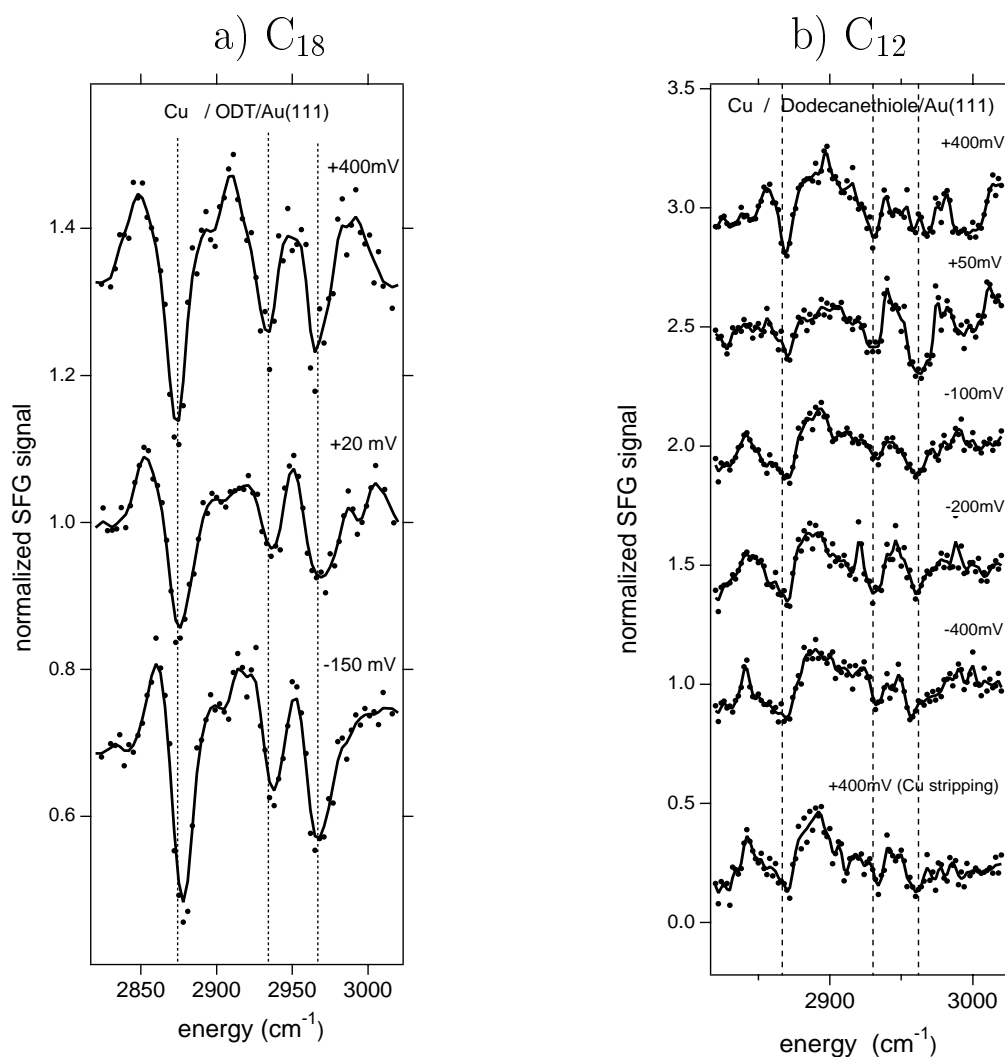


Figure 5.21: Normalized spectra of C<sub>18</sub> (a) and C<sub>12</sub> (b) during Cu deposition

### 5.5.5 Discussion

If copper would adsorb on top of a SAM, the peak intensities in the SFG spectra would be drastically changed. By the fact that the C<sub>18</sub> spectrum remains the same during Cu deposition, we can directly prove *in-situ* that the SAM acts in this case as a surfactant. The same is in principle valid for the C<sub>6</sub> SAM

Potential	$r_a^+ FR$			$r_b^+ FR$			$r^-$			Res.
	pos.	width	rel.ampl.	pos.	width	rel.ampl.	pos.	width	rel.ampl.	$\left(\frac{B_{r^+}}{B_{r^-}}\right)^2$
350mV	2875	11	10 ± 1	2931	12	7 ± 1	2968	23	5 ± 1	11.6 ± 5.0
180mV	2878	12	18 ± 2	2935	24	8 ± 2	2969	26	6 ± 2	18.8 ± 13.2
120mV	2878	10	15 ± 3	2935	15	7 ± 3	2968	17	9 ± 3	6.0 ± 4.6
60mV	2878	12	14 ± 2	2938	13	11 ± 2	2983	17	6 ± 2	17.4 ± 12.2
0mV	2875	12	9 ± 1	2935	16	6 ± 1	2970	22	3 ± 1	25.0 ± 17.3
-160mV	2874	15	9 ± 1	2932	18	6 ± 1	2968	22	5 ± 1	9.0 ± 4.0

Table 5.4: C<sub>6</sub> – Potential dependence of the SAM in a Cu-free electrolyte. Quantitative analysis of the spectra in Fig.5.20 b)

Potential	$r_a^+ FR$			$r_b^+ FR$			$r^-$			Res.
	pos.	width	rel.ampl.	pos.	width	rel.ampl.	pos.	width	rel.ampl.	$\left(\frac{B_{r^+}}{B_{r^-}}\right)^2$
400mV	2874	14	32 ± 3	2933	13	22 ± 3	2968	16	24 ± 1	5.1 ± 1.5
20mV	2875	17	21 ± 2	2937	15	10 ± 2	2969	23	14 ± 2	4.9 ± 1.7
-150mV	2878	14	31 ± 2	2938	13	15 ± 2	2967	19	21 ± 2	4.8 ± 1.1

Table 5.5: C<sub>18</sub> – Copper deposition. Quantitative analysis of the spectra in Fig.5.21 a)

which keeps at least the intensity of the asymmetric methyl resonance, even when several monolayers of Cu are deposited. The fact that we can strip off the copper and still obtain a spectrum with comparable intensity, shows that a large part ( $\sim 70\%$ ) of the thiolate remains at the surface and that the SAM acts not only during deposition but also during stripping as a surfactant.

The results of *ex-situ* XPS measurements have suggested that the Cu is deposited in between the SAM and the gold substrate, whereas *in-situ* STM measurements could not give any indication [80]. These two techniques focus on the properties of the deposited layer. In contrast, with the SFG experiments we could follow the surfactant action *in-situ* from the adsorbates point of view.

It might be thought that the change of type I to type II spectrum for  $C_6$  is imputable to the fact that the SAM is now adsorbed onto copper. There are several reasons which contradict this hypothesis. The most important is that the spectral change is clearly visible already in the UPD region (see figure 5.20a). However it is known from the STM experiments that, after the completion of the Cu island formation in the UPD range, the surface coverage only is 10% to 15% (see section 5.5.1), which is indeed not enough to account for the quasi disappearance of the symmetric methyl resonances. Further the tilt angle  $\alpha$  for alkanethiolate SAMs on Cu is about  $12^\circ$  [79, 107, 108] which results in a maximal possible angle  $\vartheta$  of  $47^\circ$ , incompatible with  $\vartheta \sim 80^\circ$  which is determined from the spectra. And finally it is not plausible why  $C_{18}$  spectra on copper should be very different from  $C_6$  spectra.

Copper deposition appears to proceed in STM studies qualitatively in a similar way for all SAMs in the range from  $C_6$  to  $C_{18}$ . For the same range of systems it *differs* drastically in SFG spectroscopy. Before copper islands form, a so-called "front" is detected with STM for all chain lengths (see figure 5.15) [139, 141]. We observed that only the affected area can express copper islands. In such an area the tunneling resistance is lowered, and ordered structures cannot be resolved. The SFG spectra should exhibit shifts in energy, intensity changes or the appearance of new bands if defects are present and influence the C – H vibrations. As discussed above, this is not the case for  $C_{18}$ , so we must conclude that the defects behind the front *do not affect the conformation of the backbone and the orientation of the methyl group*. This fact, combined with the idea that STM probes mainly the sulfur head group and is not sensitive to conformational changes of thiolates, leads us to propose for  $C_{18}$  a disorder of the sulfur packing while the chains largely retain their conformation (see theoretical studies [88, 156]). The penetration of aluminum into a  $C_{16}$  SAM appears to be based on similar processes [157].

Now we focus on the conformational possibilities which are compatible with a change of the methyl tilt angle  $\vartheta$  from  $20^\circ - 25^\circ$  to about  $75^\circ - 85^\circ$ . For the initial position we will assume a value of the Au-S-C angle which is not too far from the tetrahedral angle ( $109.5^\circ$ ) of the mostly accepted  $sp^3$  hybridization. The most straightforward way to reach the desired angular range for  $\vartheta$  is to perform a rotation about the S – C bond until  $\vartheta$  becomes sufficiently large. In this case  $\alpha$  becomes about  $70^\circ$ . Assuming a constant density of the monolayer, we can estimate from the cant angles  $\alpha$  ( $\alpha_{initial} \sim 35^\circ$ ) the new height of the

monolayer to be about 40% of the original height. This means that only 40% of the molecules remain on the surface and the rest has to desorb. However, the Cu stripping experiments show that a fraction of about 70% remains on the surface and thus excludes the simple chain tilt as possibility. If we abandon the working hypothesis in which we excluded an influence of the non detectable striped phase, we could speculate that the whole striped phase takes the same conformation as the tilted (initially dense) phase. This is compatible with the measured intensities since the molecular density of the striped phase corresponds to about 30% of the molecular density of the  $(\sqrt{3} \times \sqrt{3})R30^\circ$  phase (see chapter 5.1). The reorientation of all molecules into a  $(\sqrt{3} \times \sqrt{3})R30^\circ$  phase after the Cu stripping would lead to the postulated 70% of molecules in this phase (see figure 5.22a).

Another simple way to achieve the large change of  $\vartheta$  would be to introduce a terminal gauche defect. However we exclude this, since, as already said, this kind of gauche defects should be visible in the spectra as methylene resonances. However gauche defects which conserve the local inversion symmetry of the methylene groups, like the  $g^+tg^-$  sequences introduced in chapter 5.2.3, are not detectable with SFG. It is conceivable that for example a interdigitation mode (see Fig.5.3) - for which the exact structure is not known - is formed with such a  $g^+tg^-$  sequence. The space requirements of the molecules in the interdigitation mode should be lower than for the phase where the chain is simply tilted. Thus the desorption of molecules during the Cu deposition should be less important than in the previous case. For the reorientation after the Cu stripping experiments, a part of the striped phase could again help to reach the required intensity of 70% of the initial situation.

A completely different possibility to achieve a large change in  $\vartheta$  is to switch from  $sp^3$ - to  $sp$ -hybridization for the sulfur atom (see figure 5.22b). The Au-S-C angle becomes  $180^\circ$  and it follows immediately that  $\vartheta$  is about  $70^\circ$ . For  $\alpha$  one obtains  $35^\circ$ . Twisting about any C-C bond does not change  $\vartheta$  (and would in addition lead to gauche defects) and the only possibility to incline  $\vartheta$  further is to reduce the Au-S-C bond angle. The major difference of this mechanism with respect to the previous two is that a molecule does not need more space since the molecular cant angle  $\alpha$  remains about the same. An  $\alpha$  of  $45^\circ$  leads to a  $\vartheta$  of  $80^\circ$ , which corresponds to a desorption of about 15% of the dense phase. The spectral change can be explained solely with the dense phase and one does not have to recourse to the striped phase. The desorption of another 15% of the dense phase during the Cu stripping is plausible.

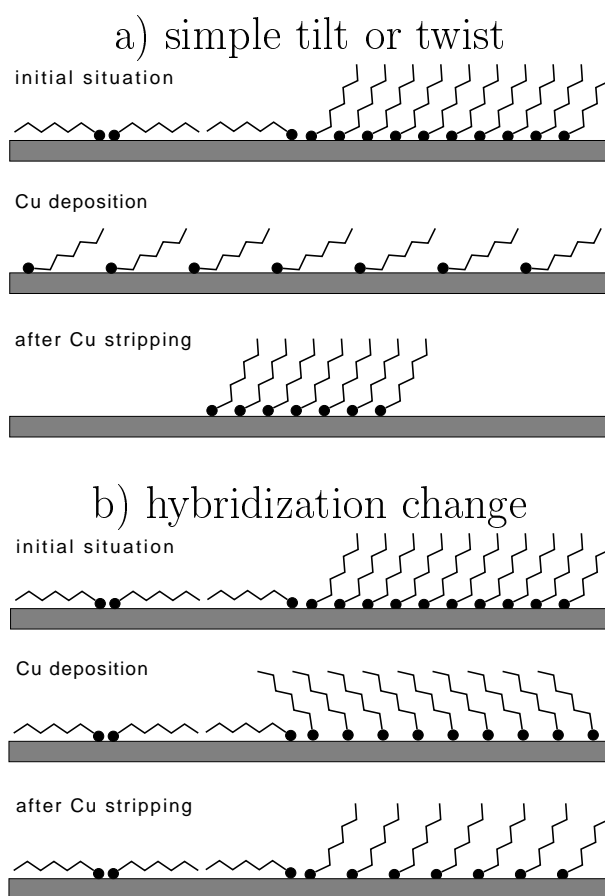


Figure 5.22: a) simple tilt or twist b) hybridization change

### 5.5.6 Conclusion

In this chapter we have studied *in-situ* the complex behavior of alkanethiol SAMs on gold during electrochemical Cu deposition. We were able to show that the C<sub>6</sub> SAM exhibits a drastic change in the SFG spectra, whereas no change is observed for C<sub>18</sub>. C<sub>12</sub> shows intermediate behavior.

With STM a disordering of the SAMs for all chain lengths is observed prior to the formation of Cu islands. In the case of C<sub>18</sub> it has been shown explicitly that the disappearance of *translational* order of the sulfur adsorbed on the substrate does not destroy the *orientational* order which is observed by SFG.

The surfactant behavior of the SAMs for all studied chain lengths could be directly followed with SFG.

*The change of the spectra for the C<sub>6</sub> SAM is neither imputable to the change of the substrate metal and its structure nor to the pure change of the potential. This is why we suggest here that it is triggered by copper ions or atoms penetrating the thiol layer.* The reason why this phase transition of the SAM appears for short chain thiolate SAMs and not for long chain thiolate SAMs might be that the alkyl chains of the latter are bound together stronger due to their larger number of methylene groups which will result in a reduced concentration of copper species in the thiolate layer during adsorption.

The change of the spectra of the C<sub>6</sub> SAM during copper deposition is due to a tilt of the methyl group angle  $\vartheta$  from  $\sim 21^\circ$  to  $\sim 80^\circ$ . Three conformations which are consistent with the new phase are proposed. The most probable conformation is the one where the hybridization of the adsorbed sulfur atom changes from  $sp^3$  to  $sp$ , since neither important desorption of the thiolate are required, nor an unlikely conformation with many centrosymmetric sequences of gauche defect. The other two conformations however can not be excluded. The fundamental problem is the lack of more detailed data of the system: When assuming the all-trans conformation of the molecule - which is justified since no methylene vibrations are visible in the spectra - it is crucial to know the angle of the S - C bond with respect to the surface. For this, the hybridization state of the sulfur atom must be known. Equally important is the question of the Au - S angle. But here too, there is incertitude about the sulfur adsorption sites and the question of the exact morphology of the bond is usually not addressed. Another complicating factor is the behavior of the striped phase which covers initially 50% of the surface and contains 25% of the adsorbed molecules. Even when it is exactly known how much of the molecules desorb during the copper-deposition or stripping process, the possible transfer of molecules between the striped and the dense phase makes it extremely difficult to argue quantitatively. In order to gain further insight into this kind of systems with spectroscopic methods, it would be of advantage to probe only a single phase, which could be realized by combining sophisticated sample preparation and highly resolving microscopy with spectroscopy.



## 5.6 Spectroscopic study of aminothiolate SAMs – solvent effects

### 5.6.1 Introduction

In the previous section we investigated the deposition of copper on alkanethiolate modified gold electrodes. The copper has been shown to be deposited in between the thiolate SAM and the gold surface. In this chapter we study a system which is interesting, because a metal can be deposited *on top* of a SAM. There, nanometer sized clusters form which are only weakly interacting with the underlying gold substrate.

In order to ensure the deposition of the metal on top of the SAM a special end-group of the thiolate has to be chosen. Thus Kind et al. [77] used the aminothiols  $\text{H-S-(CH}_2\text{)}_{10}\text{-CO-NH-(CH}_2\text{)}_2\text{-NH}_2$  in order to functionalize Au(111) electrodes. They bound palladium (Pd) in form of  $\text{Pd}^{2+}$  ions to the monolayer. The  $\text{Pd}^{2+}$  ions can bind to the free electron pair of the nitrogen atoms. By reducing the  $\text{Pd}^{2+}$  ions to Pd atoms they obtained Pd islands with a diameter of 1.5 – 6 nm which are situated on top of the monolayer as proven by XPS.

However, the choice of Kind et al. to replace the *apolar* methyl terminal group of *n*-alkanethiolates with the *polar*  $\text{-CO-NH-(CH}_2\text{)}_2\text{-NH}_2$  group has important consequences for the structure of the monolayer, since the interaction between the chains in the monolayer is much higher now. Whereas in the case of *n*-alkanethiolates the van-der-Waals interaction is predominant, for the aminothiolate a strong binding via hydrogen bonds – similar to the behavior of proteins where hydrogen bonds between different amide moieties ( $\text{-CO-NH-}$ ) cause the secondary structure – is likely to occur. This should noticeably affect the all-trans conformation of the  $\text{-CH}_2$  backbone which is known to occur for *n*-alkanethiolates (see chapter 5.2 and 5.5).

Even more important is that the *polar* terminal group of the aminothiolate SAM is hydrophil. Since the metal deposition takes place in an aqueous electrolyte with a pH of 1, there will be a strong interaction between the electrolyte and the AT SAM, again in contrast to the *n*-alkanethiolate systems.

A further effect can theoretically influence the conformation of the AT SAM. It is the form of the bond between the  $\text{Pd}^{2+}$  ions and the nitrogen

atoms which is still unknown yet. But one possibility is that a  $\text{Pd}^{2+}$  ion binds to *two* nitrogen atoms of the *same* chain the energetically favorable *trans*-conformation is given up and a *cis*-conformation is formed (see Fig.5.23) inducing strain in this part of the molecule.

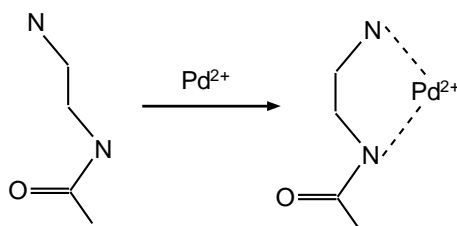


Figure 5.23: Possible change from *trans*- to *cis*-conformation induced through the presence of  $\text{Pd}^{2+}$  ions. The hydrogen atoms are omitted for the sake of simplicity.

## 5.6.2 Experimental

The aminothiols were synthesized by the group of H. Vogel (EPF Lausanne, Departement Chimie) and solutions of  $20 \mu\text{M}$  in absolute ethanol were prepared. The self-assembly is performed like described in chapter 5.2.2 for  $\text{C}_{12}$ . The substrates were gold evaporated on mica and glass for the SFG and IRRAS measurements, respectively (see chapter 5.2.2).

After the self-assembly the samples are immersed, thoroughly rinsed in absolute ethanol, and dried in air. The palladium deposition is done by covering the sample with a drop of  $\text{Pd}^{2+}$  catalyst solution. For the *in-situ* experiments the sample remains immersed and for the *ex-situ* measurements the sample is rinsed three times with a  $\text{HCl}/\text{NaCl}$  solution and dried in air. The  $\text{Pd}^{2+}$  catalyst solution was prepared with 10 mg of  $\text{Na}_2\text{PdCl}_4$  (Aldrich Chemical Co.) and 1.75 g of  $\text{NaCl}$  (Fluka) in 50 ml of  $\text{H}_2\text{O}$  (MilliQ) adjusting the solution with 37%  $\text{HCl}$  to  $\text{pH} = 1$ . The  $\text{HCl}/\text{NaCl}$  rinsing solution is 0.1 M  $\text{HCl}$  and 0.6 M  $\text{NaCl}$  in  $\text{H}_2\text{O}$  ( $\text{pH}=1$ ).

The SFG measurements are performed in co-propagating geometry like in the previous chapters (the  $\text{CaF}_2$  prism is used for the *in-situ* measurements) and the spectra are normalized as described there. For the presented IRRAS

measurements a grazing incidence accessory ( $80^\circ$ ) has been used with the FTIR spectrometer described in chapter 5.2.2.

### 5.6.3 Spectral characterization of the AT SAM in air

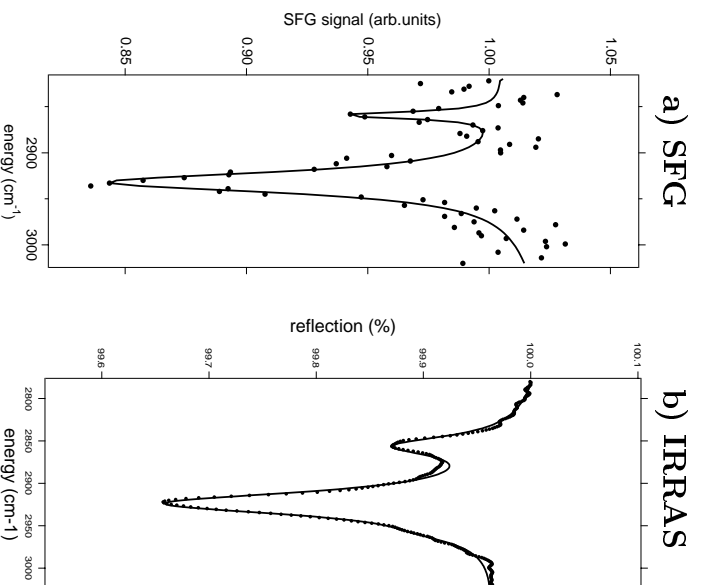


Figure 5.24: SFG and IRRAS spectra of an AT SAM in air. The peaks correspond to the symmetric  $d^+$  and asymmetric  $d^-$  methylene stretching modes. The points represent the data and the solid lines are fits with Lorentzian line shapes (see table 5.6).

Figure 5.24 presents SFG and IRRAS spectra of the C–H stretching vibration range of the AT SAM in air. In both spectra, the symmetric  $d^+$  and the asymmetric  $d^-$  methylene stretching vibration peaks at about  $2860\text{ cm}^{-1}$  and  $2930\text{ cm}^{-1}$ , respectively, are clearly observed. The SFG spectrum is thus completely different from the case of the alkane thiolate SAMs where virtually no contributions from methylene groups could be observed. This was explained by the

fact that in well ordered alkane thiolate SAMs the contributions of centrosymmetrically arranged methylene groups cancel pairwise. Thus we can directly conclude from the intensity of the resonances with respect to the non-resonant intensity of the substrate that there is a large amount of disordered methylene groups compared to the case of alkanethiolates.

In table 5.6 the quantitative analysis of both spectra is presented. The peak positions for IRRAS are  $2856\text{ cm}^{-1}$  and  $2924\text{ cm}^{-1}$  for the  $d^+$  and  $d^-$  vibrations, respectively. For well ordered alkanethiol SAMs  $2851\text{ cm}^{-1}$  and  $2918\text{ cm}^{-1}$  are reported [110]. The blue shift of these frequencies of several wavenumbers is caused from disorder in the chain [79, 137, 158]. Furthermore the peak width of  $28$  and  $34\text{ cm}^{-1}$  for  $d^+$  and  $d^-$ , respectively, is significantly larger than for well ordered alkanethiol SAMs where widths of about  $10$  and  $15\text{ cm}^{-1}$  are reported [92, 137], thus again indicating disorder in the film [137].

	$d^+$			$d^-$		
<i>method</i>	<i>pos.</i>	<i>width</i>	<i>rel.ampl.</i>	<i>pos.</i>	<i>width</i>	<i>rel.ampl.</i>
SFG	2859	9(?)	0.066	2932	27	0.171
IRRAS	2856	28	0.108	2924	34	0.320

Table 5.6: Quantitative analysis of the spectra in Fig.5.24. The positions and peak widths (FWHM) are given in  $\text{cm}^{-1}$ . The relative amplitude is in arbitrary units and cannot be compared between SFG and IRRAS measurements. The width of  $9\text{ cm}^{-1}$  for the  $d^+$  resonance in the SFG spectrum is smaller than the width of the probing IR beam and is due to the large scattering of the data points which does not allow an accurate fit in this region.

#### 5.6.4 Influence of the electrolyte – comparison between *ex-situ* and *in-situ*

After the spectral characterization in the C – H stretching vibration range the influence of the aqueous electrolyte is investigated (see Fig.5.25). The spectrum of the freshly prepared sample which is first measured in air has

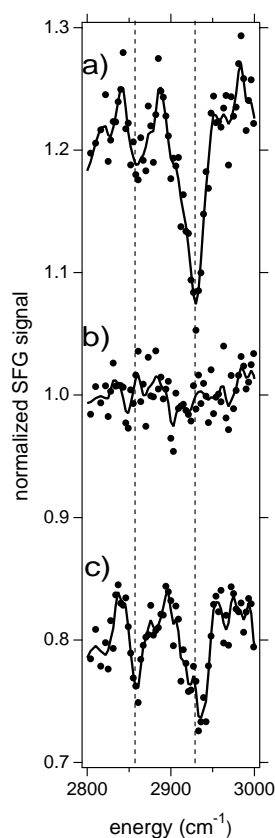


Figure 5.25: SFG spectra of an AT SAM. Freshly prepared and in air a), then immersed in Pd<sup>2+</sup> catalyst solution b), and then again in air but rinsed with HCl/NaCl solution. The spectra have been offset vertically for clarity.

the usual form. Then the sample is covered with the Pd<sup>2+</sup> catalyst solution and again measured using the CaF<sub>2</sub> prism as in the previous chapter. The peaks have disappeared, at least they lost more than one order of magnitude in strength. The Fresnel factors indeed change when passing from ex-situ to in-situ, which can alter the intensity but cannot explain the disappearance of the peaks in our geometry. In order to show that this change is not caused by destruction of the AT layer, the prism and the catalyst solution were removed, the sample was rinsed with the HCl/NaCl solution, and again measured in air. The peaks reappear (Fig.5.25c). If the AT SAM after the exposure to the Pd<sup>2+</sup>

method	$d^+$			$d^-$			new peak		
	pos.	width	rel.ampl.	pos.	width	rel.ampl.	pos.	width	rel.ampl.
SFG	2862	23	0.076	2930	47	0.157	2971	23(!)	0.017
IRRAS	2858	32	0.208	2926	37	0.529	2963	18	0.120

Table 5.7: Quantitative analysis of the spectra in figure 5.26. The (!) marks an approximate value which could not be submitted to optimization by the fitting procedure.

catalyst solution is rinsed, then covered with HCl/NaCl solution (which is in fact equivalent to the  $\text{Pd}^{2+}$  catalyst solution except for the palladium ions) and measured, the methylene peaks are also *not* observed. This excludes the possibility that large aggregates of Pd, so-called Pd nodules [77], degrade the sample surface and shows explicitly that the disappearance of the methylene resonances is caused by conformational changes of the AT SAM which are induced by the solutions.

The drying causes the AT SAM to return in a disordered conformation as exemplified by Fig.5.25c. It arises the question if the SAM is now in the same conformation as before being soaked in the solution. In order to have a closer look at this question we performed measurements in air after having covered and rinsed the SAM with the  $\text{Pd}^{2+}$  catalyst solution and the HCl/NaCl solution, respectively. The spectra of the dried samples are presented in figure 5.26 and the quantitative analysis is in table 5.7. The form of the spectra is very similar to those prior to deposition. However, a new peak at  $2963\text{ cm}^{-1}$  arises in the IRRAS spectrum. This peak is slightly visible in the SFG spectrum although close to the noise level.

A blue shift of the  $d^+$  and  $d^-$  stretching vibrations of several ten wavenumbers has been reported for methylene groups in *cis*-conformation [159], while normally very small shifts occur, even when the methylene groups are attached to very different functionalities. Hence, we suggest that this peak stems from methylene groups which are in *cis*-conformation. The driving force for the formation of the *cis*-conformations can originate from the drying process itself or from the fact that  $\text{Pd}^{2+}$  ions are bound to the AT SAM as described in figure 5.23. In order to settle the question of the origin of the new peak at  $2963\text{ cm}^{-1}$

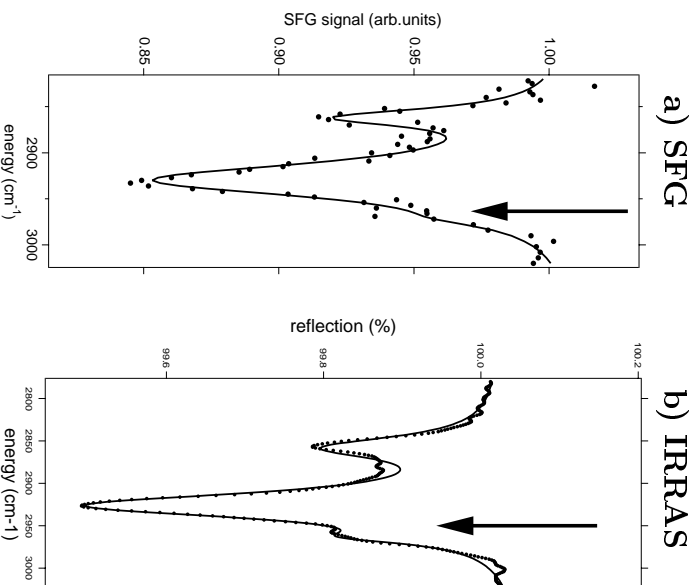


Figure 5.26: SFG a) and IRRAS b) ex-situ spectra of an AT SAM in air after exposition to the Pd<sup>2+</sup> catalyst solution and subsequent rinsing in HCl/NaCl solution. Arrows indicate the additional peak at 2971 and 2963 cm<sup>-1</sup>, respectively.

(IRRAS measurement) we freshly prepared AT samples and rinsed them *only* in the NaCl/HCl solution. Figure 5.27 shows IRRAS spectra of the sample before and after the rinsing procedure. Again the peak at 2963 cm<sup>-1</sup> is clearly visible and proofs thus that the influence of the solvent is the predominant factor for the formation of the *cis*-conformations and not the presence of the Pd<sup>2+</sup> ions. When the samples were immersed in pure water or in  $\sim$  1M NaCl solution the IRRAS spectra were qualitatively the same as in Fig.5.27b. Re-immersion in pure ethanol or in the AT self-assembly solution leads to IRRAS spectra which are equivalent to the spectra of freshly prepared films.

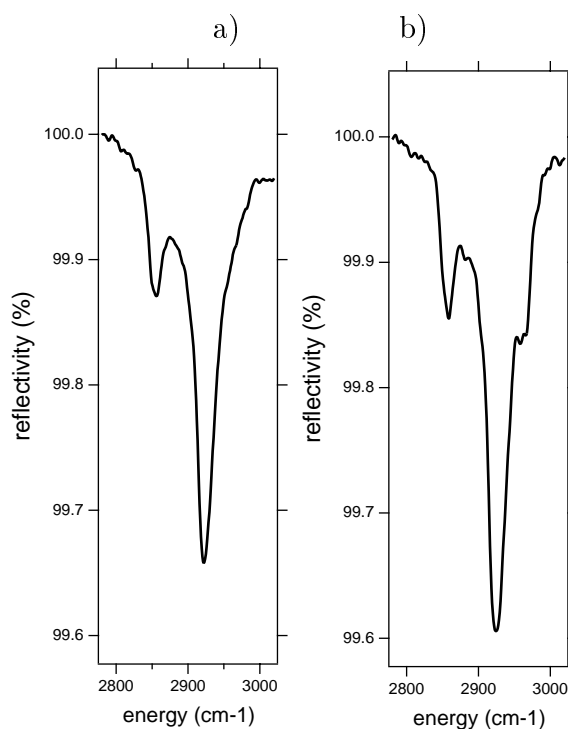


Figure 5.27: IRRAS spectra of AT SAMs; freshly prepared a) and after rinsing in HCl/NaCl solution b).

### 5.6.5 Discussion

The characterization of the pure AT monolayer clearly shows that the monolayer is disordered in air. This can be concluded from the appearance of methylene stretching vibrations in the SFG spectra and from the blue shift and broadening of the resonances in the IRRAS spectra. The disorder originates from the modified end group  $-\text{CO}-\text{NH}-(\text{CH}_2)_2-\text{NH}_2$ , since alkanethiolate SAMs with similar chain length such as  $\text{C}_{12}$ , are well ordered. The difference in chemical behavior to alkanethiolates is that the aminothiolate can form hydrogen bonds between the oxygen or nitrogen atoms and hydrogen atoms bound to nitrogen  $-\text{C}=\text{O}\cdots\text{H}-\text{N}-$  or  $-\text{HN}\cdots\text{H}-\text{N}-$ . The binding energy of hydrogen bonds is about 25 kJ/mol [160] and thus about one order of magnitude higher than the van-der-Waals binding energy per methylene unit [136]. In figure 5.28 a model of the AT SAM with hydrogen bonds is presented. It



is possible that intermolecular hydrogen bonds already form during the self-assembly process in ethanolic solution. This should result in a lower coverage due to steric constraints.

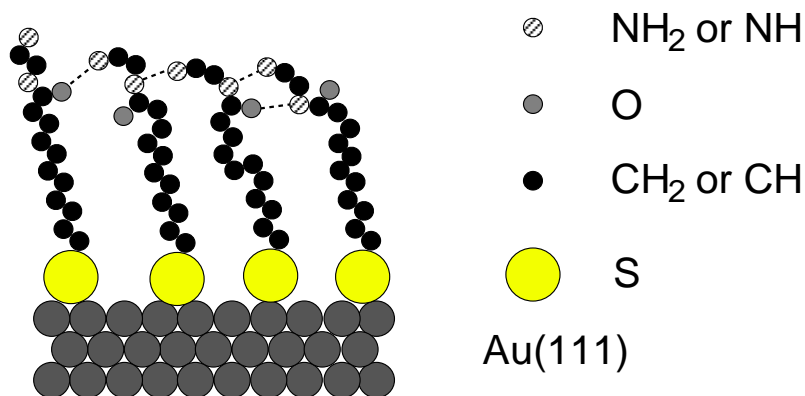


Figure 5.28: Possible model of the AT SAM in air. The dashed lines represent possible hydrogen bonds ( $\text{O} \cdots \text{H} - \text{N}$  or  $\text{N} \cdots \text{H} - \text{N}$ ). The chains are distorted and *not* all C or N atoms are placed in the same plane.

As shown, the disappearance of the methylene bands in SFG *in-situ* measurements is due to the conformation of the monolayer. Since SFG does not probe centro-symmetric structures we suppose the monolayer to be in such a conformation. Another possible arrangement could be a completely isotropic distribution of the methylene groups which is indeed incompatible with the fact that the AT molecules are still adsorbed at the surface. We thus conclude that the molecules exist mainly in the all-trans conformation. This implies that the number of hydrogen bonds is strongly reduced. We can be sure that the amino groups ( $\text{NH}_2$ ) in the monolayer are at least partially protonated ( $\text{NH}_3^+$ ) due to the acidic character of the electrolyte ( $\text{pH}=1$ ). This provokes mutual repulsion between the terminal groups which is minimized in the aqueous solution by screening the positive charges with a hydrate shell. In this way hydrogen bonds involving amino groups are broken. A substantial part of the carbonyl groups ( $\text{C} = \text{O}$ ) is probably also surrounded by water molecules due to their polarity. This “solvation” of the monolayer may result in the postulated all-trans conformation. The solvation process is reversible as shown by the alternate *ex-situ* and *in-situ* spectra (Fig.5.25).

The IRRAS spectra of AT SAMs which were rinsed in polar solvents exhibit

an additional peak at  $2963\text{ cm}^{-1}$ . This peak is typical for the asymmetric methyl stretching vibrations  $\nu_{\text{as}}$ . Since the AT molecule does not possess methyl groups one might suspect an often present hydrocarbon contamination layer which adsorbs from air onto the sample surface, or residuals from the ethanolic solutions. We can exclude this as *only* samples which were rinsed with the polar solutions did exhibit the additional peak. Samples which were only rinsed in ethanol never showed the peak at  $2963\text{ cm}^{-1}$ . Furthermore the peak disappears when a sample which was exposed to polar solvents is re-immersed in ethanol. As discussed, the peak can also not be imputed to a *cis*-conformation which is induced by the presence of  $\text{Pd}^{2+}$  ions. However, since no other candidates are available we assume that it originates by vibrations from strongly distorted methylene units. We may speculate on the reasons why the rinsing in strong polar solvents causes these distortions and not the rinsing in ethanol: The interactions of the terminal group with water are stronger than with ethanol; also the microscopic drying process itself and the drying rate may influence the conformation of the monolayer.

# Chapter 6

## Conclusion

In this work electronic properties of thin fullerene films have been studied with second harmonic (SH) spectroscopy as well as with time resolved second harmonic generation. A second subject was the investigation of metal deposition on gold electrodes which we modified with self-assembled monolayers (SAMs). Here we studied the deposition process *in-situ* by probing vibrational modes of the SAMs with sum frequency (SF) spectroscopy.

For thin films of the fullerenes  $C_{60}$  and  $C_{70}$  we performed second harmonic spectroscopy with a fundamental energy between 1.0 and 2.3 eV. For  $C_{60}$  four transitions are found and discussed. For  $C_{70}$  the signals are much weaker and many electric dipole allowed transitions are missing. For both fullerenes the lowest singlet excitons are observed while intensity due to the triplet excitons is not found. The pump beam induced suppression of the SH signal on  $C_{60}$  resonances is only efficient for the resonance at the lowest fundamental photon energy.

This suppression has been used to study the lifetime of the lowest singlet exciton as a function of distance (1-3 nm) to a metal substrate. Alkanethiols were employed in order to achieve uniform separation of  $C_{60}$  and the metal. Even at distances as small as 1 nm, classic damping mechanisms prevail, and no evidence for additional decay channels is detected. For Au substrates a predominance of energy transfer to the bulk is observed whereas for silver the transfer to the surface is dominant.

We also determined diffusion constants of  $C_{60}$  excitations for optical pump

energies above and below the band gap by grating experiments. Above 1.86 eV excitation energy a surprisingly high diffusion constant of about  $100 \text{ cm}^2/\text{s}$  is measured. It is proposed to result from singlet diffusion in the presence of vibrational and electronic excitation. Below 1.86 eV the energy diffusion constant drops abruptly by about one order of magnitude.

We rearranged totally the optical setup for the vibrational sum frequency (SF) spectroscopy of self-assembled monolayers. This was necessary because vibrational spectroscopy has higher demands concerning the bandwidth and the wavelength control of the probing radiation than spectroscopy of electronic states. Through this rearrangement a bandwidth of about  $12 \text{ cm}^{-1}$  together with a very reliable wavelength control has been obtained in the range of interest.

The spectroscopy of self-assembled monolayers on gold served to monitor *in situ* the electrochemical deposition of metals on the functionalized gold electrodes by probing the C – H stretching vibration range.

The deposition of copper on hexanethiolenol C<sub>6</sub> functionalized gold electrodes causes a strong increase of the tilt angle  $\vartheta$  of the terminal methyl ( $-\text{CH}_3$ ) end group. In order to analyze this change more quantitatively we developed a semi-empiric model and tested it for the relatively well known conformation of alkanethiolates on gold in air. Thus the tilt angle  $\vartheta$  of C<sub>6</sub> during copper deposition could be determined to be about  $80^\circ$ . We propose that the orientational change of the thiolate is triggered by the penetration of copper species in the thiolate layer and not by the change of the substrate. The copper deposition has no influence on the spectra of a C<sub>18</sub> thiolate layer. A C<sub>12</sub> layer shows an intermediate behavior. The thiolates show for all three chain lengths a surfactant behavior.

The endgroup modified aminothiolenol SAM shows strong methylene ( $-\text{CH}_2$ ) vibrational modes when probed in air. This is a sign of disorder in the chain and can be explained by hydrogen bonds between the polar units of the chain. *In-situ* measurements in aqueous solutions show that these resonances vanish. We propose that the disappearance of the resonances is due to solvation of the monolayer in the aqueous electrolyte which breaks up the hydrogen bonds and leads to a more ordered conformation of the SAM.

# Appendix A

## Fresnel factors

Refractive indices of gold and water			
Wavelength	450 nm	530 nm	3300 nm
gold	$1.53 + 1.86i$	$0.46 + 2.27i$	$1.25 + 17.6i$
water	1.34	1.34	1.42

Fresnel Factors for incidence in air			
	$L$	$K_{vis}$	$K_{IR}$
$x$	$-0.43 + 0.19i$	$0.45 - 0.34i$	$0.02 - 0.11i$
$z$	$0.92 + 0.39i$	$0.84 + 0.72i$	$1.61 + 0.16i$

Fresnel Factors for incidence in water			
	$L$	$K_{vis}$	$K_{IR}$
$x$	$-0.44 + 0.14i$	$0.45 - 0.20i$	$0.04 - 0.15i$
$z$	$0.73 + 0.36i$	$0.65 + 0.54i$	$1.61 + 0.23i$

Table A.1: Refractive indices [161] and the from these values calculated Fresnel factors for the experimental geometries.



# Bibliography

- [1] J. D. Jackson, *Klassische Elektrodynamik*, 2nd ed. (Walter de Gruyter, Berlin, 1983).
- [2] Y. Shen, *The Principles of Nonlinear Optics* (John Wiley & Sons, New York, 1984).
- [3] P. N. Butcher and D. Cotter, in *The elements of nonlinear optics*, edited by P. L. Knight and W. J. Firth (Cambridge University Press, Cambridge, 1990).
- [4] A. Le Rille, thesis, Université Paris XI Orsay, 1997.
- [5] C. Hirose, N. Akamatsu, and K. Domen, *Applied Spectroscopy* **46**, 1051 (1992).
- [6] E. Hecht, *Optics*, 2nd ed. (Addison-Wesley, Reading, Massachusetts, 1990).
- [7] V. Mizrahi and J. Sipe, *J. Opt. Soc. Am. B* **5**, 660 (1988).
- [8] Krause, thesis, Forschungszentrum Jülich, 1992.
- [9] H.-J. Krause and W. Daum, *Appl. Phys. B* **56**, 1 (1993).
- [10] M. Himmelhaus, thesis, Ruprecht-Karls-Universität Heidelberg, 1997.
- [11] Continuum, Operation and Maintenance Manual, PY61 Series Laser.
- [12] R. Becker, thesis, EPFL, 1996.
- [13] K. Wolfrum, thesis, Universität Bayreuth, 1993.

- [14] M. Dresselhaus, G. Dresselhaus, and P. Eklund, *Science of Fullerenes and Carbon Nanotubes* (Academic Press, San Diego, 1996).
- [15] S. Saito and A. Oshiyama, Phys. Rev. Lett. **66**, 2637 (1991).
- [16] S. Qin, W.-M. You, and Z.-B. Su, Phys.Rev.B **48**, 17562 (1993).
- [17] Z. Shuai and J. Brédas, Mol.Cryst.Liq.Cryst. **256**, 801 (1994).
- [18] D. Wilk, D. Johannsmann, C. Stanners, and Y. Shen, Phys.Rev.B **51**, 10057 (1995).
- [19] B. Koopmans, A.-M. Janner, H. Jonkman, G. Sawatzky, and F. van der Woude, Phys.Rev.Lett. **71**, 3569 (1993).
- [20] J. Heflin, D. Rodenberger, R. Shi, M. Wu, N. Wang, Y. Cai, and A. Garito, Phys.Rev.A **45**, R4233 (1992).
- [21] F. Li, J. Song, S. Qian, and Y. Li, Proc. SPIE **2284**, 169 (1994).
- [22] K. Kuhnke, R. Becker, H. Berger, and K. Kern, J.Appl.Phys. **79**, 3781 (1996).
- [23] P. Eklund, A. Rao, P. Zhou, Y. Wang, and J. Holden, Thin Solid Films **257**, 185 (1995).
- [24] E. Shirley, L. Benedict, and S. Louie, Phys.Rev.B **54**, 10970 (1996).
- [25] F. Negri, G. Orlandi, and F. Zerbetto, J.Chem.Phys. **97**, 6496 (1992).
- [26] D. van den Heuvel, G. van den Berg, E. Groenen, J. Schmidt, I. Hollenmann, and G. Meijer, J.Phys.Chem. **99**, 11644 (1995).
- [27] F. Negri, G. Orlandi, and F. Zerbetto, J.Phys.Chem. **100**, 10849 (1996).
- [28] B. Koopmans, A. Anema, H. Jonkman, G. Sawatzky, and F. van der Woude, Phys.Rev.B **48**, 2759 (1993).
- [29] R. Zamboni, M. Muccini, R. Danieli, C. Taliani, H. Mohn, W. Müller, and H. ter Meer, Proc. SPIE **2284**, 120 (1994).



- [30] A. Lucas, G. Gensterblum, J. Pireaux, P. Thiry, R. Caudano, J. Vigneron, L. Ph., and W. Krätschmer, *Phys.Rev.B* **45**, 13694 (1992).
- [31] S. Kazaoui and N. Minami, *Synth. Metals* **86**, 2345 (1997).
- [32] X. Wei, D. Dick, S. Jeglinski, and Z. Vardeny, *Synth. Metals* **86**, 2317 (1997).
- [33] A. Sassara, G. Zerza, M. Chergui, F. Negri, and G. Orlandi, *J.Chem.Phys.* **107**, 8731 (1997).
- [34] C. Hartmann, M. Zigone, G. Martinez, E. Shirley, L. Benedict, S. Louie, M. Fuhrer, and A. Zettl, *Phys.Rev.B* **52**, R5550 (1995).
- [35] M. Muccini, *Synthetic Metals* **83**, 213 (1996).
- [36] S. Ren *et al.*, *Appl.Phys.Lett.* **59**, 2678 (1991).
- [37] A. Hebard, R. Haddon, R. Fleming, and A. Kortan, *Appl.Phys.Lett.* **59**, 2109 (1991).
- [38] R. Benner, D. Dick, X. Wei, S. Jeglinski, Z. Vardeny, D. Moses, V. Sradanov, and F. Wudl, *Mol.Cryst.Liq.Cryst.* **256**, 241 (1994).
- [39] A.-M. Janner, R. Eder, B. Koopmans, H. Jonkman, and G. Sawatzky, *Phys.Rev.B* **52**, 17158 (1995).
- [40] R. Eder, A.-M. Janner, and G. Sawatzky, *Phys.Rev.B* **53**, 12786 (1996).
- [41] A.-M. Janner, Ph.D., Groningen, 1998.
- [42] A. Villaeys, V. Pflumio, and S. Lin, *Phys.Rev.A* **49**, 4996 (1994).
- [43] A. Sassara, G. Zerza, and M. Chergui, *J.Phys.Chem.A* **102**, 3072 (1998).
- [44] J. Shumway and S. Satpathy, *Chem. Phys. Lett.* **211**, 595 (1993).
- [45] S.-L. Ren, K. Wang, P. Zhou, Y. Wang, A. Rao, M. Meier, J. Selegue, and P. Eklund, *Appl.Phys.Lett.* **61**, 124 (1992).
- [46] F. Kajzar, C. Taliani, R. Danieli, S. Rossini, and R. Zamboni, *Phys.Rev.Lett.* **73**, 1617 (1994).

- [47] A. Sommerfeld, *Ann.Phys.* **28**, 665 (1909).
- [48] R. Chance, A. Prock, and R. Silbey, *Adv.Chem.Phys.* **37**, 1 (1978), and references therein.
- [49] A. Adams, R. Rendell, W. West, H. Broida, and P. Hansma, *Phys.Rev.B* **21**, 5565 (1980).
- [50] R. Rossetti and L. Brus, *J.Chem.Phys.* **73**, 572 (1980).
- [51] A. Alivisatos, D. Waldeck, and C. Harris, *J.Chem.Phys.* **82**, 541 (1985).
- [52] Q. Shu, P. Hansma, P. Das, and H. Metiu, *J.Luminescence* **40/41**, 745 (1988).
- [53] F. Balzer and H.-G. Rubahn, *J.Electron Spectrosc.Relat.Phenom.* **64/65**, 321 (1993).
- [54] A. Ulman, *An Introduction to Ultrathin Organic Films* (Academic Press, Inc., Boston, 1991).
- [55] K. Kuhnke, R. Becker, and K. Kern, *Chem. Phys. Lett.* **257**, 569 (1996).
- [56] H. Byrne, W. Maser, W. Rhle, A. Mittelbach, W. Hnle, H. von Schnering, B. Movaghar, and S. Roth, *Chem. Phys. Lett.* **204**, 461 (1993).
- [57] H. Byrne, in *Physics and Chemistry of Fullerenes and Derivatives*, edited by H. Kuzmany, J. Fink, M. Mehring, and S. Roth (World Science Publishing, New York, 1995), p. 183.
- [58] O. Cavalleri, A. Hirstein, J.-P. Bucher, and K. Kern, *Thin Solid Films* **284/285**, 392 (1996).
- [59] R. Becker, O. Cavalleri, and Kern.K., unpublished .
- [60] H. Kuhn, *J.Chem.Phys* **53**, 101 (1970).
- [61] B. Persson and N. Lang, *Phys.Rev.B* **26**, 5409 (1982).
- [62] N. Ashcroft and N. Mermin, *Solid State Physics* (CBS Publishing Ltd., Saunders College, Philadelphia, 1987).

- [63] P. Lane, L. Swanson, Q.-X. Ni, J. Shinar, J. Engel, T. Barton, and L. Jones, *Phys.Rev.Lett.* **68**, 887 (1992).
- [64] T. Ebbesen, Y. Mochizuki, K. Tanigaki, and H. Hiura, *Europhys. Lett.* **25**, 503 (1994).
- [65] A. Skumanich, *Chem. Phys. Lett.* **182**, 486 (1991).
- [66] M. Muccini, H. Schlaich, J. Feldmann, H. Bässler, E. Göbel, R. Zamboni, C. Taliani, J. Erxmeyer, and A. Weidinger, *Synth.Metals* **77**, 177 (1996).
- [67] T. Rose, R. Righini, and M. Fayer, *Chem. Phys. Lett.* **106**, 13 (1984).
- [68] H. Schwab, K.-H. Pantke, J. Hvam, and C. Klingshirn, *Phys.Rev.B* **46**, 7528 (1992).
- [69] A. Kortan, N. Kopylov, S. Glarum, E. Gyorgy, A. Ramirez, R. Fleming, F. Thiel, and R. Haddon, *Nature* **355**, 529 (1992).
- [70] R. Lof, M. van Veenendahl, B. Koopmans, H. Jonkman, and G. Sawatzky, *Phys.Rev.Lett.* **68**, 3924 (1992).
- [71] X. Zhu, T. Rasing, and Y. Shen, *Phys.Rev.Lett.* **61**, 2883 (1988).
- [72] L. Smith, J. Preston, J. Wolfe, D. Wake, J. Klem, T. Henderson, and H. Morko, *Phys.Rev.B* **39**, 1862 (1989).
- [73] M. Kaiser, W. Maser, H. Byrne, A. Mittelbach, and S. Roth, *Solid State Commun.* **87**, 281 (1993).
- [74] S. Kazaoui, R. Ross, and N. Minami, in *Physics and Chemistry of Fullerenes and Derivatives*, edited by H. Kuzmany, J. Fink, M. Mehring, and S. Roth (World Science, New York, 1995), pp. 242–245.
- [75] C. Lee, G. Yu, B. Kraabel, D. Moses, and V. Srdanow, *Phys.Rev.B* **49**, 10572 (1994).
- [76] T. Wink, S. van Zuilen, A. Bult, and W. van Bennekom, *Analyst* **122**, 34R (1997).
- [77] H. Kind, A. M. Bittner, O. Cavalleri, K. Kern, and T. Greber, *J. Phys. Chem. B* **102**, 7582 (1998).

- [78] J. Scherer, M. Vogt, O. Magnussen, and R. Behm, *Langmuir* **13**, 7045 (1997).
- [79] G. K. Jennings, J. C. Munro, T.-H. Yong, and P. E. Laibinis, *Langmuir* **14**, 6130 (1998).
- [80] O. Cavalleri, A. Bittner, H. Kind, K. Kern, and T. Greber, *Zeitschrift für Physikalische Chemie* **208**, 107 (1999).
- [81] P. Harder, M. Grunze, R. Dahint, G. M. Whitesides, and P. E. Laibinis, *J. Phys. Chem. B* **102**, 426 (1998).
- [82] D. J. Lavrich, S. M. Wetterer, S. L. Bernasek, and G. Scoles, *J. Phys. Chem. B* **102**, 3456 (1998).
- [83] H. Sellers, A. Ulman, Y. Shnidman, and J. E. Eilers, *J. Am. Chem. Soc.* **115**, 9389 (1993).
- [84] T.-W. Li, I. Chao, and Y.-T. Tao, *J. Phys. Chem. B* **102**, 2935 (1998).
- [85] M. Yeganeh, S. Dougal, R. Polizzotti, and P. Rabinowitz, *Phys. Rev. Lett.* **74**, 1811 (1995).
- [86] P. Fenter, F. Schreiber, L. Berman, G. Scoles, P. Eisenberger, and M. Bedzyk, *Surface Science* **412/413**, 213 (1998).
- [87] G. J. Kluth, C. Carraro, and R. Maboudian, *Phys. Rev. B* **59**, R10 449 (1999).
- [88] R. Bhatia and B. J. Garrison, *Langmuir* **13**, 4038 (1997).
- [89] A. Harris, C. Chidsey, N. J. Levinos, and D. Loiacono, *Chem. Phys. Lett.* **141**, 350 (1987).
- [90] P. Fenter, A. Eberhardt, K. Liang, and P. Eisenberger, *J. Chem. Phys.* **106**, 1600 (1997).
- [91] R. H-Terrill, T. A. Tanzer, and P. W. Bohn, *Langmuir* **14**, 845 (1998).
- [92] J. Thome, M. Himmelhaus, M. Zharnikov, and M. Grunze, *Langmuir* **14**, 7435 (1998).

- [93] P. E. Laibinis, G. M. Whitesides, D. L. Allara, Y.-T. Tao, A. N. Parikh, and R. G. Nuzzo, *J. Am. Chem. Soc.* **113**, 7152 (1991).
- [94] L. H. Dubois and R. G. Nuzzo, *Annu. Rev. Phys. Chem.* **43**, 437 (1992).
- [95] B. Ewen, G. R. Strobl, and D. Richter, *Faraday Disc. Chem. Soc.* **69**, 19 (1980).
- [96] R. G. Snyder, *J. Chem. Phys.* **71**, 3229 (1979).
- [97] W. Mar and M. L. Klein, *Langmuir* **10**, 188 (1994).
- [98] G. Poirier, *Langmuir* **15**, 1167 (1999).
- [99] G. Poirier and M. Tarlov, *J. Phys. Chem.* **99**, 10966 (1995).
- [100] N. Camillone, P. Eisenberger, T. Leung, P. Schwartz, G. Scoles, G. Poirier, and M. Tarlov, *J. Chem. Phys.* **101**, 11031 (1994).
- [101] G. Poirier, M. Tarlov, and H. Rushmeier, *Langmuir* **10**, 3383 (1994).
- [102] R. Gerlach, G. Polanski, and H.-G. Rubahn, *Appl. Phys. A* **65**, 375 (1997).
- [103] L. H. Dubois, B. R. Zegarski, and R. G. Nuzzo, *J. Chem. Phys.* **98** (1), 678 (1993).
- [104] G. K. Jennings and P. E. Laibinis, *Langmuir* **12**, 6173 (1996).
- [105] G. E. Poirier, *Chem. Rev.* **97**, 1117 (1997).
- [106] A. Harris, L. Rothberg, L. Dubois, N. Levinos, and L. Dhar, *Phys. Rev. Lett.* **64**, 2086 (1990).
- [107] C. Zubragel, F. Schneider, M. Neumann, G. Hahner, C. Woll, and M. Grunze, *Chemical Physics Letters* **219**, 127 (1994).
- [108] A. Imanishi, K. Isawa, F. Matsui, T. Tsuduki, T. Yokoyama, H. Kondoh, Y. Kitajima, and T. Ohta, *Surface science* **407**, 282 (1998).
- [109] M. A. Hines, J. Todd, and P. Guyot-Sionnest, *Langmuir* **11**, 493 (1995).

- [110] R. G. Nuzzo, E. M. Korenic, and L. H. Dubois, *J. Chem. Phys* **93**, 767 (1990).
- [111] M. D. Porter, T. B. Bright, D. L. Allara, and C. E. Chidsey, *J. Am. Chem. Soc.* **109**, 3559 (1987).
- [112] S. M. Stole and M. D. Porter, *Langmuir* **6**, 119 (1990).
- [113] P. E. Laibinis, R. G. Nuzzo, and G. M. Whitesides, *J. Phys. Chem.* **96**, 5097 (1992).
- [114] R. A. MacPhail, H. L. Strauss, R. G. Snyder, and C. A. Elliger, *J. Phys. Chem.* **88**, 334 (1984).
- [115] R. G. Snyder, S. Hsu, and S. Krimm, *Spectrochimica Acta* **34A**, 395 (1978).
- [116] M. A. Bryant and J. E. Pemberton, *J. Am. Chem. Soc.* **113**, 8284 (1991).
- [117] O. Cavalleri, thesis, EPFL, 1997.
- [118] A. B. Horn, D. A. Russell, L. J. Shorthouse, and T. R. Simpson, *J. Chem. Soc., Faraday Trans.* **92**, 4759 (1996).
- [119] M. Himmelhaus, M. Buck, and M. Grunze, *Appl. Phys. B* **68**, 595 (1999).
- [120] P. Guyot-Sionnest, J. Hunt, and Y. Shen, *Phys. Rev. Lett.* **59**, 1597 (1987).
- [121] S. R. Goates, D. A. Schofield, and C. D. Bain, *Langmuir* **15**, 1400 (1999).
- [122] A. Le Rille, A. Tadjeddine, W. Zheng, and A. Peremans, *Chem. Phys. Lett.* **271**, 95 (1997).
- [123] R. G. Nuzzo, L. H. Dubois, and D. L. Allara, *J. Am. Chem. Soc* **112**, 558 (1990).
- [124] M. A. Hines, T. D. Harris, A. L. Harris, and Y. J. Chabal, *J. Electron Spectrosc. Relat. Phenom.* **64/65**, 183 (1993).
- [125] K. Wolfrum, J. Löbau, and A. Lauberau, *Appl. Phys. A* **59**, 605 (1994).

- [126] P. Guyot-Sionnest, R. Superfine, J. Hunt, and Y. Shen, *Chem. Phys. Lett.* **144**, 1 (1988).
- [127] A. Lampert, thesis, Ruprecht-Karls-Universität Heidelberg, 1997.
- [128] R. Superfine, J. Huang, and Y. Shen, *Phys. Rev. Lett.* **66**, 1066 (1991).
- [129] V. Pouthier, C. Ramseyer, and C. Girardet, *J. Chem. Phys.* **108** (15), 6502 (1998).
- [130] M. Gussoni, in *Vibrational Intensities in Infrared and Raman Spectroscopy*, edited by W. B. Person and G. Zerbi (Elsevier, New York, 1982).
- [131] M. Gussoni, in *Advances in Infrared and Raman Spectroscopy*, edited by R. J. H. Clark and R. E. Hester (Heyden & Son, Philadelphia, 1980).
- [132] B. Schrader and W. Merier, *Raman/Infrared Atlas of Organic Compounds* (Verlag Chemie, Weinheim, 1974).
- [133] M. J. Colles and J. E. Griffith, *J. Chem. Phys.* **56**, 3384 (1972).
- [134] R. A. MacPhail, R. G. Snyder, and H. L. Strauss, *J. Chem. Phys.* **77**, 1118 (1982).
- [135] G. Hähner, M. Kinzler, C. Thümmel, C. Wöll, and M. Grunze, *J. Vac. Sci. Technol. A* **10**, 2758 (1992).
- [136] A. J. Pertsin and M. Grunze, *Langmuir* **10**, 3668 (1994).
- [137] F. Bensebaa and T. Ellis, *Langmuir* **14**, 2361 (1998).
- [138] M. Buck, F. Eisert, J. Fischer, and F. Träger, *J. Vac. Sci. Technol. A* **10**, 926 (1992).
- [139] O. Cavalleri, S. E. Gilbert, and K. Kern, *Chemical Physical Letters* **269**, 479 (1997).
- [140] O. Cavalleri, H. Kind, A. Bittner, and K. Kern, *Langmuir* **14**, 7292 (1998).

- [141] S. E. Gilbert, O. Cavalleri, and K. Kern, *J. Phys. Chem.* **100**, 12123 (1996).
- [142] J. A. M. Sondag-Huethorst and L. G. J. Fokking, *J. Electroanal. Chem.* **367**, 49 (1994).
- [143] M. H. Hölzle, U. Retter, and D. M. Kolb, *J. Electroanal. Chem.* **371**, 101 (1994).
- [144] S. Manne, P. K. Hansma, J. Massie, V. B. Elings, and A. A. Gewirth, *Science* **251**, 183 (1991).
- [145] T. Hachiya, H. Honbo, and K. Itaya, *J. Electroanal. Chem.* **315**, 275 (1991).
- [146] W. Haiß, J. Sass, and M. van Heel, in *Atomic Force Microscopy/Scanning Tunneling Microscopy*, edited by S.H. Cohen et al. (Plenum Press, New York, 1994), p. 423.
- [147] O. M. Magnussen, J. Hotlos, G. Beitel, D. M. Kolb, and R. J. Behm, *J. Vac. Sci. Technol.* **B 9**, 969 (1991).
- [148] M. F. Toney, J. N. Howard, J. Richter, G. L. Borges, J. G. Gordon, O. R. Melroy, D. Yee, and L. B. Sorensen, *Phys. Rev. Lett.* **75**, 4472 (1995).
- [149] O. R. Melroy, M. G. Samant, G. L. Borges, J. G. Gordon, L. Blum, J. H. White, M. J. Albarelli, M. McMillan, and H. D. Abruña, *Langmuir* **4**, 728 (1988).
- [150] J. A. M. Sondag-Huethorst and L. G. J. Fokking, *Langmuir* **11**, 4823 (1995).
- [151] O. Cavalleri, private communication.
- [152] H. Hagenström, M. Schneeweiss, and D. M. Kolb, *Langmuir* **15**, 2435 (1999).
- [153] A. M. Bittner, J. Wintterlin, and G. Ertl, *J. Electroanal. Chem.* **388**, 225 (1995).
- [154] X. Gao and M. J. Weaver, *Phys. Rev. Lett.* **73**, 846 (1994).



- [155] M. M-Walczak, C. Chung, S. M. Stole, C. A. Widrig, and M. D. Porter, *J. Am. Chem. Soc.* **113**, 2370 (1991).
- [156] R. Bhatia and B. J. Garrison, *Langmuir* **13**, 765 (1997).
- [157] A. Hooper, G. L. Fisher, K. Konstadinidis, D. Jung, H. Nguyen, R. Opila, R. W. Collins, N. Winograd, and D. L. Allara, *J. Am. Chem. Soc.* **121**, 8052 (1999).
- [158] G. K. Jennings and P. E. Laibinis, *J. Am. Chem. Soc.* **119**, 5208 (1997).
- [159] T. Iwamoto, *Inorganica Chimica Acta* **2**, 269 (1968).
- [160] F. A. Cotton and G. Wilkinson, *Basic Inorganic Chemistry* (Wiley & Sons, Inc., New York, 1976).
- [161] *American Institute of Physics Handbook*, 3rd ed., edited by D. E. Gray (Mc Graw Hill, New York, 1972).



# Curriculum Vitae

Nom:	Maximilian Epple
Date de naissance:	10 septembre 1968 à Munich
Nationalité	allemande
1978 - 1987	Gymnase à Augsburg (D)
1988 - 1989	Service civil
1989 - 1995	Etudes de physique à l'Université de Bayreuth (D)
1992-1993	Année d'échange avec l'Université Paris VII (F)
1994 - 1995	Travail de diplôme dans le group de Prof. Dr. J. Küppers à l'Université de Bayreuth: "Abbildungsmechanismen beim STM auf atomarer Skala"
depuis dec. 1995	Thèse dans le group de Prof. Dr. K. Kern à l'institut de physique expérimentale de l'EPFL: "Second Harmonic and Sum Frequency Spectroscopy of Thin Films and Molecular Monolayers"



# Remerciements

J'aimerais remercier tous ceux qui ont contribué, d'une manière ou d'une autre, à cette thèse:

Le professeur Klaus Kern, qui m'a donné la possibilité d'effectuer ce travail dans son groupe, et qui a guidé ce travail tout en me laissant la liberté nécessaire. Klaus Kuhnke pour son grand engagement et sa passion à discuter tous les problèmes en détail. Alexander Bittner, pour tout ce qu'il a apporté: son élan, ses connaissances en chimie et électrochimie et son enthousiasme pour le ski et bien d'autres choses.

Je tiens particulièrement à remercier Michael Himmelhaus qui m'a communiqué sans retenue toutes les astuces et tous les paramètres qui sont nécessaires pour maîtriser son système laser. C'est mon séjour dans son labo à Heidelberg qui m'a donné l'impulsion pour effectuer le changement crucial de l'OPG/A. Mes remerciements vont aussi à Abderrahmane Tadjeddine et son équipe Wang-Quan Zheng et Olivier Pluchery, qui m'ont chaleureusement accueilli au CLIO à Orsay. Je remercie Raymond Hourriet pour la bonne collaboration lors des mesures FT-IR.

J'aimerais aussi remercier toute l'équipe du secrétariat et de l'atelier pour leur collaboration précieuse et agréable. En particulier André Guisolan pour ses conseils dans tous les problèmes et Michel Fazan pour la préparation de toutes sortes de substrats ainsi qu'Andrea Testa et Martial Doy pour l'assistance informatique.

De plus, j'aimerais dire merci à tous mes collègues pour l'ambiance amicale et agréable en particulier mes collègues de bureau Martial Blanc, Bjørn Fischer, Emmanuelle Vargoz et Samuel Sarbach. Un merci aussi à Janick Schaufelbühl pour avoir relu de grandes parties de ce travail pour l'anglais. Et c'est le

moment de dire à touTEs les amiEs que j'ai rencontrÉs ici qu' ils/elles ont été un précieux soutien moral pour moi et que j'ai passé beaucoup de beaux moments avec eux/elles.

Ma famille mérite aussi un très grand merci pour m'avoir toujours soutenu à tous les niveaux et avoir toujours cru en moi.